ULTRASOUND MEDIATED NANOPARTICLE DRUG DELIVERY

Lee B. Mullin

A dissertation submitted to the faculty of the University of North Carolina at Chapel Hill in partial fulfillment of the requirements for the degree of Doctor of Philosophy in the Department of Biomedical Engineering.

Chapel Hill
2014

Approved by:

Paul A. Dayton

Caterina M. Gallippi

Michael Jay

Russell J. Mumper

Yueh Lee

ABSTRACT

Lee B. Mullin: Ultrasound Mediated Nanoparticle Drug Delivery.
(Under the direction of Paul A. Dayton)

Ultrasound is not only a powerful diagnostic tool, but also a promising therapeutic technology that can be used to improve localized drug delivery. Microbubble contrast agents are micron sized encapsulated gas filled bubbles that are administered intravenously. Originally developed to enhance ultrasound images, microbubbles are highly echogenic due to the gas core that provides a detectable impedance difference from the surrounding medium. The core also allows for controlled response of the microbubbles to ultrasound pulses. Microbubbles can be pushed using acoustic radiation force and ruptured using high pressures. Destruction of microbubbles can increase permeability at the cellular and vascular level, which can be advantageous for drug delivery.

Advances in drug delivery methods have been seen with the introduction of nanoparticles, nanometer sized objects often carrying a drug payload. In chemotherapy, nanoparticles can deliver drugs to tumors while limiting systemic exposure due to abnormalities in tumor vasculature such large gaps between endothelial cells that allow nanoparticles to enter into the interstitial space; this is referred to as the enhanced permeability and retention (EPR) effect. However, this effect may be overestimated in many tumors. Additionally, only a small percentage of the injected dose accumulates in the tumor, which most the nanoparticles accumulating in the liver and spleen.

It is hypothesized that combining the acoustic activity of an ultrasound contrast

agent with the high payload and extravasation ability of a nanoparticle, localized delivery to the tumor with reduced systemic toxicity can be achieved. This method can be accomplished by either loading nanoparticles onto the shell of the microbubble or through a coadministration method of both nanoparticles and microbubbles. The work presented in this dissertation utilizes novel and commercial nanoparticle formulations, combined with microbubbles and a variety of ultrasound systems. Ultrasound parameters are optimized to achieve maximum cell internalization of molecules and increased nanoparticle delivery to a cell layer on a coverslip. *In vivo* studies demonstrate the possibility of using a lower dose of paclitaxel to slow tumor growth rates, increase doxorubicin concentration in tumor tissue, and enhance tumor delivery of fluorescent molecules through treatments that combine nanoparticles with ultrasound and microbubbles.

To my parents, for their endless support and encouragement,
and to Jon Nunn, who has been an incredibly loving, supportive
and patient partner through this journey.

ACKNOWLEDGMENTS

There are so many people who have contributed either directly, or indirectly, to the completion of this work, and without whom I would not have survived graduate school. I want to thank my advisor, Paul Dayton, for his guidance and support; my lab mates, especially Jason Streeter, Ryan Gessner, Paul Sheeran, Steve Feingold and Chris Arena, who helped me through the entire process, assisted with experiments, and allowed me to vent; Jim Tsuruta and Kennita Johnson, were invaluable resources who were was always willing to troubleshoot experiments with me and assisted in material preparation. This work involved collaborations with multiple groups and individuals, specifically the Jay Lab: Jun Han, Marina Grace Leed, Xiuling Lu and Jin-Ki Kim; the Mumper Lab: Lei Peng, Ping Ma, Saurabh Wadhwa and Russ Mumper, and the Zamboni Lab: Gina Song and Bill Zamboni. Finally, I want to thank the UNC animal core, specifically Charlene Ross, Karla Johnson, Silmara Camargo, Mark Ross and Alain Valdivia, who assisted with animal experiments and the BRIC staff who assisted with optical imaging, specifically Hong Yuan and Jonathan Frank.

Funding for this research was provided by the Howard Hughes Medical Institute Med into Grad Program, the Carolina Center for Cancer Nanotechnology Excellence and NIH R01EB008733.

TABLE OF CONTENTS

Table of Contents . . . . . **vii**

List of Figures . . . . . **xii**

List of Tables . . . . . **xiv**

List of Abbreviations . . . . . **xv**

1 Introduction **1**

1.1 Ultrasound and Microbubble Contrast Agents 1

1.1.1 History of Contrast Agent Development 2

1.1.2 Response of Microbubble Contrast Agents to Ultrasound . . 3

1.2 Cancer and Nanoparticles 4

1.2.1 Chemotherapeutic Drugs 4

1.2.2 Tumor Microenvironment 5

1.2.3 Nanoparticles 7

1.3 Scope 10

2 US Drug Delivery **12**

2.1 Introduction 12

2.2 Ultrasound and Nanoparticles 12

2.2.1 Mechanisms of Delivery 13

2.2.2 Types of Administration 15
2.3 Ultrasound Setups 17
2.4 Review of Successful Nanoparticle Delivery Studies 18
2.5 Summary 21

3 US and MB Parameters for Sonoporation 22
3.1 Introduction 22
3.2 Materials and Methods 24
3.2.1 Cell Culture 24
3.2.2 Microbubble Preparation 24
3.2.3 Sonoporation Setup 25
3.2.4 Image Analysis 27
3.2.5 Statistical Analysis 27
3.3 Results and Discussion 28
3.4 Conclusions 36

4 Design of Acoustically Active NC Delivery Vehicles for US-Targeted Chemotherapy 37
4.1 Introduction 37
4.2 Materials and Methods 38
4.2.1 Materials 38
4.2.2 Biotinylated Microbubble Preparation 38
4.2.3 BTM Nanocapsule Preparation 38
4.2.4 AADV Preparation 40
4.2.5 Cell Culture 40
4.2.6 *In Vitro* Delivery 40
4.2.7 Vehicle Drug Loading 42
4.3 Results and Discussion 42

4.4 Conclusions 44

5 4T1 Tumor Treatment with Paclitaxel NC and MB Enhanced US Delivery 47

5.1 Introduction 47

5.2 Materials and Methods 48

5.2.1 Materials 48

5.2.2 Microbubble Preparation 48

5.2.3 Nanocapsule Preparation 48

5.2.4 Animal Preparation 49

5.2.5 Treatment 50

5.2.6 Analysis 51

5.3 Results and Discussion 51

5.4 Conclusions 54

6 *In Vivo* Targeted NP Delivery to Tumors with ARF 55

6.1 Introduction 55

6.2 Materials and Methods 56

6.2.1 Materials 56

6.2.2 Biotinylated Microbubble Preparation 56

6.2.3 Targeted Nanoparticle and Microbubble Preparation 57

6.2.4 Targeted Fluorescent Microbubble Preparation 57

6.2.5 Animal Preparation 57

6.2.6 Ultrasound Procedure 58

6.2.7 Optical Imaging 60

6.3 Results and Discussion 60

6.3.1 Nanoparticle Loaded Microbubbles 60

6.3.2 Radiation Force Targeting 60

6.4 Conclusions 68

7 PK Analysis of US Mediated PEGylated Liposomal Doxorubicin Delivery to Tumors 69

7.1 Introduction 69

7.2 Materials and Methods 70

7.2.1 Microbubble Preparation 70

7.2.2 PLD Preparation 71

7.2.3 Animal Preparation 71

7.2.4 Pharmacokinetic Study Design 73

7.2.5 Sample Processing and Analytical Methods 73

7.2.6 Pharmacokinetic Analysis 75

7.3 Results 75

7.3.1 Study 1 75

7.3.2 Study 2 81

7.4 Discussion 83

7.5 Conclusions 87

8 Concluding Remarks 88

8.1 Summary 88

8.1.1 MB Formulations 90

8.1.2 Ultrasound Sources 90

8.2 Future Directions 94

8.3 Clinical Translation 96

8.4 Conclusions 100

A Review of Nanoparticle Delivery Studies 101

B Effect of Anesthesia Carrier Gas on *In Vivo* Circulation

Times of Ultrasound MCAs in Rats 103

B.1 Introduction 103

B.2 Experimental 105

B.2.1 Gas Diffusion Model 105

B.2.2 Animal Preparation 107

B.2.3 Contrast Agent Preparation and Administration 107

B.2.4 Image Acquisition 108

B.2.5 Monitoring Physiological Changes 109

B.2.6 Measuring Microbubble Circulation Time 109

B.3 Results 110

B.3.1 Effects of Carrier Gas Composition on MCA Lifetime 110

B.3.2 Relationships Between Carrier Gas and Physiology 111

B.3.3 Simulations of MCA Circulation Time 112

B.4 Discussion and Conclusion 114

B.5 Acknowledgements 115

Bibliography 119

LIST OF FIGURES

1.1 Microbubble Schematic 2

3.1 Microbubble Size Distributions 25
3.2 Sonoporation Setup 26
3.3 Acoustic Parameters 29
3.4 Effects of Concentration 32
3.5 Effects of Size 35

4.1 BTM Nanocapsule Schematic 39
4.2 Flow Phantom Set-up for Ultrasound Parameter Testing 41
4.3 *In vitro* Nanoparticle Delivery 41
4.4 Nanoparticle Loaded Microbubble 43
4.5 *In vitro* Nanoparticle Delivery with Focused Ultrasound 45
4.6 Microbubble Drug Loading Curve 46

5.1 C22 Paclitaxel Nanocapsules 49
5.2 *In vivo* Treatment Setup 50
5.3 Average Tumor Volume 52
5.4 Dose Comparison 53
5.5 Tumor Histology 54

6.1 Clinical Ultrasound System Used for Enhanced Delivery 59
6.2 Confirmation of NP loading 61
6.3 *Ex vivo* Optical Imaging of AADV and Tumor Tissue 62
6.4 Optical imaging of tumor after NP delivery 63

6.5 AADV Biodistribution Imaging 64
6.6 DiR MB Delivery to Tumors 65
6.7 Optical Imaging of Liver and Tumor Tissue 66

7.1 Therapeutic Ultrasound Setup for PLD Delivery 72
7.2 PK Plots After PLD Treatment in C3Tag GEMM 78
7.3 Comparison of Delivery in Tumors With and Without US 81
7.4 PK Plots After PLD Treatment in Implanted C3Tag Tumor Model 82

B.1 Intensity Curve Example 111
B.2 Half Life Comparison 116
B.3 Simulated PFB 117
B.4 Simulated Gas Diffusion 118

LIST OF TABLES

3.1 Ultrasound Parameters 27

3.2 Microbubble Parameters 27

4.1 BTM Properties 42

7.1 PK Parameters C3Tag GEMM 76

7.2 GEMM C3Tag AUC Values 77

7.3 Concentration Ratios C3Tag GEMM 80

7.4 Concentration Ratios in Implanted C3Tag 80

7.5 PK Parameters Implanted C3Tag Mice 83

7.6 Implanted C3Tag AUC Values 84

8.1 Summary of Studies I 93

8.2 Summary of Studies II 94

A.1 Summary of *In Vitro* Studies 101

A.2 Summary of *In Vivo* Studies 102

B.1 Summary of Imaging Parameters 112

LIST OF ABBREVIATIONS

2-D	Two-Dimensional
3-D	Three-Dimensional
AADV	Acoustically Active Delivery Vehicle
ANG	Angiopoitin
ARF	Acoustic Radiation Force
AUC	Area Under Curve
B-mode	Brightness Mode
Brij 78	polyoxyl 20-stearyl ether
BTM	Brij TPGS Miglyol
C	Cycle
C22-PX	2'-benenoyl-paclitaxel conjugate
CL	Clearance
Cmax	Maximum Concentration
CPP	Cycles Per Pulse
CPS	Cadence Pulse Sequence
cRGD	Cyclo-Arg-Ala-Gly-Asp-D-Tyr-Cys
CW	Continuous Wave

DC	Duty Cycle
DiR	1,1'-Dioctadecyl-3,3,3',3'-Tetramethylindotricarbocyanine Iodide
DMEM	Dulbecco's Modified Eagle's Medium
DNA	Deoxyribonucleic Acid
DOX	Doxorubicin
DPPC	1,2 Distearoyl-sn-Glycero-3-Phosphocholine
DSPC	1,2 Distearoyl-sn-glycero-3-phosphatidylcholine
DSPE P2K	1,2 Distearoyl-sn-Glycero-3-Phosphoethanolmine-N-Methoxy-Polyethylene Glycol-2000
Em	Emission
EPR	Enhanced Permeability and Retention
Ex	Excitation
FDA	Food and Drug Administration
FGF	Fibroblast Growth Factor
FR	Frame Rate
FSA	Fibrosarcoma
GEMM	Genetically Engineered Mouse Model
GFP	Green Fluorescent Protein
GUI	Graphical User Interface

HIFU	High Intensity Focused Ultrasound
HL	Half Life
HPLC	High Pressure Liquid Chromatography
HUVEC	Human Umbilical Vein Endothelial Cell
IACUC	Plasmid DNA
IHC	Immunohistochemistry
JPEG	Joint Photographic Experts Group
MB	Microbubble
MCA	Microbubble Contrast Agent
MHz	Megahertz
MI	Mechanical Index
MPa	Megapascals
MPS	Mononuclear Phagocyte System
mRNA	Messenger RNA
NC	Nanocapsule
NP	Nanoparticle
PBS	Phosphate Buffered Saline
PDGF	Platlet Derived Growth Factor
pDNA	Plasmid DNA

PEG	Polyethylene Glycol
PK	Pharmacokinetics
PLD	PEGylated Liposomal Doxorubicin
PLGA	poly(lactic-coglycolic acid)
PRF	Pulse Repetition Frequency
PRP	Pulse Repetition Period
PS	Polystyrene
PW	Pulsed Wave
QD	Quantum Dots
R3230	Rodent Mammary Adenocarcinoma Cells
RES	Reticulendothelial System
RNA	Ribonucleic Acid
ROI	Region of Interest
siRNA	Small Interfering RNA
Spi	Sum of partial pressure
SPIO	Superparamagetic Iron Oxide
SPS	Solid Phase Separation
TIFF	Tagged Image File Format
TIPS	Therapeutic Imaging Probe System

Tmax	Time of Maximum Concentration
TPGS	D-α-tocopheryl polyethylene glycol 1000 succinate
US	Ultrasound
UV	Ultraviolet
Vd	Volume Distribution
VEGF	Vascular Endothelial Growth Factor

CHAPTER 1

Introduction

Ultrasound (US) imaging is one of the most widely used imaging modalities in the clinical setting. It is safe (does not use ionizing radiation), inexpensive, and portable. Ultrasound can be used as a primary diagnostic tool or in combinations with other modalities and procedures, such as with an ultrasound guided needle biopsy. While most individuals are familiar with the role of ultrasound in obstetrics and echocardiography, the capabilities of ultrasound reach far beyond those fields. Interestingly, ultrasound can be used both for diagnostic imaging and for therapy. In recent decades, the field of therapeutic ultrasound has made great progress with developments in both preclinical and clinical settings aided by the use of microbubble contrast agents.

1.1 Ultrasound and Microbubble Contrast Agents

Approved for use in echocardiography, microbubble contrast agents (MCA) are encapsulated gaseous microspheres that improve the quality of ultrasound images as a result of the difference in acoustic impedance between their gaseous core and the surrounding medium (blood) and because of their nonlinear oscillation in an acoustic field [1; 2; 3; 4; 5]. With diameters ranging from 1-10 microns, microbubbles are composed

of a protein, polymer, or lipid shell layer, and a gas core filled with a high molecular weight gas such as a perfluorocarbon or sulfur hexafluoride (Figure 1.1) [6].

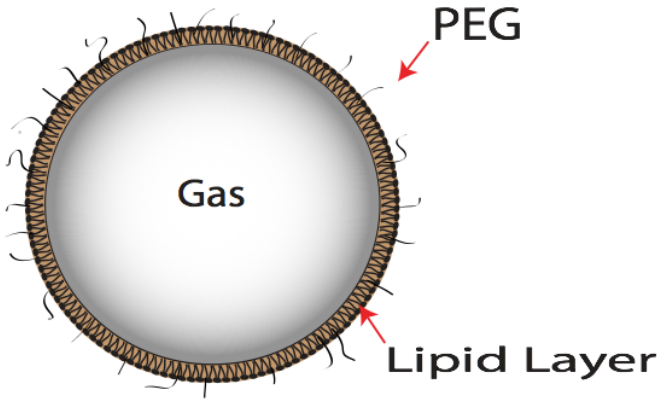

Figure 1.1: Microbubbles are composed of a gas core and stabilizing shell, such as a lipid layer. Polyethylene glycol (PEG) adds stability and reduces bubble aggregate formation.

Microbubbles have been utilized for imaging myocardial perfusion [7; 8]; left ventricular opacification [9; 10]; blood perfusion in tumors [11; 12], livers [13], and kidneys [14]; and for molecular targeting of angiogenesis [15; 16] or inflammation [17; 18; 19]. In recent years, the use of ultrasound microbubble contrast agents has expanded beyond their primary role in diagnostics and into the research fields of drug and gene therapy [1; 5; 2; 3].

1.1.1 History of Contrast Agent Development

The ability of an injected microbubble to improve ultrasound image quality was first described in 1968 by Gramiak and Shah [20]. Agitated saline air microbubbles improved left ventricular cardiac imaging in patients; however, these air bubbles had very limited circulation times. It was realized that by modifying the properties of microbubbles, circulation time could be increased. Microbubble encapsulation was

developed to prolong circulation lifetime of the bubbles. First generation contrast agents, Albunex microbubbles, were composed of a serum albumin shell and air core. Optison was later developed with a perfluorocarbon gas core. The incorporation of a higher molecular weight gas prolonged circulation as the modified gas core diffuses slower through the shell compared to air. Another important feature of microbubbles is the incorporation of polyethylene glycol (PEG), which prevents bubble aggregation and helps to avoid being phagocytosed while circulating. Definity, which is the contrast agent currently approved by the Food and Drug Administration (FDA) consists of a lipid shell and perflurocarbon gas core. Other agents, such as SonoVue (Bracco) are in use throughout the world, but are not approved in the United States. Additionally, many research groups, including our own, manufacture their own contrast agents for research purposes.

1.1.2 Response of Microbubble Contrast Agents to Ultrasound

Image Quality Improvement

The gas core effectively reflects sound waves due to the differences in impedance (a property based on density and the speed of sound) between the gas core and surrounding tissue and blood. Additionally, the compressibility of the microbubble due to the shell creates a nonlinear response of the microbubble as it expands and contracts within the ultrasound field. This nonlinear response produces harmonic signals that can be detected by ultrasound systems allowing contrast imaging to be a powerful clinical tool.

Cavitation and Microbubble Destruction

Exposure to higher amplitude signals leads to microbubble cavitation and/or eventual microbubble destruction. Cavitation can be either stable or inertial. In stable cavitation, the microbubble will oscillate without rupturing. In ineritial cavitation the the microbubble will expand more than it contracts, leading to violent collapse of the

microbubble. As a result, the microbubble may fragment and dissociate. Microbubble destruction can lead to changes in cellular and vascular permeability. The process of causing pore formation in cells is known as sonoporation, explored in Chapters 2 and 3.

Radiation Force

Acoustic radiation force, or the Bjerknes force, refers to the directional force experienced by objects in an ultrasound field. Microbubbles can be translated in the direction of the acoustic wave propagation due to the transfer of momentum from the sound wave to the bubble [21; 22]. In order to achieve translation, radiation force pulse sequences require a high duty cycle which is low in amplitude so as to not rupture the microbubbles. Radiation force applied perpendicularly to vessel orientation can result in microbubbles being pushed to the vessel walls, where they can accumulate [23].

This use of radiation force can be applied to many areas of ultrasound including molecular imaging [24; 25], drug delivery [26], in addition to the field of elastography to determine properties of tissues [27]. When applied to microbubbles, acoustic radiation force has been shown to increase the number of microbubbles present at a target site by up to a 100 fold compared to without radiation force *in vitro* [28], and up to 20 fold increase *in vivo* [29].

1.2 Cancer and Nanoparticles

1.2.1 Chemotherapeutic Drugs

Currently, cancer is the second leading cause of death in the United States [30]. While improvements to cancer detection and treatment have been made, there is still a long way to go. The primary treatment options for cancer patients are surgery, radiation treatment and chemotherapy. Often times a combination of these methods is

used [31].

Traditional chemotherapy drugs attack rapidly dividing cells, meaning cancerous as well as normal cells can be affected [32]. Hair loss, gastrointestinal issues, and myelosuppression are common side effects seen with chemotherapy treatment; nausea and vomiting are often cited as top distressing symptoms. These adverse effects can lead to esophageal tears, fractures, malnutrition, acid-base and electrolyte changes and patients' refusal to continue chemotherapeutic cycles, which decrease patient quality of life and compromises treatment efficacy [33].

There are many chemotherapeutics used in the clinic today, however, this research will focus on drug formulations involving doxorubicin and paclitaxel. Paclitaxel is most commonly used to treat lung, breast, ovarian cancer [34; 35]. One of the dose limiting side effects of this class of drug is peripheral nerve damage. Doxorubicin, an anthracycline, is an example of an anti-tumor antibiotic that interferes with enzymes associated with DNA replication. While this class of drug is used to treat many cancer types, cardiac damage is a concern for treatment [36]. Along with serious side effects from chemotherapeutics, limitations of traditional chemotherapy drug include limited solubility, lack of specificity and multidrug resistance [31; 37]. Ways to address these limitations are discussed later in this chapter and throughout this dissertation.

1.2.2 Tumor Microenvironment

When a cancerous mass grows larger than 2 mm^3, it can no longer get the oxygen and nutrients it needs, and experiences hypoxia. The hypoxic state triggers the release of numerous angiogenic factors such as VEGF-A (simply referred to as VEGF), fibroblast growth factor -2, angiopoietin 2, platelet derived growth factor, interleukin-8 and chemokines [38; 39; 40; 41; 42]. Increased presence of these factors triggers a switch to angiogenesis (new vessel formation) [43; 39; 41]. VEGF plays the primary role of

mediating tumor angiogenesis by binding to vascular endothelial growth factor receptor 2 (VEGF-2), which is presented on endothelial cells. Binding to the receptor starts multiple signaling pathways leading to up-regulation of genes triggering proliferation and migration of endothelial cells [42]. Vasodilation occurs along with an increase in permeability of existing capillaries. This is followed by extravasation of plasma proteins which provide the matrix for migrating endothelial cells [43; 39]. The TIE-2 receptor, also expressed on the vascular endothelium is linked to the tyrosine kinase signaling pathway. Angiopoioetin-1 and angiopoietin-2 bind to the TIE-2 receptor, signaling loosening of the pericytes along the vessels [43]. When endothelial migration occurs, a tip cell is selected and the neighboring cells (stalk cells) divide.

Vessels formed during tumor angiogenesis are abnormal in several ways. Tumor vasculature is disorganized, tortuous, dilated, and heterogeneous due to the imbalance of pro- and anti-angiogenic factors present in tumors [38; 41]. Tumor blood flow can also be an order of magnitude slower than in normal vasculature [38]. Tumor vasculature is characterized by large inter-endothelial junctions, increased number of fenestrations and abnormal basement membrane formation [38]. The endothelial cells recruited during angiogenesis are also abnormal, with altered receptor activity, signaling pathways, gene expression, and structure [44]. Pericytes are cells that in normal vasculature are closely associated with vessels, providing stability. In tumor vessels however, fewer pericytes are present, and they are loosely associated, leading to gaps [42]. The decrease in number and association of pericytes causes abnormal vessel diameters [43]. There is also a lack of smooth muscle cells, which would help regulate blood flow in normal vasculature [41]. Abnormalities continue to be seen in the basement membrane where the collagen thickness and proximity to endothelial cells may vary [44]. Due to inadequate vessel formation, the tumor environment remains hypoxic, which can reduce sensitivity to radiation treatment and other therapies, along with hinder the ability of

immune cells [38]. The continued hypoxic state triggers VEGF and other factors from tumor cells and recruited host cells (such as inflammatory cells), further promoting the angiogenesis cycle [39].

Enhanced Permeability and Retention Effect

The abnormal characteristics of tumor angiogenesis contribute to what is known as the enhanced permeability and retention (EPR) effect, first described by Matsumura and Meada in 1986 [45]. Due to the leaky vessels and large fenestrations (from abnormalities described above), tumor vasculature is more permeable than healthy vessels. The gaps or pores found in tumor vessels has been found to often range from 100 nm up to 2 μm, depending on the tumor type and location [38]. Some reports have even cited endothelial openings as large as 4.7 μm [46]. The enhanced retention comes from the lack of lymphatic clearance in the tumor tissue. The lymphatic system within tumors is nonfunctional (does not transport fluid or macromolecules) due to compression of lymphatic vessels, which causes an increase in interstitial pressure. [38; 41].

1.2.3 Nanoparticles

These characteristics provide an environment that can be exploited by nanoparticles. Although strictly defined by the National Cancer Institute as any particle with at least one dimension under 100 nm, this dissertation will use the term nanoparticle to describe any sub-micrometer vehicle. Nanoparticles are often capable of carrying a therapeutic payload and vary in shape, size, and physical and therapeutic properties. Some common types of nanoparticles are micelles, liposomes, dendrimers, solid nanoparticles, nanocapsules and emulsions [47; 48]. Nanoparticles can be easily modified to effect bioavailability, cytotoxicity, clearance and recognition by the immune system [49]. Additional modifications can make nanoparticles multifunctional serving both therapeutic and diagnostic purposes with the capability to include multiple

targeting ligands and drug combinations [50].

Nanoparticles are often used as delivery vehicles by encapsulating a therapeutic compound that may otherwise cause systemic toxicity if delivered in free form. Nanoparticle delivery vehicles show promise for carrying high therapeutic payloads, controllable release rates, and targeting abilities - both passive and active [48]. Passive targeting refers to the uptake of particles based solely on their size. Active targeting involves adding a component to the particle that will bind to a specific biological tag that is overexpressed in the tumor such as integrins, folic acid, or antigens.

In cancer therapy, the small size of nanoparticles is particularly advantageous within tumor vasculature. The EPR effect enables passive targeting of nanoparticle drugs to tumors. The particles cannot pass through normal vasculature with endothelial junctions of 5-10 nm, but accumulate within the tumor tissue through the leaky vasculature [47]. This is significant because harmful side effects seen in traditional chemotherapy can be greatly reduced. Nanoparticles ranging from 10-100 nm in size are ideal for delivery to tumors. Being larger than 10 nm evades renal clearance, and under 100 nm avoids hepatic clearance [47]. The long circulation time is an important property to allow the particle time to accumulate within the tumor. Polyethylene glycol (PEG) on the surface of the particle helps to avoid the mononuclear phagocyte system and thereby prolong circulation. Size is also a major determining property to not only ensure extravasation, but to increase penetration into the tumor tissue.

Preclinically, there are countless formulations of chemotherapeutic nanoparticles being investigated. Animal models provide the means for scientists to investigate the impact of various nanoparticle characteristics on tumor delivery and effectiveness of treatment. There are also several examples of passively targeted nanomedicines used in the clinic, some of which are in clinical trials while other are approved for patient use. Liposomes were the first nanoparticles to be approved for cancer therapy by the

FDA [47]. Liposomes include Doxil, Myocet, DaunoXome, Onco-TCS, and Marquibo. Myocet and Doxil are both liposome formulations of doxorubicin, however Doxil is PEGylated. DaunoXome is PEGylated daunorubicin. Examples of other approved nanoparticles include Abraxane- an albumin bound paclitaxel nanoparticle, Transdrug- a doxorubicin nanoparticle, and Nanoxel- a paclitaxel nanoparticle. Despite the success of these formulations, the translation of nanomedicine into the clinical setting has been unexpectedly slow [51].

There are numerous factors that contribute to the limited clinical success of nanoparticles for cancer therapy. Although nanoparticles may be able to exit through the leaky vasculature of the tumor, there are still other barriers to delivery. The tumor microenvironment is composed of a matrix of collagen fibers, proteoglycans and glycosaminoglycans, which can hinder nanoparticles from reaching tumor cells [51]. Nanoparticles must travel through this matrix and enter into tumor cells must occur for chemotherapeutics to have their full therapeutic effect.

Scientists have also observed an overestimation of the EPR effect in murine models compared to human tumors. Rapidly growing tumors, such as subcutaneous tumor in mice, produce large quantities of VEGF and other mediators which enhance permeability effects [51; 52]. Heterogeneity within tumors and tumor types has also been observed. Tumor location and host environment can also impact permeability. For example, glioma tumors grown subcutaneously are more leaky than orthotopic tumors [38].

Additionally, although nanoparticles do limit exposure of many healthy cells, they still accumulate in other organs such as the liver and spleen. Studies have shown that less than 5% of the injected dose accumulates in the tumor. These limitations of nanoparticles in cancer therapy have lead researches to look of ways to improve nanoparticle delivery into tumors.

1.3 Scope

Combining ultrasound and microbubbles with nanoparticles has the potential to overcome the limitations of current therapy practice for cancer, as well as many other conditions. While the field of ultrasound mediated drug delivery has been expanding, there are still many unknowns, and much room for improvement. This research aims to optimize ultrasound and microbubble parameters to improve targeted nanoparticle drug delivery. We hypothesize that improved chemotherapeutic delivery, with reduced systemic toxicity, can be achieved by utilizing ultrasound to concentrate and disrupt microbubble contrast agents at a target site in the presence of a nanoparticle drug. This dissertation will present research on a variety of nanoparticle formulations, both novel and commercially available, combined with the use of microbubbles and a variety of ultrasound systems ranging from piston transducers to clinical scanners.

This chapter has introduced the importance of microbubble contrast agents and nanoparticles. In Chapter 2, progress in the field of ultrasound mediated nanoparticle drug delivery will be discussed further.

In Chapter 3, the ability of ultrasound to enhance local nanoparticle delivery *in vitro* is explored. Acoustic parameters are optimized to enhance cellular internalization of molecules through sonoporation. Microbubble parameters are also investigated to achieve optimal internalization.

Chapter 4 will illustrate the combined effects of acoustic radiation force and microbubble destruction for targeted delivery *in vitro*. An acoustically active delivery vehicle is created that is comprised of a microbubble coated in nanoparticles.

Chapter 5 demonstrates the potential of ultrasound as a therapeutic tool *in vivo* through treatment of tumor bearing mice. Combined ultrasound treatment is compared to nanoparticle only treatment.

Chapter 6 describes preliminary studies conducted using nanoparticle-loaded microbubbles combined with acoustic radiation force and microbubble destruction. These studies are carried out using a clinical ultrasound scanner to deliver nanoparticles within tumors in preclinical cancer models.

In Chapter 7, pharmacokinetic analysis of nanoparticle drug delivery combined with therapeutic ultrasound in a mouse breast cancer model is explored. Liposomal doxorubicin treatment is compared to a co-injection of microbubbles and liposomal doxorubicin combined with focused ultrasound treatment.

Chapter 8 will summarize the work presented in this dissertation and discuss the limitations and challenges of ultrasound mediated drug delivery and the path towards clinical translation.

Other work related to improving ultrasound imaging methods is present in the appendix.

CHAPTER 2

Ultrasound Drug Delivery

2.1 Introduction

Ultrasound is being explored as a platform for enhancing therapeutic delivery. Studies investigating gene and drug delivery aided by ultrasound are rapidly gaining popularity. A subset of the drug delivery field focuses on nanoparticle delivery. This chapter provides a more in depth explanation of the role of ultrasound and provides a review of this body of literature.

2.2 Ultrasound and Nanoparticles

In the field of therapeutic ultrasound with microbubbles, the most commonly used types of nanoparticles are quantum dots [53], liposomes [54; 55; 56; 57], and poly(lactic-coglycolic acid) (PLGA) nanoparticles [58; 59]. Quantum dots are often used in studies in place of nanoparticle drugs to characterize delivery vehicles and evaluate successful delivery into targeted tissue. Doxorubicin-containing liposomes have been used extensively in ultrasound and microbubble delivery studies (see Appendix A). One reason for their popularity in research studies is that several forms, known as Doxil or Caelyx,

DaunoXome, and Myocet, are already FDA approved for clinical use. Doxorubicin is also inherently fluorescent, which makes optical tracking of delivery feasible. Another form of liposome used with microbubble ultrasound delivery is the lipoplex, which is a liposome containing genetic material such as plasmid DNA [60; 61; 62]. This method protects the DNA during *in vivo* circulation and allows a greater amount of genetic material to be delivered [60; 61].

2.2.1 Mechanisms of Delivery

Ultrasound exposure in the presence of microbubbles can increase both cellular and vascular permeability, leading to enhanced nanoparticle delivery. An increase in cell permeability ensues from the formation of pores in the cell membrane during a process called sonoporation. At higher pressures, ultrasound alone can cause the formation of pores within the cell membrane [63]. This effect is enhanced with the addition of microbubbles. Although the exact mechanisms are not fully understood, the oscillation of microbubbles in an ultrasound field creates transient pores in the lipid bilayer [64; 65; 66]. The degree of sonoporation is dependent on the cavitation behavior of the microbubbles, which is in turn dependent on the acoustic conditions applied. Both stable and inertial cavitation have been shown to result in pore formation [1; 26]. During stable cavitation, the microbubble oscillates without disruption, whereas during inertial cavitation, the microbubble is unstable and fragments [1]. Streaming of fluid around the bubble can occur in both cases and causes shearing of the cellular membrane [67; 68]. When microbubbles near cellular membranes are exposed to high-energy pulses, they often form microjets during collapse, resulting in high shear stresses from streaming and shockwaves that are thought to lead to pore formation [69; 70]. In addition to creating openings in cells, the cavitation response of microbubbles may also facilitate uptake by forcing the nanoparticles into the cell through microjets [71].

Pore formation can be either transient (reversible) or permanent. Transient pore formation has been observed *in vitro*, wherein pores remained open for seconds to hours. In some instances, pore openings have been reported up to 24 h after ultrasound exposure [72]. Permanent pore formation is undesirable in most applications, because it leads to cell death. Consequently, care must be taken in selecting appropriate acoustic conditions because cell death can occur with sufficiently high or long ultrasound exposure [67; 68; 73]. For example, Deng *et al.* observed an increased transmembrane current in cells subjected to both ultrasound and the presence of microbubbles indicating increased membrane porosity [74]. Cells recovered to resting levels in about 4 to 10 s following insonation for approximately 1 s at 1 MHz and 1 MPa pressure, but higher ultrasound intensities (>1 MPa) for durations longer than 0.5 s resulted in irreversible cell damage and cell death. In general, reagent delivery increases with increasing acoustic pressure, but so too does the likelihood of cell apoptosis [73; 74; 75; 76; 77].

Many groups are also investigating cellular changes that occur as a result of ultrasound exposure, including changes in calcium levels, cell signaling pathways, and endocytosis [65; 78]. In a study on gene delivery to BLM melanoma cells, Lentacker *et al.* found that lipoplexes were directly entering the cell cytoplasm through sonoporation rather than endocytosis [61]. The uptake was seen to occur during or immediately after ultrasound exposure. Meijering *et al.* also observed small molecules (4.4 and 70 kDa) entering the cell membrane via pores, however they found that larger molecules (155 and 400 kDa) were entering into the cell through vesicle formation in endocytosis [65]. The role of calcium in sonoporation has been investigated and calcium is believed to aid in cell recovery after pore formation [79]. Other cellular changes that have been observed are hyperpolarization of the cell membrane, release of free radicals, and increased levels of hydrogen peroxide [79; 80]. Yang *et al.* recorded differences in cell viability and permeability depending on the stage of cell growth, indicating the cell cycle may

play a role in cell permeability [79]. With respect to vessel permeability, effects can range from mild reversible permeability enhancement to gross vessel rupture, depending on the microbubble and acoustic parameters [81; 82; 83; 84; 85]. Results from many groups have suggested that large molecules (such as dextrans), as well as nanoparticles, enter into the interstitial space after sonication with microbubbles [86; 87; 88; 89]. This vascular permeability is expected to be a result of the interaction between microbubbles and vessel walls. Caskey *et al.* studied the effects of insonated microbubbles within *ex vivo* vessels and observed both asymmetric collapse and jet formation near the vessel wall [90]. Chen *et al.* also studied microbubbles within *ex vivo* vessels and observed that jet formation occurs away from the vessel wall [91; 92; 93].

Acoustic radiation force also enhances nanoparticle delivery. Radiation force, explained in Chapter 1, refers to the ability to push an object, such as a microbubble, within an ultrasound field. When nanoparticles are attached to the microbubble, the local concentration of nanoparticles can be increased by pushing the microbubbles against the vessel wall in one location [23; 28; 94]. This phenomenon has been shown to aid in delivery of nanoparticles when microbubbles are used [54; 95; 96; 97].

2.2.2 Types of Administration

There are two main administration methods employed for nanoparticle delivery with ultrasound and microbubbles: unbound and bound nanoparticles. In the first method, the nanoparticles are not associated with the microbubbles, but are either injected separately or co-administered. If separate injections are performed, the order of injection may vary as long as microbubbles are present when ultrasound is applied. Lin *et al.* showed no significant difference in tumor accumulation between quantum dot injection before or after insonation as long as microbubbles were present during the ultrasound [98]. The second method of delivery requires the nanoparticles to be

attached to the microbubble before injection and ultrasound treatment. There are numerous ways to associate the nanoparticle with the microbubble. One of the most common methods to attach a nanoparticle to the microbubble is with the use of biotin avidin interactions.

Biotinylated microbubbles are used to attach either avidin or streptavidin nanoparticles, or in some cases an avidin linker is used to link biotinylated particles [54; 57]. Although biotin avidin linkage is suitable for proof of concept studies, it is not ideal for *in vivo* use because it can induce an immunogenic response [54; 99]. An alternative to this method is to use maleimidethiol chemistry. Maleimide conjugation is often used in molecular imaging studies to create targeted microbubbles and can also be applied to nanoparticle attachment to the shell of the microbubble [56]. Another covalent binding possibility was illustrated by Burke *et al.*, in which PLGA nanoparticles were coupled to albumin microbubbles through carbodiimide chemistry [58]. Oligonucleotides have also been employed as tethers to link vesicles to microbubbles through hybridization of complementary lipid-linked DNA oligonucleotides [100].

Electrostatic binding of nanoparticles to microbubbles is often implemented in gene delivery studies, wherein negatively charged DNA is attached to positively charged microbubbles with shells composed of a cationic lipid. Electrostatic interactions can also be exploited to create nanoparticle-bound microbubbles. One example of this was described by Seo *et al.* who created positively charged monodisperse microbubbles through microfluidics and attached negatively charged silica-coated nanoparticles [101]. This technique was shown to be effective for various sizes and shapes of nanoparticles.

Drugs can also be directly incorporated into the shell of the microbubble, although this provides a challenge in the inherently limited payload capacity. Drug-loaded polymer-shelled microbubbles, whose thicker shells allow for higher drug loading, fragment into nanoshards, which are less than 400 nm in size [102; 103; 104]. These shards

are small enough to extravasate from the vasculature of the tumor.

There are some definite advantages to linking the nanoparticle to the microbubbles. Along with being able to track the nanoparticle in circulation by ultrasound imaging of the microbubble carriers, attaching the nanoparticle ensures that they are present at the target site during insonation. Using ultrasound to rupture the microbubble at a desired location leads to targeted deposition of particles. As discussed previously, linking the nanoparticle to the microbubble also allows for radiation force to be used to increase particle/drug concentration at the desired site. Lum *et al.* and Kheirolomoom *et al.* demonstrated higher delivery of nanoparticles *in vitro* using radiation force in combination with microbubble-loaded nanoparticle constructs compared with without using radiation force [95; 54]. Linking nanoparticles to microbubbles is also advantageous because it prevents dilution of the nanoparticle solution when it enters the bloodstream [58]. Finally, microbubbles loaded with certain nanoparticles may serve as multi-modality contrast agents for platforms such as dual MRI-ultrasound and optical-ultrasound [105; 106; 107].

There are also some challenges related to associating the nanoparticle to the shell. When linking through a process such as biotin and avidin, multiple washing steps are necessary to remove free linking agent. This can be both time consuming and detrimental to the fragile bubble preparation, requiring a higher initial concentration of microbubbles. Furthermore, excess nanoparticles are typically required to maximize loading. Finally, attaching the nanoparticle to the microbubble may alter the *in vivo* circulation time and biodistribution.

2.3 Ultrasound Setups

There are a variety of ultrasound systems in use to accomplish microbubble-aided nanoparticle delivery. Many researchers use single-element transducers powered by

arbitrary waveform generators and amplifiers, whereas others use commercial therapy systems or even clinical imaging systems (see Appendix A). In [108], Seip *et al.* describe ideal qualities of a therapy system, including the ability to both image and treat a desired location to monitor delivery and release of the agent. The system should be able to generate intensities and pulse sequences needed for microbubble delivery, deliver focused energy deep within tissue to target a specific area, treat in an acceptable amount of time, be incorporated into current treatment workflow, and be easy to use and set up. Most therapeutic treatments involve ultrasound with a center frequency of around 1 MHz, which is much lower than clinical imaging systems typically provide. Although some custom systems have been created, dual imaging and treatment often requires multiple transducers to be used in conjunction with one another [109]. Nanoparticle delivery has been performed with both focused and unfocused transducers, as well as at varying pressures up to 7 MPa.

2.4 Review of Successful Nanoparticle Delivery Studies

Some of the first nanoparticle delivery studies were performed *in vivo* with fluorescent nano/microspheres (100 to 500 nm) delivered to rat skeletal muscle [86; 110]. In these studies, vessel rupture caused by microbubble breaking was observed and the particles were delivered into the intersitium of the muscle. Extravasation points were observed where particles and red blood cells leaked out of the vasculature. Findings also illustrated the importance of allowing microbubbles to replenish in between ultrasound pulses and quick (10 s) injection of particles to increase deposition. Delivery of fluorescent nanospheres (30 to 120 nm) to cardiac muscle was later shown by Vancraeynest *et al.* [87].

The feasibility of *in vivo* nanoparticle drug delivery with microbubbles and ultrasound was demonstrated using PLGA nanoparticles loaded with fibroblast growth

factor-2 [111]. Initial studies depicted 40-fold and 670-fold increases in nanoparticle delivery to the mouse adductor muscle when ultrasound or ultrasound and microbubbles were applied compared with nanoparticles alone. Subsequently, drug- loaded nanoparticles were delivered into the ischemic hind limb of the mouse with the addition of ultrasound and microbubbles. Results of the studies showed an increase in total number of large and moderate diameter arterioles, as well as marked luminal expansion of pre-existing collateral arteries and transverse arterioles. Although the growth factor did not induce angiogenesis in gracilis muscles, arteriogenic remodeling was seen along with an increase in arteriole-line intersections.

Successful nanoparticle gene delivery was demonstrated *in vitro* with plasmid DNA (pDNA), short interfering RNA (siRNA) and messenger RNA (mRNA), often involving a fluorescently tagged gene so that transfection can be easily quantified [60; 61; 62; 112; 113]. Encapsulating the genetic material within a liposome, creating a lipoplex, or siPlex, protects the genetic material and allows more to be delivered to the target site. Ultrasound-mediated delivery with microbubbles was found to overcome the limitations of PEGylated liposomes. Although PEG increases circulation of the lipo/siPlexes, it hinders cellular uptake. When cells in an Opticell were exposed to ultrasound, liposomes loaded with up to 15 mol% PEG had limited gene expression/ inhibition with free liposomes, but exposure to loaded microbubbles and ultrasound led to statistically significant differences. These studies also demonstrated the direct entry of liposomes into the cytoplasm when ultrasound and microbubbles are present [61]. Uptake and expression were investigated further with mRNA lipoplexes loaded onto microbubbles [62]. Uptake was observed in 50% of the cells when loaded microbubbles and ultrasound were applied, compared with 0% uptake with lipoplexes alone, and 24% of the cells illustrated successful transfection. These results support the hypothesis that not all of the contents are released from liposomes upon insonation.

Liposomal-loaded microbubbles have also proven to be advantageous for drug delivery. As mentioned in an earlier section, Doxil, and other doxorubicin-containing liposomes are commonly used in ultrasound and microbubble delivery studies. When doxorubicin-containing liposomes were bound to microbubbles and delivered to melanoma cells in an Opticell, significantly higher cytotoxicity was seen [114]. Additional findings indicated that enhanced delivery was caused by both release of doxorubicin from liposomes and sonoporation caused by the microbubbles. The released free doxorubicin enters into the cell more efficiently than the liposome-contained doxorubicin. Studies carried out with self-assembling liposome-loaded microbubbles revealed a lower dose of doxorubicin could be used when the liposomes were bound compared with free liposomes [56].

Recently, enhanced *in vivo* delivery of liposomal doxorubicin has also been observed. After several studies with lipid-coated quantum dots delivered in mice, studies were carried out with Doxil and microbubbles with ultrasound exposure [115]. The concentration of Doxil in tumor tissue over time, the impact on tumor size on various treatments, and dose were investigated. Using focused ultrasound, more Doxil was delivered when microbubbles were administered, and colorectal adenocarcinoma tumor growth in mice was hindered. At 24 h after treatment, more drug was concentrated within the tumor compared with treatments of Doxil alone, however, the concentrations of both treatments were similar by 48 h. It was also observed that smaller tumors responded better to treatment than larger tumors at 5 mg/kg. Larger tumors required a higher treatment dose of 10 mg/kg. Tumor histology revealed extravasation of fluorescent Doxil.

Delivery of doxorubicin-containing nanoshards has also been carried out *in vivo*. Polymer microbubbles containing doxorubicin in the shell were destroyed within VX2 tumor-bearing rabbits, which created nanoshards capable of extravasating into tumor

tissues. Initial studies revealed significantly higher concentration of doxorubicin within the periphery of the tumor following ultrasound treatment compared with no insonation [104]. In later work, significant differences in tumor growth were also observed between mice treated with drug-loaded microbubbles and ultrasound compared with free drug at 14 days [116]. Paclitaxel-loaded polymer microbubbles are also being developed which can hold up to 20 times as much drug as doxorubicin-loaded microbubbles [102].

Nanoparticle drug delivery has also recently been applied to fields outside of chemotherapy [117]. Microbubbles loaded with rapamycin-coated magnetic ion nanoparticles are being investigated as a treatment option for ischemic coronary heart disease. Using magnetic stents, the nanoparticle-loaded microbubbles are targeted to the desired location, and then the drug is released when the microbubbles are ruptured using ultrasound. *In vitro* studies have shown cell growth inhibition with rapamycin-loaded nanoparticles, whereas testing of the magnetic stents confirms microbubble accumulation at the stent. Increasing the flow conditions lead to an increase in nanoparticle deposition.

2.5 Summary

In this chapter, the concept of combining ultrasound with nanoparticles for targeted drug delivery was explored. Future chapters will focus on studies to improve these methods by obtaining a better understanding of the role of the ultrasound settings and microbubbles to increase permeability to enhance nanoparticle delivery to cells and tumor tissues.

CHAPTER 3

Ultrasound and Microbubble Parameters for Maximizing Sonoporation

3.1 Introduction

Ultrasound mediated drug delivery can utilize various ultrasound techniques to achieve enhanced delivery. Combining acoustic radiation force with microbubbles destruction has the potential to increase concentrations of therapeutics at the target site when the therapeutic load is combined with the microbubble [26; 95; 96]. This method uses radiation force to translate microbubbles to the targeted vessel walls followed by destruction of the microbubbles close to the cells creates desirable bioeffects which enhance delivery, such as pore formation.

Although increased permeability has been observed by many researchers, the mechanisms behind sonoporation are not yet fully understood and are still being investigated. Evidence would suggest, however, that microbubble cavitation plays an important role in sonoporation. Both stable and inertial cavitation can result in pore formation [26; 1]. In stable cavitation, the microbubble gently oscillates, whereas in inertial cavitation the microbubble violently collapses. Possible mechanisms leading to pore formation are microjets, streaming, and shear force [69; 70; 118]. In addition, changes in calcium levels, cell signaling pathways and endocytosis have also been observed [65; 78; 119].

Along with the mechanisms leading to pore formation, there are other factors related to sonoporation that are also being studied. It is known that various ultrasound

settings can affect delivery into cells. Frequency, duty cycle, and pressure are three factors which have been shown to impact sonoporation [65; 120; 121; 122; 73; 123; 124]. Microbubble composition is another important factor to consider when optimizing delivery. Microbubbles can be made with various shell and gas core components, and the size can be altered through a number of techniques including centrifugation and microfluidics [6]. The effect of microbubble size has been shown in imaging studies as well as blood brain barrier delivery studies [83; 24]. Larger microbubbles lead to greater contrast in images and also demonstrate better efficiency at disrupting the blood brain barrier. Too many microbubbles can cause a shadowing effect due to signal attenuation, whereas too few microbubbles may not provide enough contrast to see the desired area. Similarly, microbubble concentration may also play a role in efficacy of sonoporation [125; 126; 127].

Although these parameters have been studied previously by various groups as listed in the prior paragraph, to date no group has evaluated all of the parameters described here with the same experimental system. Thus, variations in experimental setups make it challenging to compare the effects of parameters across studies. Differences in cell type, cell seeding method (single cell, cell suspension, or adhered cells), microbubble properties, transducer orientation, and ultrasound parameters all contribute to inconsistent results. The aim of this study was to optimize *in vitro* cellular uptake by controlling parameter settings including cell-bubble exposure time, pulse repetition frequency (PRF), acoustic pressure, microbubble size distribution, and microbubble concentration. An *in vitro* setup containing an inverted monolayer of cells on a coverslip positioned above an unfocused 1 MHz transducer was used. This setup allows for microbubble flotation to produce bubble-cell proximity. Studies were performed to determine which parameters had the greatest impact of cellular uptake of calcein molecules in order to guide future *in vitro* and *in vivo* experiments.

3.2 Materials and Methods

3.2.1 Cell Culture

A549 human non-small lung cancer cells were purchased from ATCC (CCL-185). The cells were cultured in Dulbecco's Modified Eagle's Medium (DMEM) with 4.5 g/L glucose supplemented with 10% fetal bovine serum and 1% antibiotic media at 5% CO_2, 37°C. Cell monolayers were cultured on acoustically transparent Thermanox coverslips (Nunc, Thermo Fisher Scientific) until nearly confluent. Studies involving the effects of cell density were performed by seeding coverslips at low cell density and selecting them for use once cells reached the desired confluency. Cell confluency studies were performed on days 1-5 after seeding on coverslips.

3.2.2 Microbubble Preparation

Microbubbles were prepared with 1,2 Distearoyl-sn-glycero-3-phosphocoline (DSPC) and 1,2 Distearoyl-sn-Glycero-3-Phosphoethanolmine-N-Methoxy (Polyethylene glycol)-2000 (DSPE-PEGK) purchased from Avanti Polar Lipids, Inc. (Alabaster, AL) (9:1 molar ratio). Phosphate buffered saline (PBS) was added to the lipids to create a concentration of 1 mM (1 mg/mL). Smaller microbubble solutions (mean diameter less than 1 μm) were formed by flowing decafluorobutane through the dissolved lipid solution and activated via mechanical agitation using a VialMix as previously described [128]. Larger microbubbles (mean diameter greater than 1 μm) were formed using a sonic dismembrator for 10 seconds at 70% power in the presence of decafluorobutane, which produced a microbubble solution that was then centrifuged at settings described by Streeter *et al.* and Feshitan *et al.* to isolate desired populations of microbubbles [24; 129]. An Accusizer 780A device (Particle Sizing Systems, Santa Barbara, CA) was used to measure concentrations and size distributions of the microbubbles (Fig. 3.1).

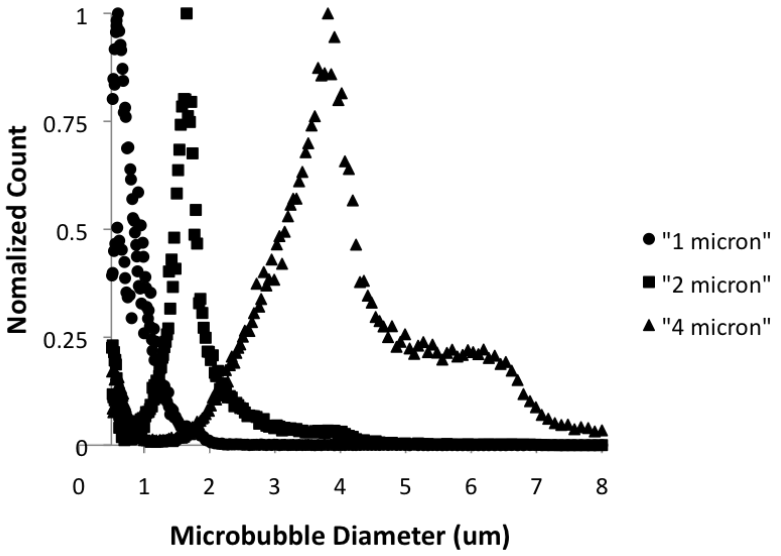

Figure 3.1: Microbubble size distributions re obtained using an Accusizer 780A device. Microbubbles (circles) with a mean diameter of 0.79 μm, were used in all experiments unless otherwise stated and are referred to as the 1 μm microbubble population. Larger microbubbles around 2 μm (squares) and 4 μm (triangles), mean diameters of 1.6 and 3.6 μm, respectively, were used to study the effects of mic size on sonoporation.

3.2.3 Sonoporation Setup

Calcein, a fluorescent molecule which does not normally enter cells, was used to monitor the effects of sonoporation. Calcein was dissolved in Dulbeccos phosphate buffered saline (DPBS) at a concentration of 1 mg/mL. A 1 MHz, 1 inch diameter unfocused transducer (Olympus-Panametrics) was positioned beneath a Bioflex tissue culture plate (Flexcell, Hillsborough, NC), with coupling gel between the transducer face and the bottom membrane of the well (Fig. 3.2A). Cell coated coverslips were positioned face down on a stand-off within a well (Fig. 3.2B). A solution with 25 μL of microbubbles mixed with 1 mL of calcein was added to the well beneath the coverslip. The cells were incubated with the calcein-microbubble solution for 10 minutes before being sonicated for 3 min. After ultrasound exposure, the coverslip was removed from the well and washed in PBS for 2 min on a rotating platform to remove excess calcein.

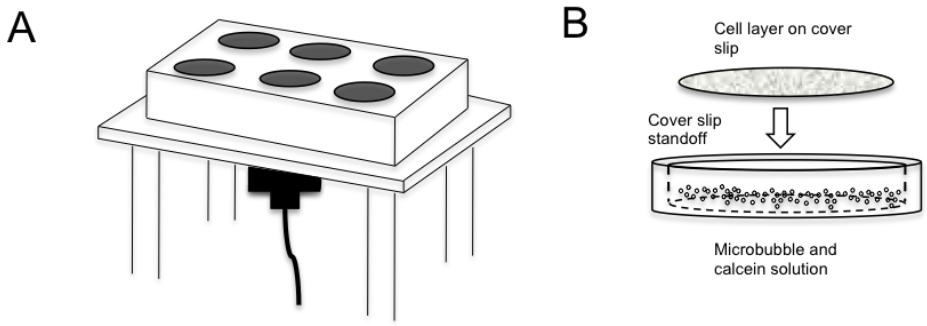

Figure 3.2: (A) The *in vitro* setup consisted of a 1 MHz transducer positioned underneath a six well plate with soft membrane bottom. (B) A standoff was positioned inside the well to hold the cell coated coverslip above the microbubble-calcein solution.

The transducer was excited with 5-cycle sinusoidal pulses from an arbitrary waveform generator (AWG2021 Tektronix, Beaverton, OR) and a 55 dB RF amplifier (3200L, ENI, Rochester, NY). An additional arbitrary waveform generator (33120A, Hewlett Packard, Palo Alto, CA) was used to control the pulse repetition frequency (PRF). Pressure values were measured with a needle hydrophone positioned 8 mm from the face of the transducer in a water bath.

Ultrasound parameters tested included incubation time, pulse repetition frequency, pressure, and number of repeated exposures. Table 3.1 and Table 3.2 display the parameters studied. Unless otherwise indicated, setting used were 10 minute incubation, PRF of 150 kHz, and 300 kPa. Microbubble distributions with 2 and 4 μm diameters were tested and concentrations between 6 x10^6 and 1x10^{10} MB/mL were also studied. Additional examination of the role of cell confluency on sonoporation was performed on coverslips with varying degrees of cell coverage. Control experiments were carried out with calcein incubation followed by ultrasound exposure without microbubbles.

Table 3.1: Summary of acoustic parameters investigated

Incubation	1 min	5 min	10 min	15 min
PRF	0.15 Hz	1.5 Hz	15 Hz	150 Hz
Pressure	150 kPa	310 kPa	850 kPa	1200 kPa
Repetitions	1	2	3	

Table 3.2: Summary of microbubble parameters investigated

MB Concentration	$1x10^{10}$ MB/mL	$2.5x10^{8}$ MB/mL	$6x10^{6}$ MB/mL
MB Size	1 μm	2 μm	4 μm

3.2.4 Image Analysis

Both bright field and fluorescent micrographs of the coverslip were acquired with a fluorescent microscope (Olympus BX51). Multiple images were acquired for each coverslip. Fluorescent images were acquired and compared by summing the pixels within areas of intensities above the noise threshold using Metamorph Basic (Molecular Devices, Sunnyvale, CA). The pixel counts for each image acquired were averaged to obtain a quantitative value for fluorescence for each coverslip. Once individual averages were obtained, coverslips for each parameter were averaged and normalized to the baseline setting. Analysis of cell confluency studies was carried out with an in house MATLAB script developed to segment cell borders and calculate cell count and area covered per coverslip. A mask was created to only measure fluorescence in areas where cells were present.

3.2.5 Statistical Analysis

Each of the 5 images taken on each coverslip were averaged for overall average value of the coverslip. The coverslips average values were then averaged together for similar settings. Settings were compared using a Student's t-test with a Bonferroni correction. Values of $p<0.05$ were considered significant.

3.3 Results and Discussion

Finding the optimal ultrasound parameters for *in vitro* delivery using microbubbles is an important step to improving drug delivery techniques. Although there are additional challenges that will need to be overcome for *in vivo* studies, demonstrating successful *in vitro* delivery provides promise for future work. Calcein was used as a fluorescent drug marker because it does not enter into cells under normal conditions and is easily detectable within cells. Other groups have also demonstrated that calcein is an appropriate permeability tracer [125; 130; 131].

Increasing PRF did not lead to a consistent increase in calcein uptake (Fig. 3.3A). This data suggests that sonoporation may require only a few acoustic pulses to occur, and increasing the number of acoustic pulses has no further cumulative effect. It was also stated by Rahim *et al.* that the first 10 cycles were the most important [124]. Additionally, Fan *et al.* found that shorter pulses were more effective than longer ones, as they avoid unwanted translation [132]; this finding supports the use of short pulse length. Other groups, however, have seen an increase in sonoporation with increasing the duty cycle [122]. Unlike in these experiments, Pan *et al.* increased the duty cycle by increasing pulse length instead of adjusting the PRF. These conflicting findings suggest that variations in *in vitro* setups may contribute to variations in optimal settings. In a static chamber like the one used in these experiments, PRF may not play as important a role as it would when microbubbles are non-stationary as in a flow chamber or vertical setup, or even *in vivo*.

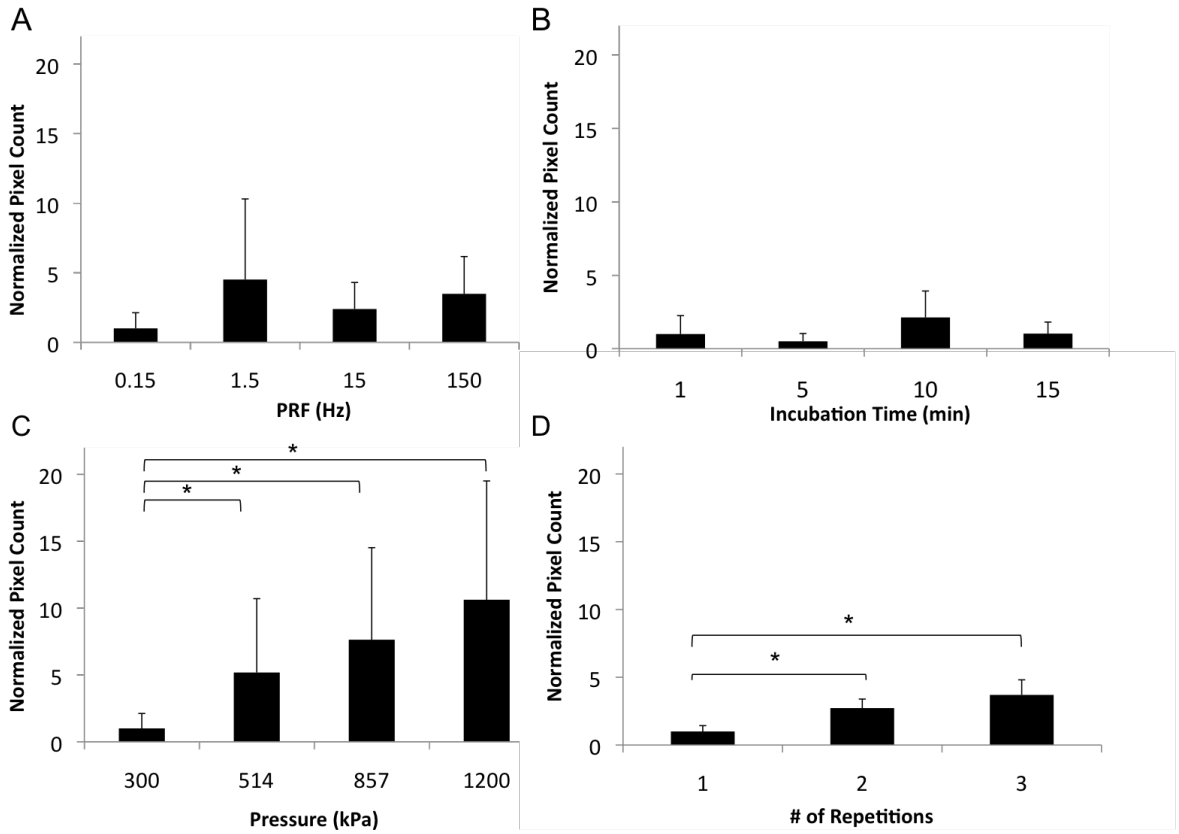

Figure 3.3: Ultrasound parameters tested included PRF, incubation time, pressure, and number of repetitions. Standard settings used were 10 minute incubation time, a PRF of 0.15 Hz, Pressure of 300 kPa, and 3 minutes of ultrasound exposure with a 1 MHz unfocused transducer. Mean and standard deviation for each setting are plotted. (A) Increasing the PRF did not lead to a significant increase in calcein uptake (N=7). (B) Increasing the incubation time did not have a significant impact on calcein uptake (N=9). (C) A linear increase was seen in cellular fluorescence from calcein was pressure was increased (N=9). Each of the higher pressure were significant from the baseline setting, but not from one another. (D) Repeating the incubation and ultrasound procedure multiple times lead to significant increases in calcein uptake compared to one exposure time (N=4). *$p<0.05$

Incubation time was observed to result in greater sonoporation after 10 minutes of incubation than 1 and 5 minutes, but was not statistically significant (Fig. 3.3B). As with PRF, high variability was seen in the data. Incubation time was studied to determine whether longer incubation times would lead to greater uptake through sonoporation as microbubbles float into contact with the cells on the coverslip. Although no statistically significant differences were seen, a longer incubation time of 10 min was used since it has been shown that greater sonoporation effects occur when the microbubble is in close proximity to the cell [133]. In reviewing similar studies, some groups allow flotation time while other group immediately expose the cells to ultrasound after the addition of microbubbles. This is one example of the variations in experimental design that need to be studied more in depth in future work.

Within the range of acoustic parameters tested, calcein internalization by target cells increased with increasing acoustic pressure (Fig. 3.3C). An increasing linear trend in fluorescence was observed. Uptake increased up to tenfold by changing pressure from 300 up to 1200 kPa. A Student's t-test showed a significant increase in calcein uptake from baseline settings when pressure was above 500 kPa ($p<0.05$), but no significant differences were seen between the higher pressure groups. Increasing acoustic pressure is an established method of increasing the effects of sonoporation [73; 125; 134]. These results validate the current setup as similar trends to other groups are seen. These findings correlate with other groups who have seen increased permeability with increased pressure. At higher acoustic pressures cell detachment was seen; similar findings were presented by Karshafian *et al.* in an Opticell setup [73]. Cell detachment and cell death are seen to increase with increasing pressure. Finding a balance between permeability and viability is an important step to achieve optimal delivery and will continue to be studied.

Calcein internalization also increased with repeated exposures of the cells to microbubbles and ultrasound (Fig. 3.3D). After undergoing 10 minutes of incubation with calcein and microbubbles followed by 3 minutes of ultrasound, the cell coated coverslip was transferred to a new well and incubation and insonation was repeated either one or two more times. Uptake was increased almost fourfold by increasing ultrasound and microbubbles exposure from 1 to 3 repetitions. Both 2 and 3 repetitions were statistically significant from only 1 exposure cycle ($p<0.05$), although they were not statistically different from each other. Repeating the ultrasound exposure with calcein and microbubbles two or three times increased cellular uptake compared to a single exposure. Adding fresh microbubbles to the well was performed to simulate flowing microbubbles *in vivo*. During an *in vivo* experiment targeted vasculature would continually be exposed to microbubbles. Although repeated exposures resulted in an increase in cell uptake, it is not as practical a solution for current setup due to the extra handling of the coverslips leading to higher chances of damaging the cells. A modified experimental setup involving a flow chamber, such as one used by Chen *et al.*, would not have the same limitation and may be able to achieve a similar effect while more accurately representing the *in vivo* environment, however acoustic radiation force would need to be applied to push microbubbles next to the cells since the flotation aspect is removed [135].

Due to the large variance in data for the acoustic parameters tested, cell density on the coverslip was studied to determine if it was affecting sonoporation results. Cells were insonated at varying confluency levels to look for a correlation between cell growth and sonoporation. Previous work by Yang *et al.* found that cells in the stage of mitosis were more susceptible to pore formation that other stages of cells growth [79]. However, with the tested acoustic parameters, experiments with cell confluency and uptake revealed no significant difference. A consistent percentage of cells affected by sonoporation was

seen regardless of the area of coverslip coated by cells. At the baseline settings, roughly 15% of cell area showed uptake of calcein regardless of the confluency of the coverslip.

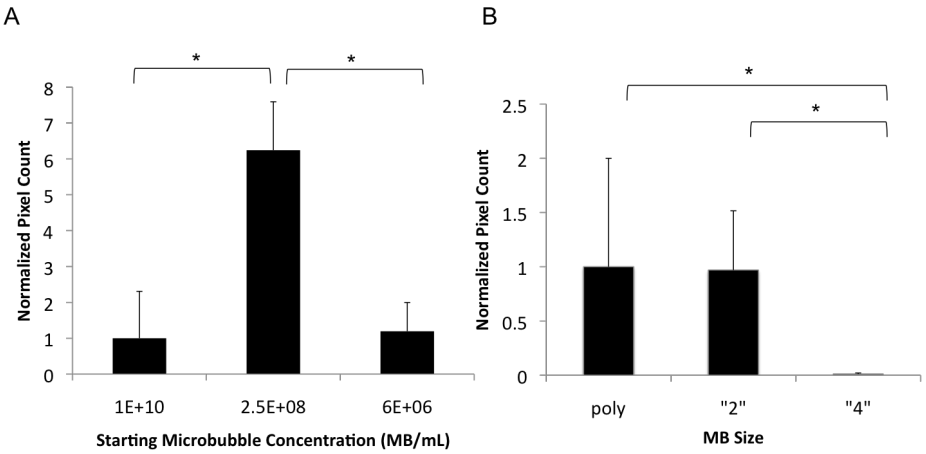

Figure 3.4: (A) Three concentrations of 1 μm microbubbles were tested at the baseline ultrasound settings. Reducing the concentration from the initial stock concentration produced significantly higher amounts of calcein uptake within the cells (N=7). (B) Two larger microbubble populations, 2 μm and 4 μm were tested at the optimal 1 μm concentration. The 4 μm microbubbles did not result in calcein uptake (N=6). Mean and standard deviation of normalized pixel count above baseline are plotted; *p<0.05

Microbubble concentration was also observed to affect sonoporation efficiency. A statistical difference was seen between the middle concentration tested and both the high and low concentrations with 1 μm microbubbles (Fig. 3.4A). It was observed that it was possible to have too many or too few microbubbles present, which lead to a decrease in sonoporation. These findings correlate with permeability results found by Karshafian *et al.* who saw similar curves with both Optison and Definity [126]. Increasing concentration enhanced microbubble-cell interaction to a point, after which microbubble screening reduces the acoustic energy delivered to microbubbles close to cells. Bright field images showed the presence of large microbubbles even after washing when a high concentration was used. It was observed that the microbubbles were not breaking and were coalescing to form larger bubbles when higher concentrations were

used. Large bubble cluster formation was also reported by Meijering *et al.* [65]. Unlike with the ultrasound parameters, current findings on concentration dependence are not in agreement with work published by Rahim *et al.*, who believed concentration was not a critical factor and did not see significant changes when changing the concentration [124]. Studies presented here used a higher concentration of microbubbles and had the transducer placed below the cells, requiring the ultrasound to penetrate through the microbubble layer at the cell surface. Positioning the transducer below the microbubble and cell layer simulates an *in vivo* environment where the radiation force would be used to push the microbubbles out of flow before microbubble destruction. The cell suspension setup used by Karshafian *et al.* also required the ultrasound waves to penetrate through the solution of microbubbles and cells [126]. Effects of microbubble attenuation *in vivo* have been seen in imaging studies, and results presented here suggest attenuation resulting from high concentrations could be critical for therapeutic studies [136]. Other concentration studies see an increase and then plateau [124; 125]. It is hypothesized that this different behavior can be attributed to differences in ultrasound parameters used such as longer pulse length and higher duty cycle, along with transducer placement as mentioned above. Additionally, although the aim is to investigate concentration, it is possible that these studies did not explore a wide enough range in concentrations to observe the same increasing, then decreasing trend. Differences in reporting concentrations used such as volume added or percent volume cannot always be compared due to these differences in stock concentrations. Because stock concentrations of microbubbles vary from $1x10^{10}$ down to $1x10^{8}$, even using undiluted samples are not comparing the same volume.

Microbubbles can be produced in a range of sizes, such as around 1 μm in diameter for Definity (Lantheus Medical Imaging North Billerica, MA, USA), to around 2 μm for SonoVue (Bracco International BV, Amsterdam, Netherlands). Several groups,

including our own, also have developed methods to size isolate larger microbubbles [24; 129]. Since not all microbubble solutions have the same size characteristics it is important to understand the impact of size on ultrasound mediated therapy. A clear dependence on both size and concentration for sonoporation was observed. When 1 and 2 μm microbubbles were tested at the same concentration, similar results were seen. However, with microbubbles closer to 4 μm in diameter, cellular uptake was not observed (Fig. 3.4B). The 4 μm microbubbles were investigated further and a similar distribution in optimal concentrations was seen to the 1 μm microbubbles, only shifted to a lower concentration (Fig. 3.5). Lowering the concentration, however, led to calcein internalization. While other groups have examined the role of microbubble concentration and brand [125; 126; 137] this study takes a more in depth look at size by comparing microbubbles with the same composition and expanding the range of concentrations. Although Alter *et al.* compared Optison, Sonozoid, and SonoVue at various concentrations, the focus was on finding the agent that worked the best, not on studying the effect of size [137]. In addition, they concluded that size had little influence, which is not in agreement to current findings. Here, the larger microbubbles performed poorly compared to smaller bubbles at the same settings. A lower concentration was needed to enhance delivery into the cells. The effect of size has also be documented by Choi *et al.* with blood brain barrier studies, who also found that size does have an impact on delivery [83]. Future exploration on the optimal concentration based on microbubble size with varying frequency is needed to take into account the resonance frequency dependent response of microbubbles.

It has been pointed out here and by other groups that variations exist in *in vitro* setups used to study the effects on ultrasound on cells [138]. Because of the goal to focus on sonoporation effects that would occur after acoustic radiation force, it was important to make sure microbubble flotation was present. Allowing space for the microbubbles

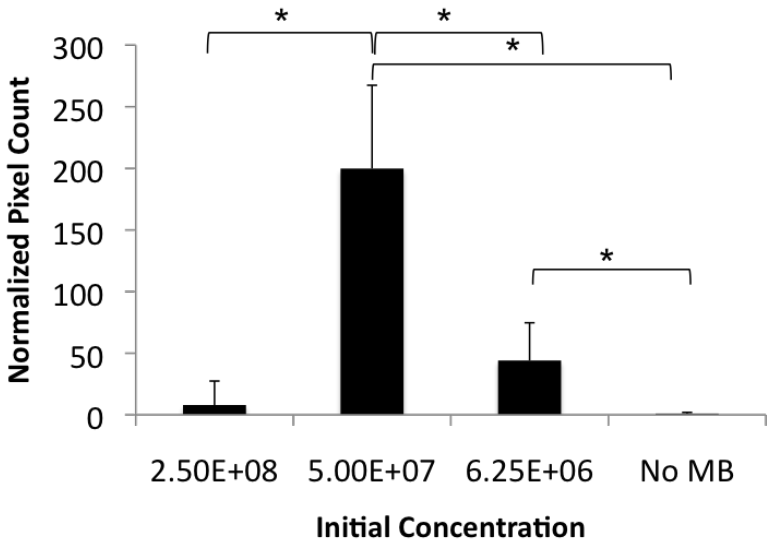

Figure 3.5: (A) 4 μm microbubbles tested at the peak concentration for 1 μm microbubbles did not show the same enhanced sonoporation effect. At a lower concentration, calcein uptake was seen using the 4 μm microbubbles. Mean and standard deviation of normalized pixel count above baseline are plotted (N=6). *p<0.05

to become in contact with the cells allows for the cavitation effects of the microbubble to be studied in depth separate from acoustic radiation force. This would not have been possible using a cell suspension study or with cells cultured on the bottom of well plate. Additionally, precise control over the concentration of microbubbles present at each ultrasound treated site was needed. In an OptiCell, the concentration of microbubbles can decrease over time as microbubbles are destroyed at each exposure site and large amounts of microbubbles solutions must be used at one time. These reasons contributed to the use of a coverslip setup. Modifications were made to improve upon a traditional treatment within a well by using a FlexCell plate which has a soft membrane bottom that leads to less attenuation and reflection than a hard bottomed culture plate, as well as a plastic coverslip instead of glass [139]. However, it could be advantageous to have a chamber that can be fully submerged in a water bath to eliminate the air interface. Future studies will be performed with additional modifications to the setup

that eliminates the air interface by creating a sealed chamber submerged in a water bath. Additional future work will look more in depth at the relationship between size and concentration with respect to ultrasound frequency and pressure.

3.4 Conclusions

Determining optimal ultrasound parameters for sonoporation is beneficial for future studies involving drugs or macromolecules. Challenges for *in vitro* studies include selecting parameters that will increase cell permeability, yet not irreversibly damage or detach cells. The presented findings are in agreement with current literature in that there are substantial changes in sonoporation efficiency depending on acoustic parameters, yet additional evidence was observed that microbubble concentration and size play a larger role than previously believed. These findings will help inform ongoing and future studies as microbubble- mediated ultrasound therapies develop towards clinical use and bring more attention to the importance of experimental design.

CHAPTER 4

Design of Acoustically Active Nanocapsule Delivery Vehicles for Ultrasound-Targeted Chemotherapy

4.1 Introduction

In the previous chapter, the roles of various acoustic and microbubble parameters in enhancing cellular permeability were examined. In this chapter, microbubble destruction and microbubble translation by acoustic radiation force are combined. In addition, the first nanoparticle loaded microbubble used for this research is introduced.

By utilizing an acoustically-active delivery vehicle (AADV), which combines the acoustic activity of a microbubble with the high payload and extravasation ability of nanoparticles, the limitations of current chemotherapy delivery methodologies can be overcome. In this chapter the synthesis and characterization of AADVs and preliminary results of *in vitro* delivery to cells are described.

4.2 Materials and Methods

4.2.1 Materials

DSPC, DSPE-PEG2K, and DSPE-PEG2K-Biotin were purchased from Avanti Polar Lipids (Alabaster, AL). Additionally, 25-[N- [(7- nitro- 2- 1, 3- benzoxadiazol- 4 -yl) methyl]amino]-27- norcholesterol (25-NBD- cholesterol) and 1, 2 - dioleoyl- sn-glycero- 3 -[(N-(5- amino-1-carboxypentyl) iminodiacetic acid)succinyl] (nickel salt) (DGS-NTA(Ni)) in chloroform, were purchased from Avanti Polar Lipids. Inc. Streptavidin protein (His-tag) was purchased from Abcam (Cambridge, MA). Green Fluorescent Protein (His-tag) was purchased from Millipore (Billerica, MA).

4.2.2 Biotinylated Microbubble Preparation

Lipid solutions were formed using a 9:0.5:0.5 molar ratio of DSPC, DSPE-PEG2K, DSPE-PEG2K-Biotin in a 90 mL solution of phosphate-buffered saline (Fisher Scientific, Pittsburg, PA). Size isolated microbubbles were created using the method previously described by Feshitan *et al.* and Streeter *et al.* [129; 24]. Briefly, using a sonic dismembrator (Model 500, Fisher Scientific, Hampton, NH) for 15 seconds at 70% power in the presence of decafluorobutane (SynQuest Labs, Alachua, FL), microbubbles were generated via acoustic emulsification and isolated with centrifugation. Concentrations and size distributions of the microbubbles were obtained using a laser light obscuration and scattering device (Accusizer 780A, Particle Sizing Systems, Santa Barbara, CA).

4.2.3 BTM Nanocapsule Preparation

Nanocapsules were made by warm water microemulsion methods as previously described by Dong *et al.* [140; 141]. Miglyol 812 as the oil phase, Brij 78, Vitamin E TPGS, and DOGS-Ni-NTA as the surfactants were weighed out into a 7 mL glass vial. The vial was heated to 65°C to melt the oil and surfactants while stirring, and

then preheated deionized water was added to form the nanocapsules. The excess of DOGS-Ni-NTA was removed by a Sepharose CL-4B column and the nanocapsules were concentrated by rotary evaporator. The final GFP nanocapsule was formed by adding his-streptavidin and his-GFP into the concentrated nanocapsules.

Paclitaxel containing nanocapsules were made in a similar method. The behenoyl-paclitaxel conjugate was dissolved in ethanol and transferred to the vial containing the oil and surfactant mixture. Residual ethanol was evaporated under a stream of nitrogen gas, and then preheated deionized water was added to form the nanocapsules. The excess of DOGS-Ni- NTA was removed by a Sepharose CL-4B column and the nanocapsules were concentrated by rotary evaporator. The final behenoyl-paclitaxel nanocapsule containing his-streptavidin was formed by adding his-streptavidin into the concentrated nanocapsule suspension.

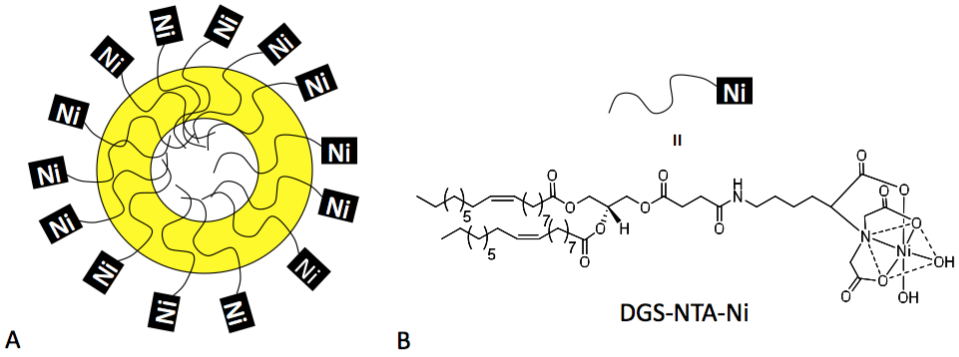

Figure 4.1: (A)DGS-NTA-Ni was incorporated in the shell of BTM nanocapsules. (B)Four out of the six co-ordination sites of Ni are occupied by NTA while the two remaining sites (shown as occupied by water molecules) are available for binding by the his-tagged peptides. Figure provided by Saurabh Wadhwa.

4.2.4 AADV Preparation

Acoustically-active delivery vehicles (AADVs) were created by incubating microbubbles and nanocapsules within a syringe and mixing on a rotating stand. Free nanocapsules were removed by either washing by flotation or centrifugation. Vehicles were examined using fluorescence microscopy or high performance liquid chromatography (HPLC) to assess binding. Control vehicles were made of fluorescent avidin polystyrene beads (Spherotech, Lake Forest, IL) conjugated to biotin microbubbles.

4.2.5 Cell Culture

Rodent mammary adenocarcinoma cells (R3230), maintained in DMEM medium (Sigma, St. Louis, MO) supplemented with 10% fetal bovine serum and 1% penicillin/streptomycin, were grown as a cell monolayer on Thermanox coverslips (Nalge Nunc, Rochester, NY). Thermanox coverslips were used because they are nearly acoustically transparent.

4.2.6 *In Vitro* Delivery

A flow phantom setup was used to determine acoustic parameters required to both concentrate microbubble vehicles and to fragment the microbubble (Fig. 4.2). Both a water-immersion objective and a 2.25 MHz focused transducer (Olympus Panametrics, Waltham, MA) were mutually focused with each other and on a 200 μm tube. Microbubbles were pushed through the tube by a syringe pump. An arbitrary waveform generator allowed pulse sequences of varying frequency and amplitude to excite the transducer. A high speed camera allowed the microbubbles to be visualized while being exposed to ultrasound.

In vitro experiments were performed using a static chamber to test vehicle and parameter settings (Fig. 4.3). The static chamber consisting of a transducer and cell

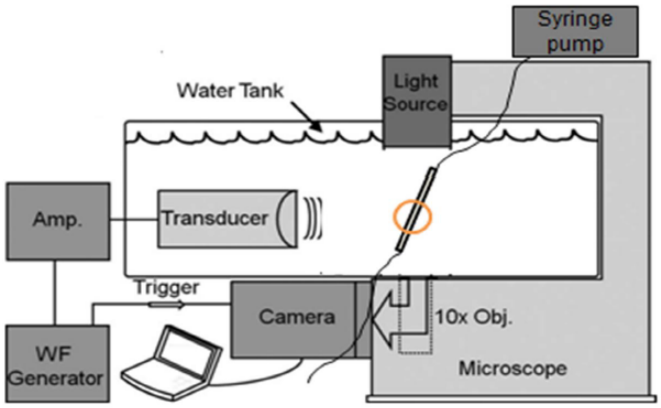

Figure 4.2: A high speed camera and phantom setup with the microscope and transducer mutually focused on a 200 μm tube allowed microbubbles to be visualized while being exposed to ultrasound.

plate in a water bath was used to test the ability of ultrasound to locally increase nanoparticle delivery. Cells cultured on a coverslip were exposed to an AADV solution and positioned in front of a focused 2.25 MHz focused transducer. The cells were exposed to ultrasound for three minutes then washed in PBS before being examined.

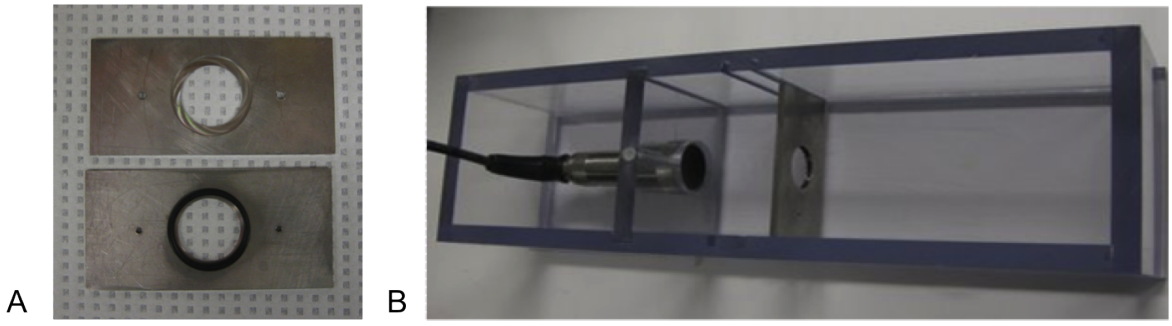

Figure 4.3: A static chamber consisting of a transducer and cell plate in a water bath was used to test the ability of ultrasound to locally increase nanoparticle delivery. Cells cultured on a coverslip were exposed to a AADV solution and positioned in the focus of a 2.25 MHz transducer.

Table 4.1: Composition and physicochemical characteristics of BTM-Ni nanoparticles (Provided by Lei Peng and Saurabh Wadhwa)

Parameters	BTMNi Nanoparticles
Brij 78/Vit E TPGS/M812 /DGS-NTA-Ni (mg/mL)	3.5/1.5/2.5/0.1
Particle size ± S.D.	183.9 ±1.33
Polydispersity Index	0.026
Zeta potential ± S.D.	-14.8 ± 11.3
Nickel content (ng/mg NP)	145.6 ± 19.53
Binding efficiency (Molar) (Ni:GFP)	1:12
GFP: Streptavidin (molar ratio)	1:1

4.2.7 Vehicle Drug Loading

Paclitaxel-loaded AADVs were analyzed to determine the amount of drug bound to the bubbles. Increasing amounts of microbubbles were added to a fixed volume of nanocapsules to obtain a loading curve. After a floatation wash was performed, the bottom PBS layer and top bubble layer were separated for analysis. The behenoyl-paclitaxel conjugate concentration in nanocapsule formulations was measured by HPLC with an Inertsil ODS-3 column. The mobile phase consisted of a solvent mixture of isopropyl alcohol, water and acetonitrile (35:5:60, v/v/v) at a flow rate of 1.0 mL/min. The retention time of behenoyl-paclitaxel was about 9.5 min.

4.3 Results and Discussion

Successful conjugation of GFP/Streptavidin labeled BTM nanocapsules onto the shell of biotinylated microbubbles was verified by fluorescence microscopy (BX51 Microscope, Olympus, Center Valley, Pa) (Fig. 4.4). Modifications of the BTM nanocapsules involving various fluorescent moieties including Cy3, bodipy, and Oregon green paclitaxel were also tested but could not be easily detected under the microscope.

Using a high speed camera, the response of microbubbles within a tube to various ultrasound parameters was studied. Optimized radiation force was achieved with a

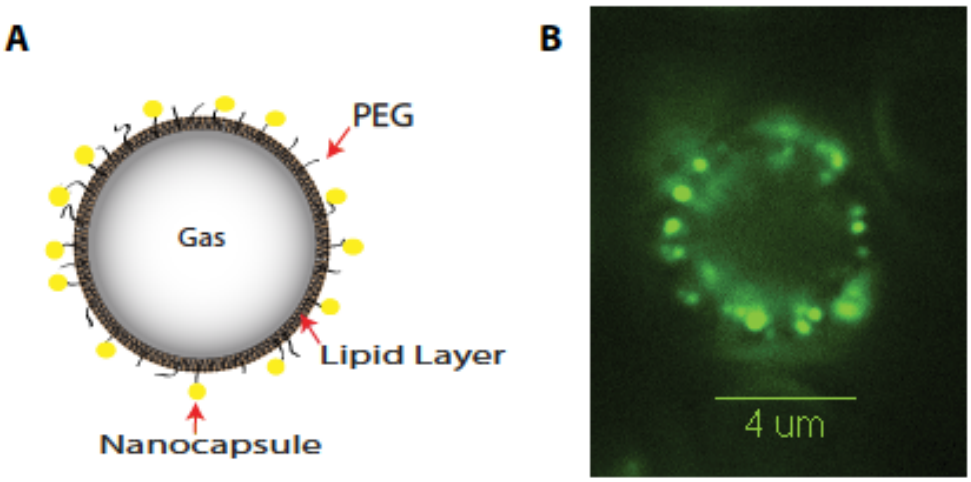

Figure 4.4: (A) A cartoon illustration of proposed loading of nanocapsules onto the shell of the microbubble. (B) Confirmation of loading onto the bubble seen by fluorescence microscopy. ©2010 IEEE.

2.25 MHz focused transducer operated at 3.5 MHz, 50 kPa. Microbubble destruction occurred with a 5 pulse sequence at 1.5 MHz, 1.2 MPa with 0.1 second pause between each pulse. The final wavelength was a 3 second waveform operated at PRF of 150 mHz at a duty cycle of 30%.

In vitro static chamber experiments using the optimized parameters yielded higher delivery of nanoparticles within the focus of the transducer compared to outside of the focus (Fig. 4.5A). Using intensity thresholding in MetaMorph Basic software (Molecular Devices, Downingtown, PA), comparisons were made for the amount of fluorescence present in various areas of the coverslip. The relative integrated intensity shows a 14-fold increase in nanoparticle delivery within the focus of the ultrasound (Fig. 4.5B).

After optical confirmation of nanoparticles binding to the bubbles was seen, a quantitative analysis of the AADV was desired to determine the drug concentration delivered to the cells was performed. HPLC results showed that an average of 50% of the initial paclitaxel mixed with microbubbles was bound to the shell (Fig. 4.6). Nearly 80% of

the paclitaxel was recovered between the top bubble cake and bottom wash layer. It is possible that there was more bound paclitaxel than detected due to loss during the transferring process. Future work will include further drug load characterization of the AADVs followed by *in vitro* drug cell uptake studies.

4.4 Conclusions

Binding of nanocapsules to ultrasound microbubble contrast agents was achieved and the ability to increase delivery of nanocapsules using acoustic radiation force and microbubble destruction by ultrasound was demonstrated. Fourteen times as many particles were delivered to cells treated with ultrasound compared to untreated. Future work will include studies with paclitaxel-loaded nanocapsules used both *in vitro* and *in vivo*.

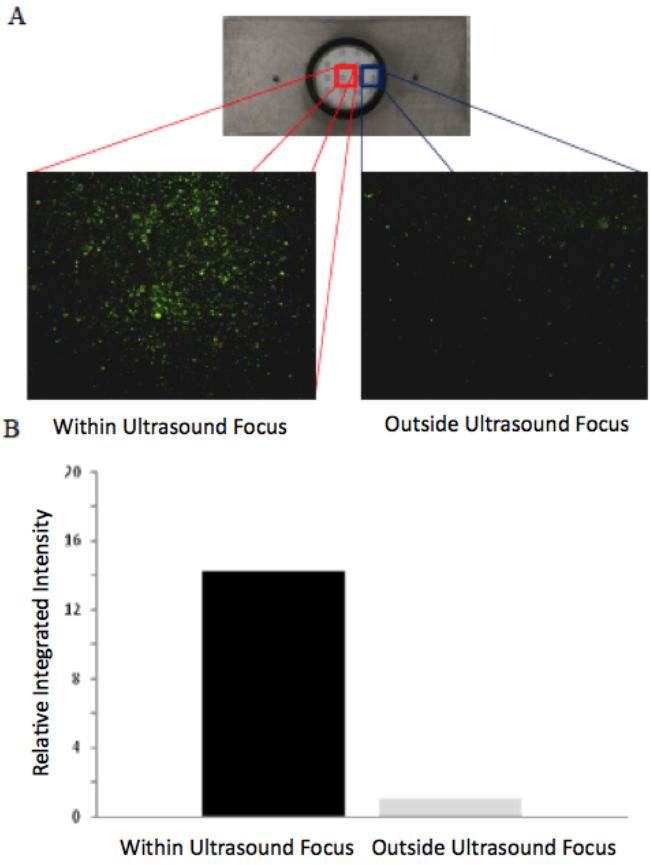

Figure 4.5: A) Increased delivery of nanoparticles to cells was seen with exposure to ultrasound. Images obtained with fluorescence microscopy show higher levels of fluorescence associated with cells in the center of the disc (within the ultrasound focus) compared to outside of the ultrasound focus. B) The relative integrated intensity shows a 14 fold increase in nanoparticle delivery within the focus of the ultrasound.

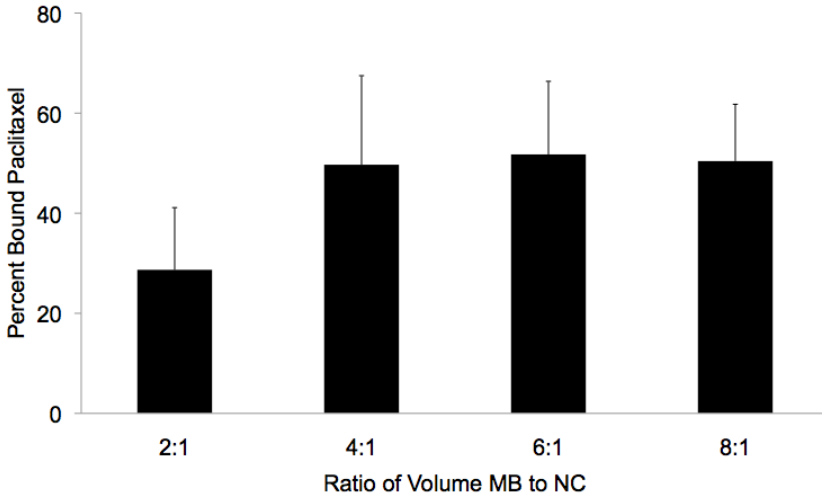

Figure 4.6: HPLC analysis of microbubble solutions containing paclitaxel nanocapsules showed 50% binding of nanocapsules could be achieved. Mean values and standard deviation are plotted; N=3. ©2010 IEEE.

CHAPTER 5

4T1 Tumor Treatment with Paclitaxel Nanocapsules and Microbubble Enhanced Ultrasound Delivery

5.1 Introduction

Nanoparticle based drug delivery is a rapidly growing field, especially in chemotherapy applications. Nanoparticulate formulations offer a promising alternative to conventional methods due to their size and high payload [142; 143; 47]. One reason for the success of this technique is the enhanced permeability and retention (EPR) effect. Nanoparticles can enter into the tumor through the leaky vasculature, thus delivering higher doses of drugs to tumor tissue with lower systemic toxicity. BTM paclitaxel nanocapsules (introduced in the previous chapter) are formed by oil and water microemulsion methods and overcome the limitations of poor drug solubility. This formulation has previously been shown to be more effective at treating tumors in mice than intravenous injections of Taxol [140; 141]. However, accumulation within the tumor was still limited.

It is hypothesized that the addition of low intensity ultrasound and microbubbles to a nanoparticle chemotherapeutic treatment will improve the overall efficacy of the

treatment. Applying ultrasound at the tumor site may enhance nanoparticle drug uptake by increasing vascular permeability through ultrasound targeted microbubble destruction.

5.2 Materials and Methods

5.2.1 Materials

DSPC and DSPE-PEG2K were purchased from Avanti Polar Lipids (Alabaster, AL). Paclitaxel was obtained from ScinoPharm Taiwan Ltd. Polyoxyl 20-stearyl ether (Brij 78) was obtained from Uniqema (Wilmington, DE). Vitamin E TPGS was generously provided by Eastman Chemical Co. (Kingsport, TN). Behenoyl chloride was purchased from Sigma-Aldrich (St. Luis, MO).

5.2.2 Microbubble Preparation

A lipid mixture (DSPC and DSPE- PEG2K) was prepared using a 9:1 molar ratio, similar to a previously described method [128]. Briefly, lipids were dissolved in chloroform, dried and dissolved into a buffer solution of PBS. The lipid solution was then transferred into vials, which were then evacuated and filled with decafluorobutane gas. Vials were shaken with a Vialmix shaker (Bristol-Myers Squibb Medical Imaging, North Billerica, MA, USA) for 45 s prior to injection.

5.2.3 Nanocapsule Preparation

2'-behenoyl-paclitaxel (C22-PX) conjugate was synthesized using behenoyl chloride and paclitaxel (PX) via a one-step esterification reaction. The synthesized conjugate was confirmed and characterized by nuclear magnetic resonance, mass spectrometry, and thin layer chromatography analysis. To prepare the C22-PX nanocapsules, briefly, 2.6 mg of Miglyol 812 as the oil phase, 2.0 mg of Brij 78, and 1.6 mg of Vitamin E

TPGS as the surfactants were accurately weighed out into a 7 mL glass vial. The vial was heated to 65°C to melt the oil and surfactants while stirring. The C22-PX in ethanol stock solution was transferred to the vial containing the oil and surfactant mixture. Residual ethanol was evaporated under a stream of nitrogen gas, and then preheated deionized water was added to obtain a final volume of 1 mL. Oil-in-water microemulsions formed spontaneously at this elevated temperature and upon direct cooling of the warm microemulsions to room temperature, nanocapsules formulations were formed. To enhance circulation time, the Brij78PEG750 was synthesized and incorporated on the surface of the nanocapsules.

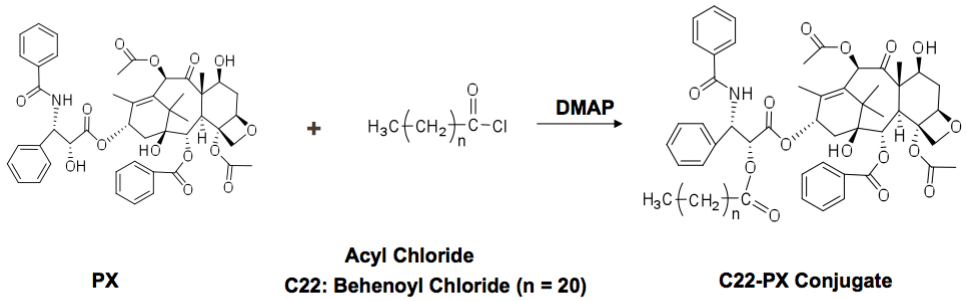

Figure 5.1: Chemical Structure of the paclitaxel conjugate used. Figure provided by Ping Ma.

5.2.4 Animal Preparation

Animals were handled according to National Institute of Health guidelines and our study protocol was approved by the UNC Institutional Animal Care and Use Committee. Twenty four female BALB/c mice received a subcutaneous injection of $1x10^8$ 4T1 mammary carcinoma cells on the left flank. Treatment began once tumor volumes reached approximately 100 mm^3, about 1 week after injection.

5.2.5 Treatment

Mice were divided into three treatment groups. Group one received a 200 μL tail vein injection of C22-PX nanocapsules (NC). Group two received a 200 μL tail vein injection of C22- PX nanocapsules followed by ultrasound exposure (NC+US). Group three received a co-administration of 150 μL of C22- PX nanocapsules with 50 μL MB followed by ultrasound exposure (NC+MB+US). The paclitaxel dose for all animals was 2.5 mg/kg. After receiving the appropriate tail vein injection, animals were placed on a heating pad and anesthetized with inhaled isoflurane at 1.5% through a nose cone. Ultrasound gel was then applied between the tumor and the transducer. Therapeutic ultrasound was applied with a Sonicator 740 system (Mettler Electronics Corp.). The 1 MHz transducer was operated at 2 W/cm^2 and 10% duty cycle (Fig. 5.2). Tumors were sonicated for two minutes. Treatments were given every other day for two weeks.

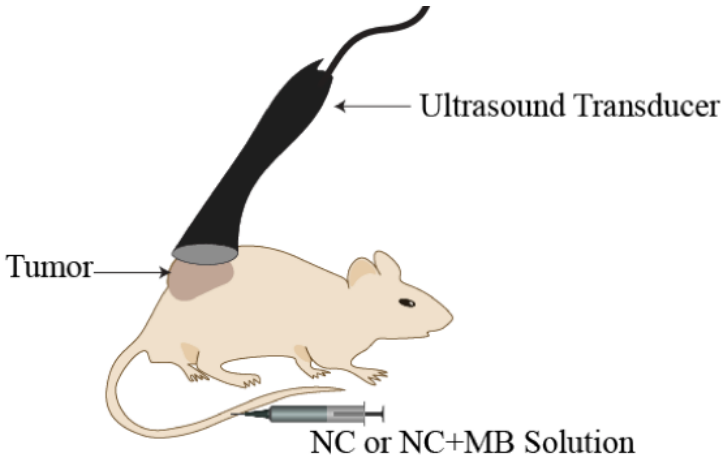

Figure 5.2: Therapeutic ultrasound was applied with a Sonicator 740 system (Mettler Electronics Corp.). The 1 MHz transducer was operated at 2 W/cm^2 and 10% duty cycle. Tumors were sonicated for two minutes. Treatments were given every other day for two weeks.

5.2.6 Analysis

Caliper measurements were taken every other day to measure the volume of the tumor. The tumor size was calculated as 1/2 x (width)^2 x (length). Animal weight was also monitored.

After humanely sacrificing the mice, the tumors were removed and processed routinely for histology. Specifically, tissues were processed into paraffin and 5 μm sections were stained with hematoxylin and eosin using standard methods. The histology slides were scanned with an Olympus BX51 microscope and motorized 2-dimensional stage controlled by MetaMorph software (Molecular Devices, Sunnyvale, CA). The digital images were imported into ImageJ (NIH, Bethesda, MD). A color deconvolution algorithm was performed on each digital histological image to separate the hematoxylin and eosin [13]. An index was calculated by dividing the number of pixels that corresponded to hematoxylin by the sum of the pixels that corresponded to hematoxylin and eosin.

5.3 Results and Discussion

Although tumor growth was not halted by any of the treatments, mice treated with the combination of paclitaxel nanocapsules, microbubbles and ultrasound had slower tumor growth compared to nanocapsules alone and nanocapsules with the addition of ultrasound (Fig. 5.3). On days two, four, six, eight and twelve, there were significant differences between average tumor volume between tumors treated nanocapsules and ultrasound compared to nanocapsules, ultrasound and microbubbles ($p<0.05$). On days six and ten, significant differences were seen between average tumor volume of mice treated with nanocapsules only compared to nanocapsules, ultrasound and microbubbles ($p<0.05$). At the end of the two week treatment schedule, average volume between all groups were not statistically different.

Previous work evaluated the efficacy of C22- PX nanocapsules at a dose equivalent

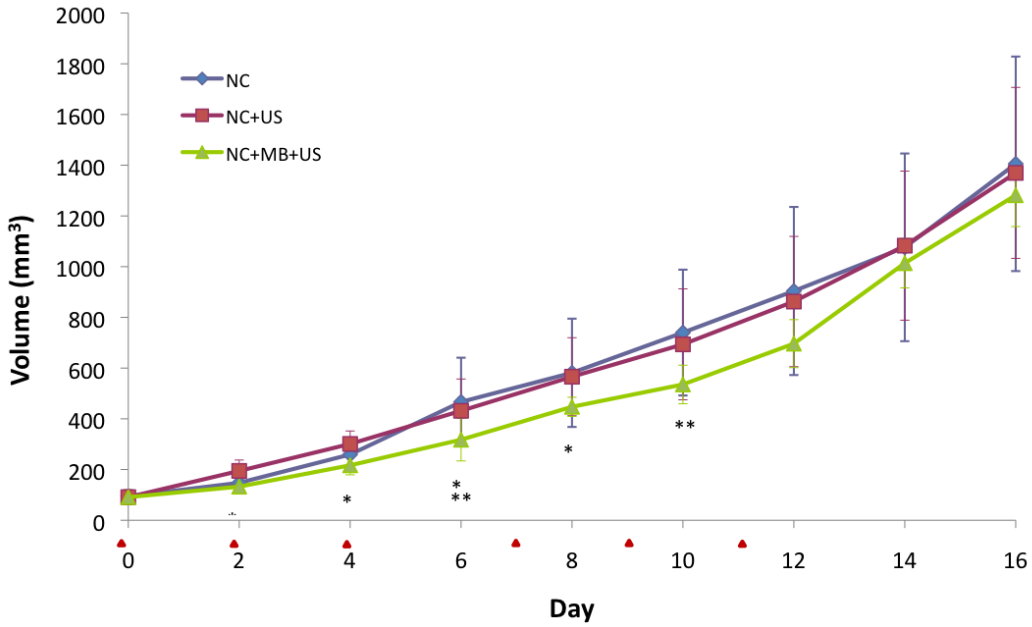

Figure 5.3: Mice bearing 4T1 tumors were treated with either NC (N=8), NC and US (N=8), or NC, MB, and US (N=6). Mice treated with nanocapsules, microbubbles and ultrasound had the slowest tumor growth rates. Treatments days are marked by red arrows; The treatment dose was 2.5 mg/kg of C22-PX nanocapsules. *Significant difference ($p<0.05$) between NC+US and NC+MB+US **Significant difference ($p<0.05$) between NC and NC+MB+US. © 2011 IEEE

to 5 mg/kg paclitaxel [144]. The results from this study were used to make a comparison to our current study were the dose was lowered to 2.5 mg/kg. It was hypothesized that the addition of ultrasound and microbubble will allow for a lower treatment dose to be given. Because the tumors implants and treatments were done at separate times, the tumor volume data was normalized to the starting volume. This lead to the finding that the growth curve of tumors treated at the lower dose of 2.5 mg/kg with ultrasound and microbubbles was similar to the growth curve produced at double the dose (Fig. 5.4). Hematoxylin and eosin staining of tumor tissue was performed to characterize any differences in tissue based on treatment groups. Tumor samples all revealed necrotic centers of the tumor, and no significant differences in areas of necrotic tissue between

treatment groups (Fig. 5.5). Tumors were also harvested from animals that did not receive any treatment.

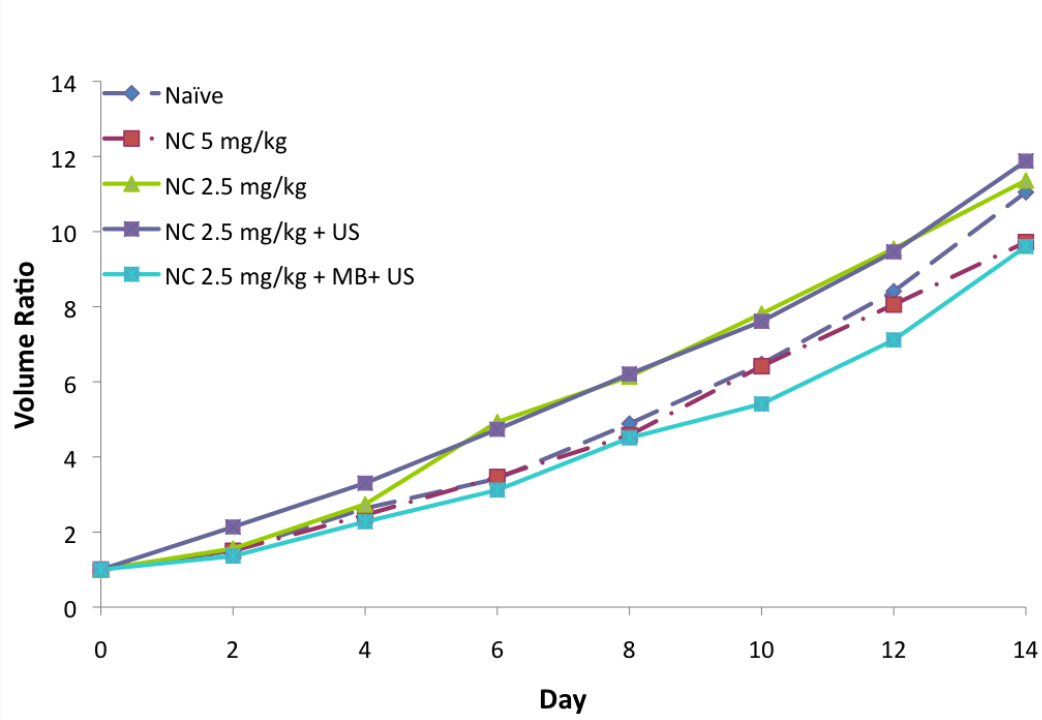

Figure 5.4: Mice bearing 4T1 tumors were treated with either NC, NC and US, or NC, MB, and US treated at 2.5 mg/kg were compared with data from unpublished work by Ping Ma. Data was normalized to tumor starting volume. Mice treated with nanocapsules, microbubbles and ultrasound had the slowest tumor growth rates. Treatments days are marked by red arrows. *Significant difference ($p<0.05$) between NC+US and NC+MB+US **Significant difference ($p<0.05$) between NC and NC+MB+US. © 2011 IEEE

Data indicated significant differences in tumor growth over treatment days, despite the fact that the tumor used was an aggressive, quickly growing tumor. The study design may be improved upon by using a higher treatment dose or by changing the treatment schedule. Treating every other day with tail vein injections is difficult, and the number of animals in the third treatment group decreased from eight to six because it was not possible to do injections in two of the mice after a week of treatment.

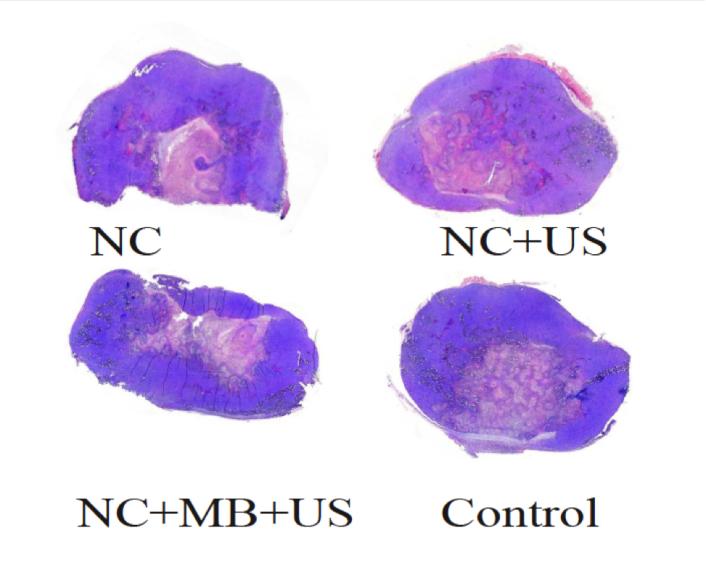

Figure 5.5: Mice were sacrificed after 14 days and tumors were harvested, sectioned and stained using hematoxylin and eosin. Examples of tumor sections showing necrosis in all treatment groups are shown.

5.4 Conclusions

Preliminary results showed the potential to reduce growth of an aggressive tumor model using paclitaxel nanocapsules combined with microbubbles and ultrasound. The combination of paclitaxel nanocapsules with microbubbles and ultrasound performed equally as well as nanocapsules alone at twice the dose. It is hypothesized that further optimization of ultrasound parameters and delivery vehicles may result in even greater improvements in therapeutic effect. Future work will be done with nanocapsules linked to the microbubble instead of a co-injection in an effort to deliver more drug to the tumor.

CHAPTER 6

In Vivo Targeted Nanoparticle Delivery to Tumors with Acoustic Radiation Force

6.1 Introduction

In this chapter, a fluorescent AADV is used to investigate the ability of a clinical ultrasound scanner to enhance *in vivo* delivery of nanoparticles to tumors. As explained in previous chapters, attaching nanoparticles onto the lipid shell of a microbubble allows for both acoustic radiation force (ARF) and microbubble destruction to be used to increase nanoparticle delivery. In chapter 4, enhanced delivery of fluorescent nanoparticles to a cell layer was observed. Other groups have also demonstrated improved delivery either to cells or tumor tissues by using a nanoparticle loaded microbubble [145; 121; 113; 61; 95; 54]. An additional benefit of attaching the nanoparticle to the shell is that the AADV becomes a theranostic agent since the microbubble can be detected using ultrasound imaging techniques while the nanoparticle component delivers the drug payload. Localized delivery can be monitored using ultrasound to confirm the nanoparticle is reaching the tumor site.

While *in vivo* delivery using bound nanoparticles has been shown by other groups, low frequency piston transducers and focused transducers that do no allow imaging of the tissue have been used [121; 145]. In this work, using methods developed by Gessner *et al.* for molecular imaging, a clinical ultrasound system is used to produce both ARF and microbubble destruction for delivery [146]. Fluorescent nanoparticles and

molecules are used in place of drugs while parameters are optimized. It is hypothesized that enhanced targeted delivery to the tumor will be seen when ARF is applied to the tumor.

6.2 Materials and Methods

6.2.1 Materials

DSPC, DSPE-PEG2K, and DSPE-PEG2K Biotin were purchased from Avanti Polar Lipids Inc. (Alabaster, AL). cRGD peptide (Cyclo-Arg-Ala-Asp-D-Tyr-Cys) and cRGD Biotin-PEG-PEG and were purchased from Peptides International (Louisville, KY). 1,1'-Dioctadecyl-3,3,3',3'-Tetramethylindotricarbocyanine Iodide (DiR) was purchased from Marker Gene Technologies (Eugene, OR). Blue fluorescent streptavidin coated nanoparticles were purchased from Spherotech (Lake Forest, IL).

6.2.2 Biotinylated Microbubble Preparation

Lipid solutions were formed using a 9:0.5:0.5 molar ratio of DSPC, DSPE-PEG2K, DSPE-PEG2K-Biotin in a 90 mL solution of phosphate-buffered saline (Fisher Scientific, Pittsburg, PA). Size isolated microbubbles were created using the method previously described by Feshitan *et al.* and Streeter *et al.* [129; 24]. Briefly, microbubbles were formed using a sonic dismembrator (Model 500, Fisher Scientific, Hampton, NH) operated at 70% power for 15 s in the presence of decafluorobutane gas (SynQuest Labs, Alachua, FL). The microbubble solution that was then centrifuged to isolate desired populations of microbubbles. Concentrations and size distributions of the microbubbles were obtained using a laser light obscuration and scattering device (Accusizer 780A, Particle Sizing Systems, Santa Barbara, CA).

6.2.3 Targeted Nanoparticle and Microbubble Preparation

Targeted nanoparticles were formulated by mixing cRGD biotin PEG with fluorescent streptavidin coated nanoparticles for 30 minutes on a rotating plate. Coated nanoparticles were then incubated with biotinylated microbubbles and mixed for an additional 30 minutes in a 3 mL syringe. The syringe was placed in a 6°C refrigerator overnight in an upright position to allow a layer of AADVs to form at the top of the solution; unbound nanoparticles remained in the infranant. The top layer was resuspended in 1 mL PBS. Concentration and size distributions were obtained with an Accusizer 780A prior to *in vivo* use.

6.2.4 Targeted Fluorescent Microbubble Preparation

Targeted fluorescently labeled microbubbles were formed similarly to the above biotinylated microbubbles. A 9:0.5:0.5 molar ratio of DSPC, DSPE-PEG2K and DSPE-PEG2K cross-linked to a cRGD peptide was combined in a 90 mL solution of phosphate-buffered saline. The 1.5 mL lipid solution was aliquoted into a 3 mL vial with 2 μL DiR and gas exchanged. Microbubbles were shaken using a VialMix and then transferred into a 5 mL syringe. The solution was washed by centrifuged three times for 3 min at 1500xG. The final solution was resuspended in 1 mL PBS. Concentration and size distributions were obtained using an Accusizer 780A prior to *in vivo* use.

6.2.5 Animal Preparation

All animal studies were conducted in accordance with protocols approved by the University of North Carolina School of Medicine's Institutional Animal Care and Use Committee. Both rats and mice were used as part of these investigations. Fischer 344 rats (Charles River Laboratories, Durham, NC, USA) were implanted with fibrosarcoma (FSA) tumor tissue in the right flank. Once tumors reached approximately 1 cm in

diameter they were used for the study. Balb/c mice were injected with 1x10^6 4T1 mouse mammary carcinoma cells. Once tumors reached approximately 0.5 cm in diameter they were used for this study.

6.2.6 Ultrasound Procedure

A Siemens Accuson Sequoia 512 system (Mountain View, CA, USA) and a 15L8 transducer at 7 MHz were used for this study to image the tumor and deliver the AADVs with ARF and microbubble destruction. The transducer was positioned using a three-axis translational motion stage setup (Fig. 6.1). The transducer was swept in the elevational direction across the tumor by a computer-controlled motion stage (Model UTS150PP; Newport, Irvine, CA, USA) interfaced through LabView (National Instruments, Austin, TX, USA) on a desktop computer. ARF pulses were generated in pulsed wave (PW) Doppler mode at a frequency of 7 MHz. Adjusting the gate size (18 mm), location of the gate within the field (65 mm), and blood velocity scale (1 m/sec) created a 25% duty cycle pulse with a PRF of 25 kHz (approximately 70 cycles). Microbubble destruction was achieved in D-color mode with a scan velocity of 5 m/s. ARF pressure was determined in previous work to be 13 kPa [146].

Animals were anesthetized in an induction box at 5% inhaled isoflurane anesthesia mixed with oxygen, and maintained at 2.5%. Animals were then placed on a heating pad to maintain body temperature at 37°C and prepped for imaging. The area to be imaged was shaved, further depilated using a chemical hair remover, and then coupled to the ultrasound transducer using gel. A tail vein catheter was inserted for microbubble administration. A B-mode scan of the tumor volume was performed to determine proper scan length. Approximately 2x10^8 microbubbles were injected through a tail vein catheter, followed by 100 μL saline flush. One minute after injection, ARF was applied to the tumor as the transducer scanned across at a constant speed of 1

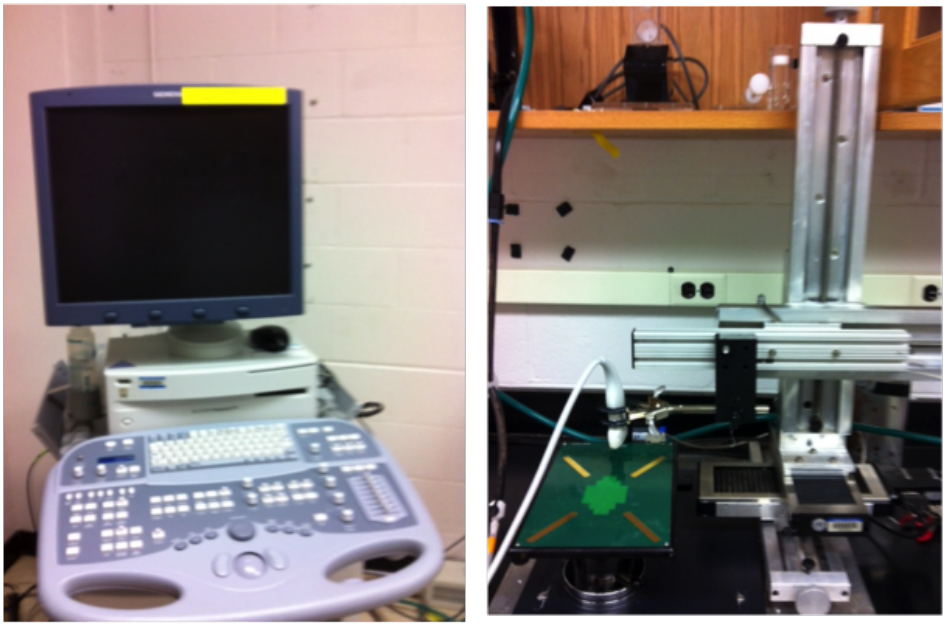

Figure 6.1: A Siemens Accuson Sequoia 512 system was used to image, apply radiation force, and destroy loaded microbubbles. A motion stage (right) was used to scan the transducer across the tumor volume.

mm/s. 5 ARF scans were performed.

After waiting approximately 10 min for freely-circulating bubbles to clear from the animal's system, a 3-D imaging scan of the tumor was acquired in Cadence Pulse Sequence (CPS) contrast imaging mode; the interplane step size was 400 mm. The bound microbubbles were then destroyed using a high mechanical index B-mode 3-D scan. The tumor was imaged again in CPS mode at the same slice locations for a baseline measurement without contrast agents present.

Animals were divided into 3 groups. Group 1 animals served as control without ultrasound or AADV injection. Group 2 received an injection of AADVs followed by microbubble destruction 10-12 minutes after injection. Group 3 received AADV

administration immediately followed by radiation force; microbubble destruction was performed 10-12 minutes after injection. Subsequent studies without destruction were performed to evaluate passive and enhanced targeting of the AADVs. Animals were sacrificed 15 minutes after injection and the tumor tissue was harvested for further analysis.

6.2.7 Optical Imaging

Harvested tumor tissue was placed in a 6 well plate, and imaged with an IVIS Kinetic optical imaging system (PerkinElmer; Waltham, MA).

6.3 Results and Discussion

6.3.1 Nanoparticle Loaded Microbubbles

Loading of the nanoparticles onto the microbubbles was confirmed by optical imaging of the resuspended AADV solution. A fluorescent signal was detected from the microbubbles, however, no signal was seen from the infranant (Fig 6.2). This indicates that the nanoparticles were successfully bound to the microbubbles and could be isolated from the solution. The AADV solution was then diluted to ensure less concentrated solutions would also provide signal.

Further optical imaging tests were performed to examine if the signal from the fluorescent nanoparticles could be detected through tissue. The AADV solution was placed under harvested tumor tissue and imaged. The particles could be detected through the tissue (Fig. 6.3).

6.3.2 Radiation Force Targeting

Results from optical imaging revealed no difference in fluorescent signal from tissues with or without radiation force treatment (Fig. 6.4). These results indicated that

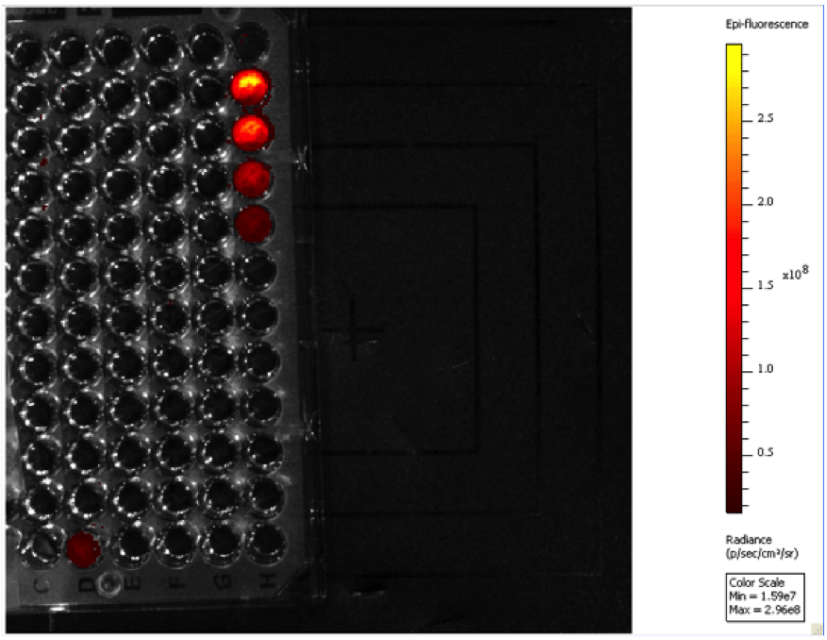

Figure 6.2: After washing, optical imaging of the AADV solution confirmed binding. Imaging parameters were Ex. 640 nm, Em. 680 nm, EM Gain 50, 2 s exposure. The top well, which contained the unused washing solution, did not provide a signal.

the concentration of fluorescent particles delivered to the tumor was too low to be detected or the nanoparticles were not remaining targeted to the tissue after microbubble destruction.

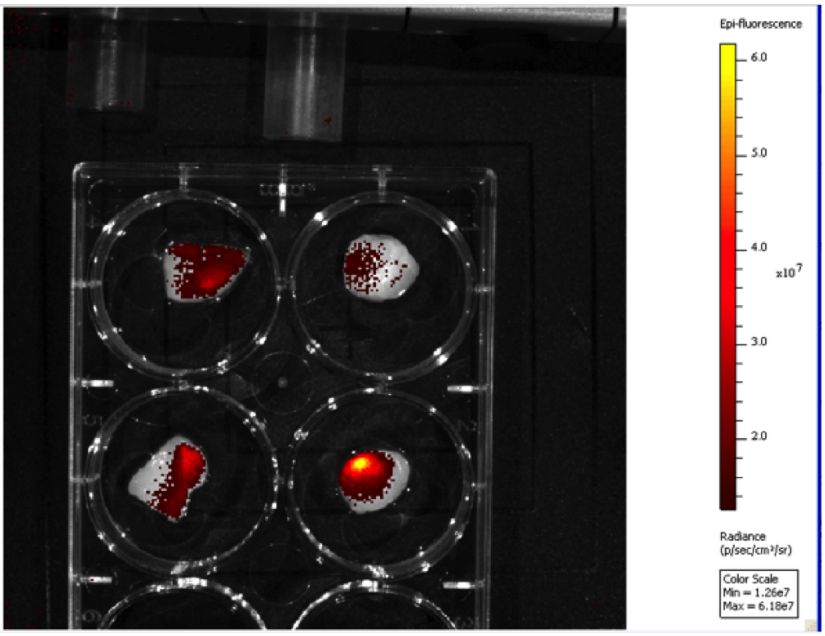

Figure 6.3: The AADV solution was placed beneath harvested control tumor tissue to test signal penetration through tissue. Settings: Ex. 640 nm, Em. 680 nm, 1 s exposure.

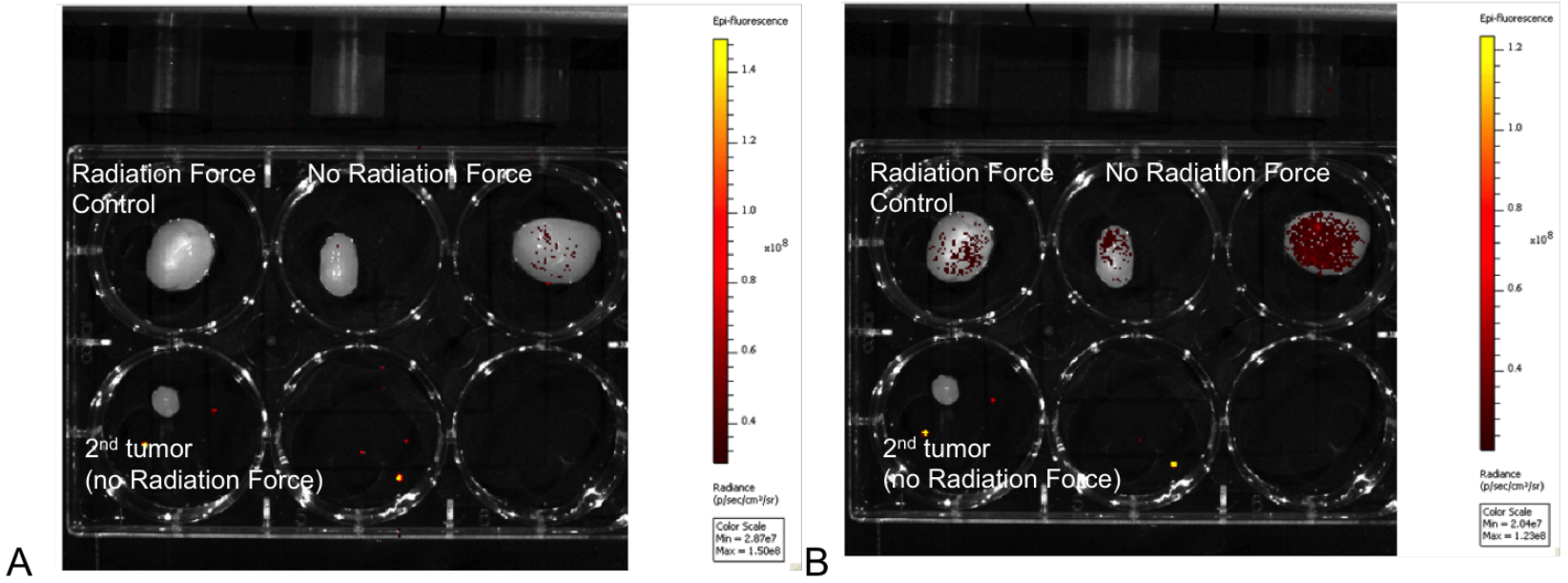

Figure 6.4: Optical imaging of harvested tumors did not show evidence of nanoparticle delivery. Increasing the gain settings (B) did not amplify nanoparticle signal; the control tissue without NP exposure had the highest signal. Imaging settings were A: Ex. 640, Em. 680, 1 s exposure; and B: Ex. 640 nm, Em. 680 nm, 1 s exposure EM Gain 50.

To investigate the signal strength of the AADV solution, a biodistribution study with whole body imaging was performed in a non-tumor bearing female FVB mouse (Fig. 6.5). The fluorescent signal from the AADV solution was not brighter than the background signal from the mouse.

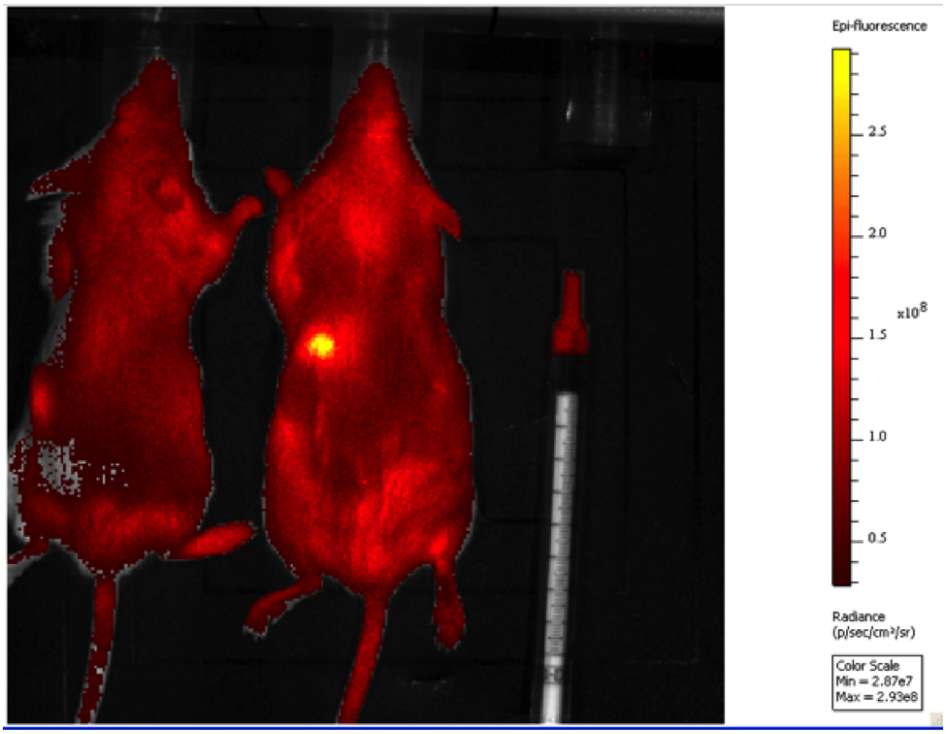

Figure 6.5: To investigate the *in vivo* signal strength of the AADV solution, whole body imaging after a tail vein injection. Left: FVB mouse after injection; center: control FVB mouse without AADV injection; right: AADV solution in syringe. Imaging settings were Ex 640 nm, Em. 680 nm; 1 s exposure.

To further study the effects of the radiation force to enhance delivery *in vivo*, a fluorescent (DiR) microbubble was used for subsequent studies in place of the nanoparticle loaded microbubble. A pilot study (N=1 per group) performed in Balb/c mice with 4TI tumors revealed increased signal from tumor tissue after radiation force was applied compared to passive targeting (Fig. 6.6).

Subsequent studies, however, did not show increased fluorescent signal. It was hypothesized that the microbubbles were not targeting. To explore this hypothesis,

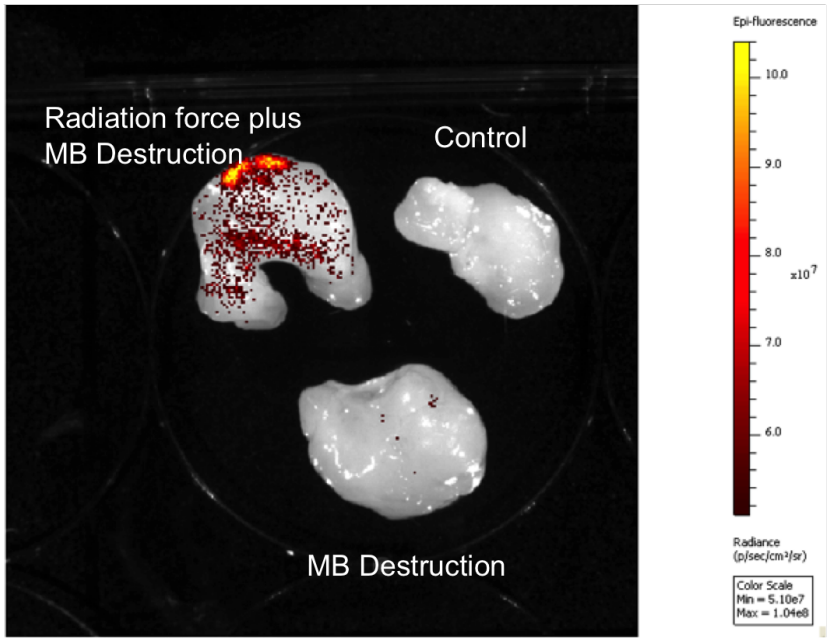

Figure 6.6: Optical imaging of harvested tumors after DiR MB were injected into a Balb/c mouse. Top left: radiation force was applied followed by microbubble destruction. Imaging settings were Ex. 745 nm Em. 800 nm, 1 s exposure, EM Gain 50.

DiR labeled cRGD microbubbles were injected into two rats with FSA tumors. Tumor and liver tissue was harvested after DiR injection with ARF and DiR injection without ARF. The strong fluorescent signal from the liver, but not tumor illustrates that the DiR microbubbles are detectable *in vivo*, but were not successfully targeting to the tumor.

There are several possible explanations for the limited success seen with ARF enhanced delivery of nanoparticles to the tumor tissue. While this method of using a clinical ultrasound scanner to deliver ARF to enhance targeted microbubble delivery has been successful for molecular imaging applications, it could be better optimized for nanoparticle delivery. Due to the wait time between the ARF and the microbubble destruction scans, the AADVs and DiR microbubbles were both designed to be targeted to the endothelium. Unlike in Chapter 4, the break pulse did not come immediately after the push force and the microbubbles would be carried away by the blood flow

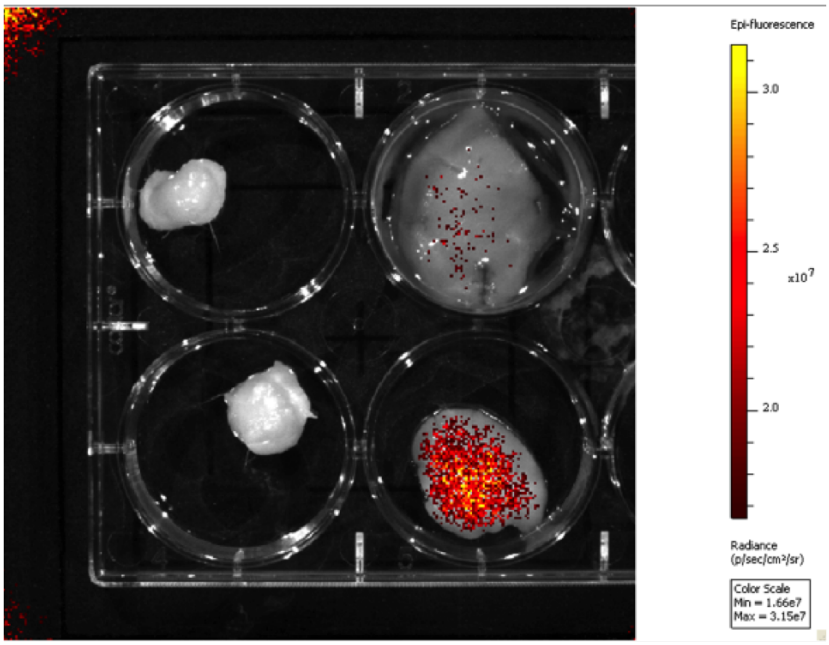

Figure 6.7: After administration of DiR microbubbles and ARF (top row) or without ARF, tumor and liver tissue were harvested. Settings: Ex.745 nm, Em. 800 nm, EM Gain 50, 1 s exposure.

without a targeting component to tether the microbubbles in place. However, targeting could be compromised by the stage of tumor development. Expression levels of $\alpha_v\beta_3$ and vascular density can change as the tumor grows which could inhibit the effectiveness of using cyclic RGD labeled nanoparticles and microbubbles. These studies were also limited by low numbers of animals in each treatment group. Additionally multiple tumor models were used, making comparisons of delivery methods difficult.

Other researchers have shown enhanced delivery into tumors with significant differences in efficacy using drug loaded nanoparticles. Increased delivery seen by others was a result of destroying the microbubbles immediately after injection [115; 145; 147]. However, in the method utilized with the application of ARF, if the AADVs were not targeting, the break pulses would not be effective. Future work will examine various waiting periods to find the optimal timing for ultrasound with and without the addition of ARF.

Early experiments were also limited by the inability to detect the nanoparticles. Attempts were made to extract the particles from digested tumor tissue by centrifugation, but it was not possible due to the small size of the particles. Analysis of the particles and loaded MB by flow cytometry were also hindered by nanoparticle aggregation. Blue nanoparticles (Ex. 640 nm, Em. 680 nm) were selected so that the signal could be differentiated from the tissue. However, these particles could not be loaded onto MB in high enough concentrations to be seen *in vivo* (Fig. 6.5). Alternative methods include real time *in vivo* analysis using an insertable optical imaging device. Sectioning the tumor tissue after nanoparticle administration and ultrasound exposure is also an alternative method that could be explored. Several groups have been able to detect nanoparticles outside of tumor vasculature though tissue histology [115; 145]. Replacing the fluorescent particle with a drug could also help overcome the limitations of detection using optical imaging.

Work published by Burke *et al.* has shown that nanoparticles can be delivered both to the endothelial cells of the tumor vasculature as well into the extracellular matrix of the tumor [145]. Enhancing cytotoxic drug delivery to endothelial cells may still provide a way to halt tumor growth. It has been shown that damaging the endothelial cells within tumor makes tumors more susceptible to chemotherapeutic drugs [148]. The treatment given by Burke *et al.* was over an hour of ultrasound exposure. Shorter treatment times would be more practical both for continuing with preclinical studies and for moving forwards clinical testing.

Future work will continue to optimize settings using a system capable of imaging the tumor while treating. The ability to image using ultrasound and microbubbles contrast agents allows for confirmation that the tumor is vascularized. This is an important characteristic to determine since the delivery can only be achieved if the agents can circulate through the targeted area [149].

6.4 Conclusions

Variations of an AADV using targeted fluorescent nanoparticles were used in combination with a clinical ultrasound system to target the nanoparticles to tumor tissue. Enhancement of fluorescent lipid within the tumor was seen using a DiR microbubble and acoustic radiation force, however a limited number of animals was used. Future work will use other methods to evaluate delivery to avoid problems with weak signal from fluorescent nanoparticles.

CHAPTER 7

Pharmacokinetic Analysis of Ultrasound Mediated PEGylated Liposomal Doxorubicin Delivery to Tumors

7.1 Introduction

While several studies have shown ultrasound enhanced delivery of nanoparticles (see Appendix A), there is limited work that investigates these effects from a pharmacological perspective. How a drug is distributed through the body and its mechanism of action are core components to drug delivery. These parameters are evaluated through pharmacokinetic (PK) and pharmacodynamic (PD) studies. PK examines the time course of the drug concentration in the body, or what the body does to the drug. Drug absorption, distribution, metabolism, and excretion are the primary areas that are studied. PD examines the effect and mechanism of action of the drug, or what the drug is doing to the body. By design, nanoparticles have very different pharmacologic profiles when compared to their small molecule counterparts. Longer circulation times, slower release kinetics, and altered uptake throughout the body are often seen with nanoparticles. One of the large unanswered questions in the field of ultrasound mediated nanoparticle drug delivery is what happens to the nanoparticles and bubbles after administration. During a co-administration of microbubbles and nanoparticle

---

Unpublished work by LB Mullin, LC Phillips, G Song, WC Zamboni and PA Dayton

drugs, it is hypothesized that the application of ultrasound at the target (tumor) site while microbubbles are circulating will enhance uptake of the nanoparticle due to desirable bioeffects that result from exposing the microbubble to sound waves, causing oscillation and destruction, which leads to enhanced cellular and vascular permeability. This increased permeability will allow a larger amount of drug/nanoparticles to enter into the tumor tissues, hopefully resulting in a more effective cancer treatment. While multiple groups have shown reduced tumor growth with ultrasound treatment, information about what is happening at the site of ultrasound application is relatively limited. Here we use novel methods to detect both encapsulated and released doxorubicin levels within plasma and total doxorubicin concentrations within tumor tissues of mice treated with PEGylated liposomal doxorubicin (PLD), microbubbles and focused ultrasound.

7.2 Materials and Methods

7.2.1 Microbubble Preparation

A lipid mixture 1,2-distearoyl-sn-glycero-3-phosphocholine (DSPC); 1,2-distearoyl-sn-glycero-3 phosphoethanolamine-N-[methoxy- (polyethylene glycol)-2000] (ammonium salt; DSPE- PEG2K; Avanti Polar Lipids) was prepared using a 9:1 molar ratio. Briefly, lipids were dissolved in chloroform, dried and dissolved into a buffer solution of PBS. The lipid solution was then transferred into vials, which were then evacuated and filled with decafluorobutane gas. Vials were shaken with a Vialmix shaker (Bristol-Myers Squibb Medical Imaging, North Billerica, MA) for 45 s prior to injection. Microbubbles had a mean diameter of 0.71 μm and a concentration of 1.0x10^{10} MB/mL.

7.2.2 PLD Preparation

PEGylated liposomal doxorubicin (PLD) at was diluted in 5% Dextrose Injection, USP (D5W) prior to use. The dose used in all animals was 6 mg/kg.

7.2.3 Animal Preparation

Animals were handled according to National Institute of Health guidelines and the study protocol was approved by the UNC Institutional Animal Care and Use Committee.

Study 1

Studies were performed with a C3Tag genetically engineered mouse model (GEMM) that spontaneously develops mammary carcinoma tumors. When tumors reached approximately 7 mm, treatment was given.

Mice were anesthetized at 2% isoflurane on a heating pad and maintained at 1-2%. A 27 gauge catheter was inserted into the tail vein for administration of PLD and microbubbles. The transducer was placed above the center of the tumor with gel between the tumor and transducer.

Mice were treated with a Philips Therapy Imaging Probe System operated at 1 MHz, 1 MPa, 10% duty cycle, and 10 Hz pulse repetition frequency (Fig. 7.1). The transducer was programmed to scan the tumor volume, 5 s at each location. Microbubbles were diluted 1:1 in saline; 100 μL microbubbles were slowly injected by hand while ultrasound was applied to the tumor. PLD at 6 mg/kg was injected via the catheter following microbubble and ultrasound treatment.

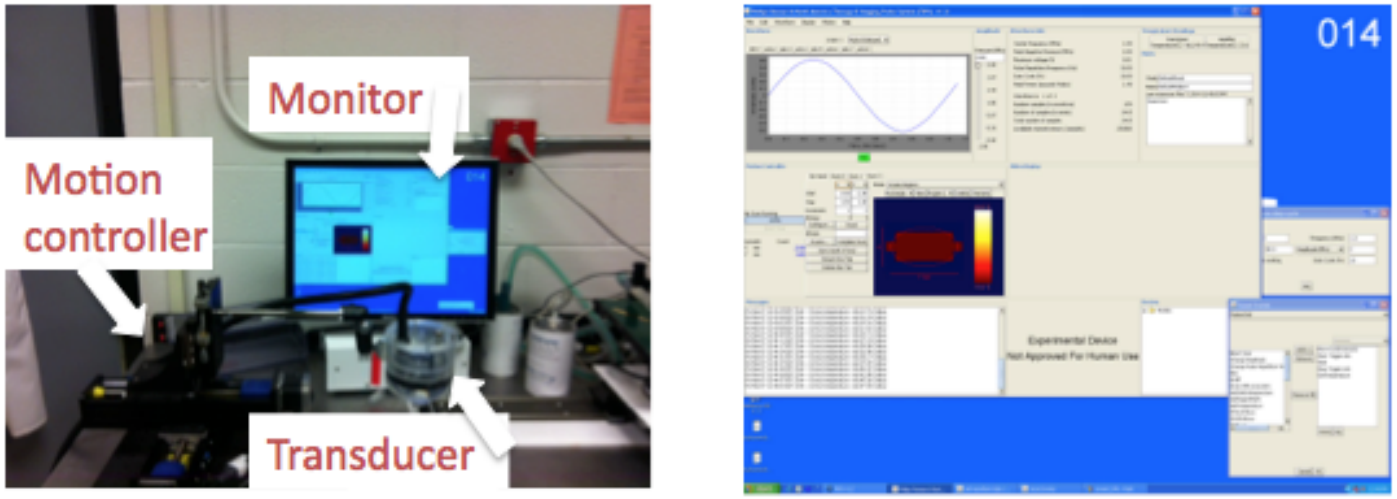

Figure 7.1: A Philips Therapeutic imaging probe system was used to treat mice in combination with PLD treatment. The tumor volume was programmed using the GUI (right) so that the transducer would scan across the tumor.

Study 2

Studies were performed in FVB mice injected with cells derived from an autochthonous (GEMM), the C3Tag ($5x10^5$ cells/injection). Tumors were treated once they reached approximately 5-7 mm in diameter.

Mice were anesthetized at 2% isoflurane on a heating pad and maintained at 1%. A catheter was inserted into the tail vein. The transducer was placed above the center of the tumor with gel between the tumor and transducer.

Mice were treated with a Philips TIPS operated at 1 MHz, 1 MPa, 50% duty cycle, 10 Hz pulse repetition frequency (Fig. 7.1). The transducer was programmed to scan the tumor volume, 5 sec at each location. PLD at 6 mg/kg was injected prior to MB/US treatment. Microbubbles were diluted 1:9 in saline; 100 μL of microbubbles were injected slowly by hand during the duration of the ultrasound treatment.

Control mice were treated with an injection on 6 mg/mL PLD.

7.2.4 Pharmacokinetic Study Design

Mice were sacrificed at 0.083, 1, 6, 24, 48 and 96 h (Study 1) and 1, 6, and 24 h (Study 2) after administration of PLD. Approximately 1 mL of blood was collected via terminal cardiac puncture following deep anesthesia and placed on ice in polypropylene screw cap tubes. Tumor tissue was divided into sections for PK analysis, IHC, and fluorescence imaging. Tumor and other tissues (lungs, liver, spleen, kidney) were placed in cryopreservation vials and preserved by snap freezing in liquid nitrogen. All tissue samples were stored at -80°C until processed.

7.2.5 Sample Processing and Analytical Methods

After collection, blood samples were immediately centrifuged at 1,500xG for 5 minutes to collect plasma. Samples were not frozen in order to avoid rupturing the liposome

structure. Solid phase separation (SPS) was carried out for the determination of encapsulated and released doxorubicin. SPS columns were preconditioned with PBS and methanol. An internal standard solution of daunarubicin in PBS was added to each column after the addition of each spiked sample. The encapsulated fraction was collected and stored at -80°C. The released doxorubicin was eluted from the column with methanol and evaporated in a TurboVap (Caliper Lifesciences, Hopkinton, MA) under nitrogen flow at 45°C. Samples were reconstituted in 150 μL of 85:15 Acetonitrile: water with 0.1% formic acid, and vortexed for 10 minutes. 125 μL were transferred to a 200 μL plastic inset in a HPLC autosampler vial. Vials were centrifuged for 10 min at 3,000xG. Samples were analyzed by HPLC using fluorescence (FL) detection with an excitation wavelength of 490 nm and emission wavelength of 590 nm.

The encapsulated fraction was further processed to determine concentration of doxorubicin within the carrier using protein precipitation with acetonitrile. Samples were removed from the freezer and allowed to reach room temperature. 2 mL of acetonitrile with Daunorubicin was added to all samples and vortexed for 10 minutes. Samples were then centrifuged for 5 minutes at 1,000xG before transferring 1 mL of the organic phase to a 5 mL propylene tube. The organic phase was then evaporated in a TurboVap. Samples were reconstituted with 150 μL mobile phase and mixed by vortex and centrifugation before being transferred to autosampler inserts. Samples were analyzed by HPLC in the same methods as the released doxorubicin.

To form tumor homogenates, tumors were thawed and sectioned. The sections were weighed and diluted in a 1:3 ratio with DI water. These mixtures were homogenized by placing zirconium oxide beads (15 small and 2 large; Omni International Inc, Kennesaw, GA) into 2 mL tubes at 3,000xG using a Precellys 24 homogenizer (Omni International Inc, Kennesaw, GA) twice for 40 s each with a 20 s wait between each run.

An extraction solution composed of daunorubicin and acetonitrile was placed into

a microcentrfigue tube filled with tumor homogenate, vortexed, and centrifuged at 10000xG for 10 minutes at 4°C. 850 μL of the supernatant was transferred to a 2 mL tube and evaporated under nitrogen in TurboVap and reconstituted in 150 μL of the mobile phase.

After vortexing for 10 min, 125 μL of reconstituted samples was transferred to a 200 μL plastic inset in a HPLC autosampler vial. Vials were centrifuged for 10 min at 3000xG before being analyzed by HPLC using fluorescence detection with an excitation wavelength of 490 nm and emission wavelength of 590 nm using an injection volume of 10 μL.

7.2.6 Pharmacokinetic Analysis

Pharmacokinetic parameters for encapsulated, released, and sum total doxorubicin were calculated by non-compartmental methods using Phoenix WinNonlin (Pharsight Corp., Mountain View, CA). The area under the concentration versus time curve from 0 to 24 h (Study 2) or 96 h (Study 1) was calculated using the linear up/log down rule. The plasma volume of distribution (Vd), clearance (CL), and half-life ($t_{1/2}$) were calculated using standard equations. The maximum concentration (C_{max} and time of C_{max} (T_{max})) were determined by visual inspection of the concentration versus time data.

7.3 Results

7.3.1 Study 1

Pharmacokinetic parameters from ultrasound treated mice were compared to previous data collected previously in C3Tag mice receiving only 6 mg/kg PLD [150]. AUC values revealed elevated amounts of doxorubicin within the tumor, along with an increase in encapsulated and released plasma level (Table 7.2).

Table 7.1: Study 1PK Parameters C3Tag GEMM

Parameter	Units	Plasma Encapsulated	Plasma Released	Tumor
MB, US, PLD				
HL	hr	26	61	
Tmax	hr	1	1	96
Cmax	ng/mL	86369	1181	16627
SE_Cmax	ng/mL	11973	103	4141
Tlast	hr	96	96	96
Clast	ng/mL	5395	212	16627
AUClast	hr*ng/mL	2976370	68126	1176218
SE_AUClast	hr*ng/mL	419407	9629	166937
Vd	mL/kg	72		
CL	mL/hr/kg	1.9		
PLD				
HL	hr	15.10	16.92	40
Tmax	hr	0.08	0.50	24
Cmax	ng/mL	82,760	1,712	6534
SE_Cmax	ng/mL	17,200	277	1895
Tlast	hr	96	96	96
Clast	ng/mL	1,199	19	2388
AUClast	hr*ng/mL	1,609,775	30,818	480111
SE_AUClast	hr*ng/mL	111,180	2,840	71419
Vd	mL/kg	79.91		
CL	mL/hr/kg	3.67		

Visual inspection of the concentration over time curves reveals differences between PLD control and PLD ultrasound treated concentrations (Fig. 7.2). Plasma doxorubicin levels decreased then increased at 48 h post treatment. Sum total values within the tumor decreased at 6 h post treatment, but increased after 24 h.

Table 7.2: GEMM C3Tag AUC Values

	AUC Plasma Encapsulated	AUC Plasma Released	AUC Tumor
Ultrasound	2,976,3709	68,126	1,176,218
No Ultrasound	1,609,775	30,818	480,111
Percent Difference	60	75	84

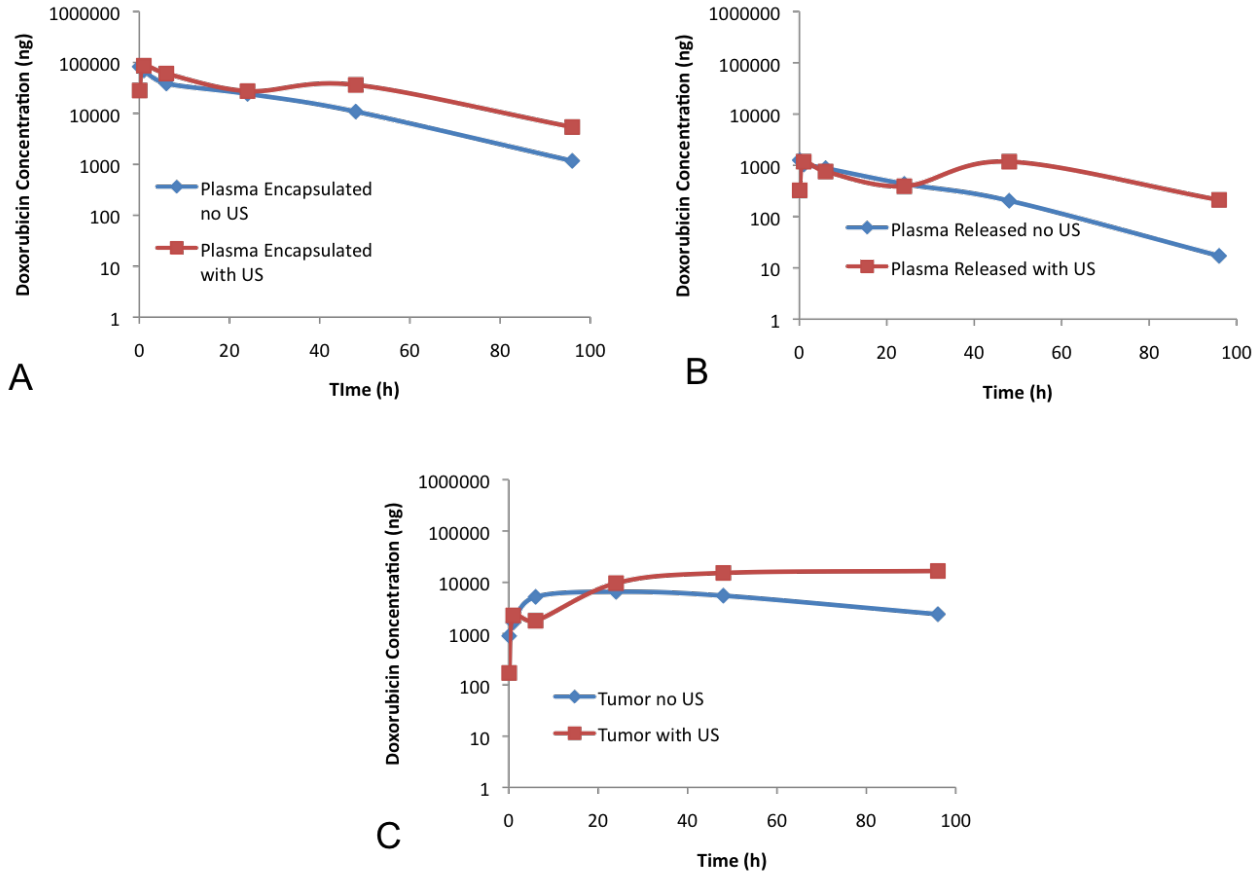

Figure 7.2: A) Concentration over time for (A) plasma encapsulated, (B) plasma released, and (C) tumor tissue after 6 mg/kg treatment by PLD alone or PLD combined with microbubble and ultrasound exposure in a C3Tag GEM model.

Ratios of tumor to plasma levels were also calculated (Table 7.3).

Table 7.3: Concentration ratios between encapsulated and released and tumor in C3TagGEMM

	tumor/encapsulated	tumor/released	tumor/total plasma	encapsulated/released
US treated	0.395	17.3	0.387	43.7
No Ultrasound	0.298	15.6	0.293	52.2

Table 7.4: Concentration ratios between encapsulated and released and tumor in implanted C3Tag

	tumor/encapsulated	tumor/released	tumor/total plasma	encapsulated/released
US treated	0.136	14.3	0.135	104.7
No Ultrasound	0.117	9.26	0.115	79.2

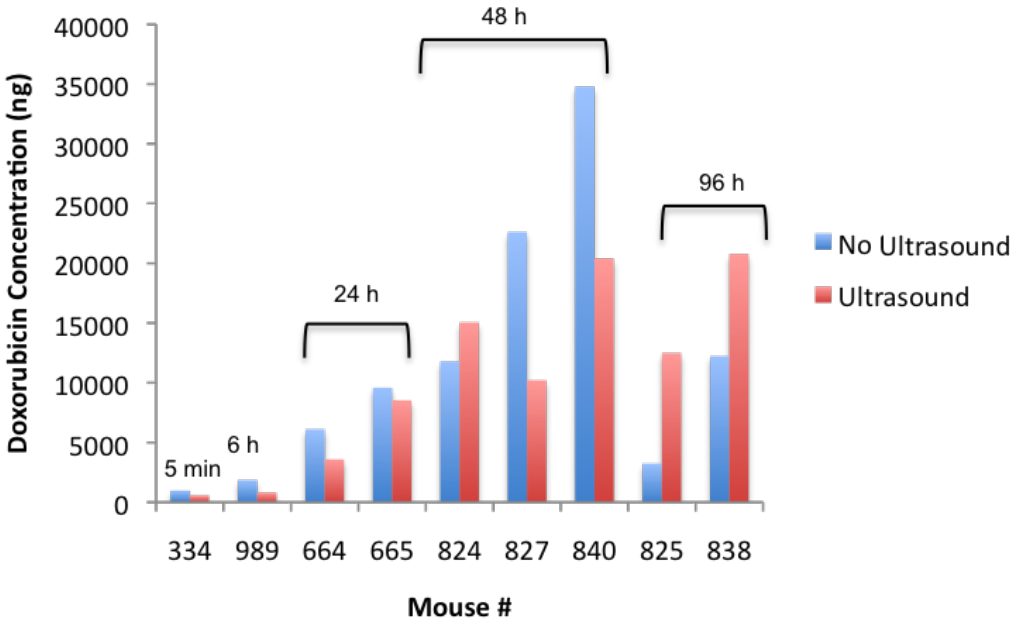

Figure 7.3: Nine of the C3Tag mice in Study 1 had secondary tumors not exposed to tumors. Doxorubicin values within the insonated and non insonated tumors are compared in the plot.

Multiple mice within the ultrasound microbubble treatment group also had secondary tumors which were not treated with ultrasound. These tumors were harvested and the doxorubicin concentration was compared to the treated tumor (Fig. 7.3). Both of the mice sacrificed 96 h after treatment had increased doxorubicin with ultrasound exposure. This aligns with the T_{max} of 96 h seen in Study 1 mice treated with ultrasound and microbubbles. At 48 h the largest difference between tumors was seen, however the increase in 2 out of the 3 mice was in the tumor without ultrasound.

7.3.2 Study 2

The concentration time curves of doxorubicin within plasma and tumor tissue is displayed in Figure 7.4. The profiles of the concentrations within mice that received only PLD and the mice that received PLD with microbubbles and ultrasound are very similar.

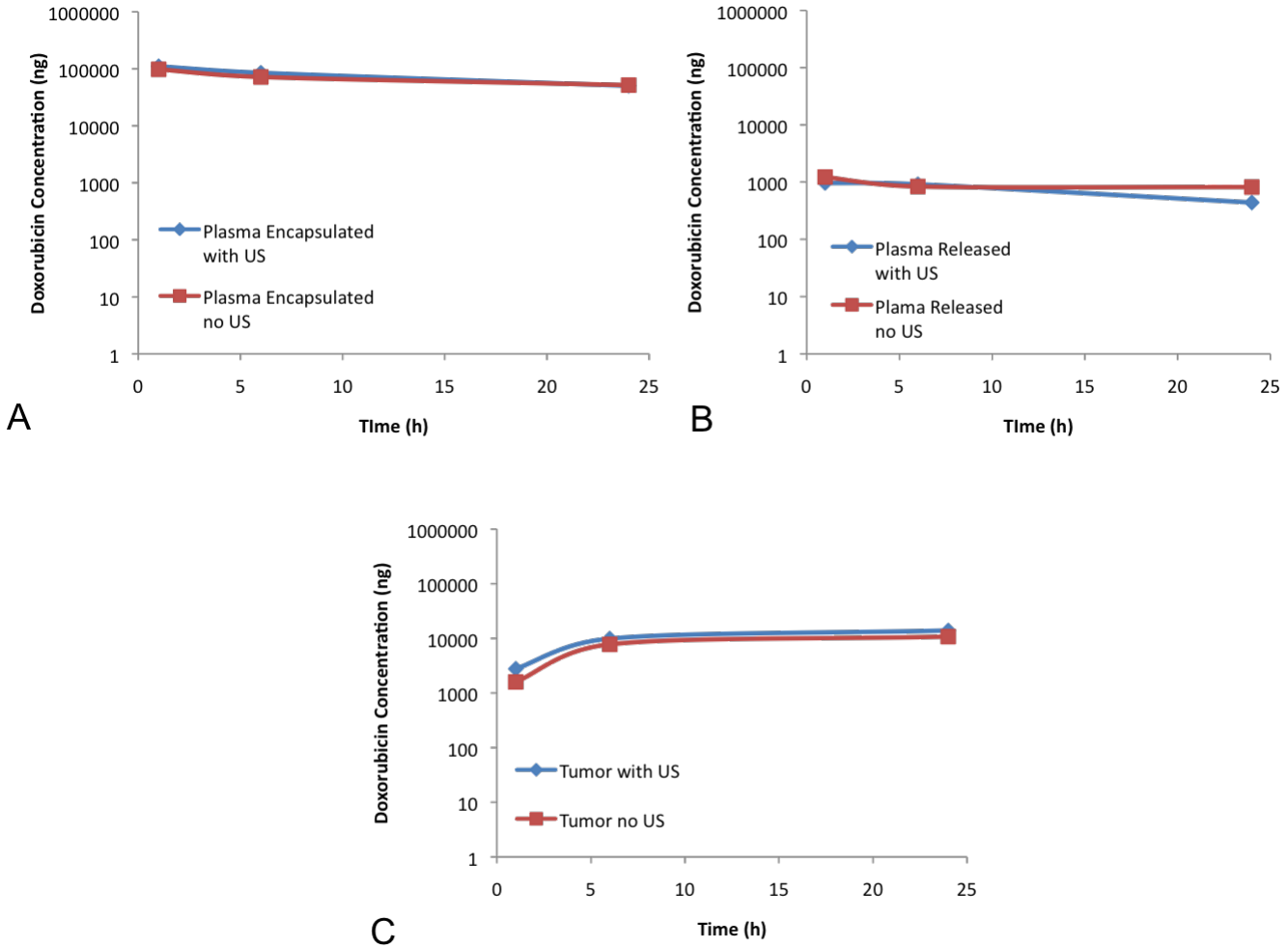

Figure 7.4: A) Concentration over time for (A) plasma encapsulated, (B) plasma released, and (C) tumor tissue after 6 mg/kg treatment by PLD alone or PLD combined with microbubble and ultrasound exposure in FVB mice implanted with C3Tag tumors.

Table 7.5: Study 2:PK Parameters Implanted C3Tag Mice

Parameter	Units	Plasma Encapsulated	Plasma Released	Tumor
MB, US, PLD				
HL	hr	21		
Tmax	hr	1	1	24
Cmax	ng/mL	110712	968	13960
SE_Cmax	ng/mL	18363	127	1520
Tlast	hr	24	24	24
Clast	ng/mL	50377	439	13960
AUClast	hr*ng/mL	1819984	17380	247921
SE_AUClast	hr*ng/mL	167904	1000	14750
Vd	mL/kg	54.5		
CL	mL/hr/kg	1.8		
PLD				
HL	hr	27		
Tmax	hr	1	1	24
Cmax	ng/mL	98052	1225	10791
SE_Cmax	ng/mL	6827	195	2109
Tlast	hr	24	24	24
Clast	ng/mL	51757	820	10791
AUClast	hr*ng/mL	1638623	20685	191470
SE_AUClast	hr*ng/mL	41355	1644	30180
Vd	mL/kg	64.4		
CL	mL/hr/kg	1.6		

Ratios of tumor to plasma levels were also calculated (Table 7.4).

7.4 Discussion

In the field of preclinical drug delivery, there is debate over the appropriate mouse model to use for studying drug formulations. There are several options of tumor models, which include syngeneic and xenograft mouse tumors or autochronous models such as genetically engineered mouse models that have genetic mutations that cause spontaneous tumor development. Syngeneic models are mouse tumors injected or implanted ectopically or orthotopically (within the organ of origin). These are advantageous

Table 7.6: Implanted C3Tag AUC Values

	AUC Plasma Encapsulated	AUC Plasma Released	AUC Tumor
Ultrasound	1819984	17379	247921
No Ultrasound	1638623	20685	191470
Percent Difference	10.5	-17.3	25.7

because they do not require immunocompromised mice, are low cost and are highly reproducible [151]. However, they may not accurately represent the human condition of this disease [152]. Xenograft models use human cells/tumors in a murine environment. This model is also cost effective and reproducible, but interactions between cells from different species may produce tumor environments that are not an accurate model of the human tumor microenvironment. These transplantable models may also lead to misrepresentations of the tumor environment with respect to vessel permeability. A possible solution to these problems is the use of GEM models that develop tumors in the appropriate organ, but these studies can be difficult to use due to the delayed onset of tumor and low tumor incidence within mouse colonies [151].

Both because of the difficulty in acquiring appropriate animals per treatment group, and the differences in tumor environment, two types of models were used for this investigation into the pharmacokinetics of PLD combined with ultrasound treatment. Study 1 used a GEM model, whereas Study 2 was conducted in a orthotopic syngenic model.

In Study 1, PLD alone treatments were performed previously by collaborators [150]. Ultrasound parameters were selected based on a review of the literature. Similar studies performed by Lin *et al.* saw increased delivery at 24 h post treatment with a similar setup, and this was selected as an end time point for preliminary studies [115].

Tumors developed from cell injections, may have increased permeability compared

to GEMMs. Changing the tumor model for Study 2 allowed investigation into if this concept could be seen for C3Tag tumors. Additionally, the implanted tumors have a more predictable tumor growth pattern which aids in study feasibility.

Ultrasound parameters that were modified between studies include increased duty cycle from 10% up to 50%. Increasing the duty cycle increased overall ultrasound exposure within the tumor. The microbubble were also diluted 1:9 instead of 1:1. As discussed in Chapter 3, microbubble concentration can play an important role in increasing permeability.

In both studies, elevated concentrations of doxorubicin were found in the tumor with the application of ultrasound. However, along with elevated tumor levels, plasma levels were also elevated in the animals treated with ultrasound. This data could indicate the microbubbles circulating with the liposomal doxorubicin may interfere with MPS clearance of the drug. Further investigation into how the circulating nanoparticles are recognized by the immune system could provide more details on this mechanism. Alternatively, it is possible that in the current method of delivery, there is not a significant increase in drug concentration within the tumor, but that other mechanisms might be responsible. This could be supported by data shown in Figure 7.3. An efficacy study performed over 6 weeks with a weekly treatment schedule will investigate the efficacy of the ultrasound treatment to inhibit tumor growth.

Additional time points for Study 2 could support the trend of a increase at 24 hours post treatment in the ultrasound group compared to PLD control. In Study 1, the concentration time curves become more distinct after 25 h, however this data has not be obtained yet for Study 2.

While it was hypothesized that ultrasound in the presence of microbubbles would increased the drug concentration at the tumor site, it is possible other mechanisms may have a more important role when the drug is not bound to the microbubble. Analysis of

the untreated secondary tumors in Study 1 may indicate that the ultrasound parameters may need to be adjusted in hopes of increasing the drug concentration within the ultrasound treated tumor. The data presented in Figure 7.3 is not normalized to tumor volume. When multiple tumors were present in an animal, the tumor most accessible by ultrasound (away from the head) was selected. Most times this was also the larger of the two tumors.

Previous studies have shown that the order of administration does not effect nanoparticle uptake within the tumor [98], yet the state of nanoparticles, liposomes in particular, has been under investigation. It is possible that variations in the ultrasound settings may provide an environment where liposomes would rupture. This would be an additional methods of causing a spike in drug concentrations within tumor tissue. However, data presented here also indicate that the ultrasound is not breaking the liposomes. In Study 2, PLD was administered prior to ultrasound exposure, yet there was not an increase in released doxorubicin concentration (Table 7.4). Although Study 1 does show an increase compared to without ultrasound, the PLD was administered after the tumor was exposed to ultrasound and is therefore not responsible for the difference.

Future studies with bound nanoparticles will allow a greater understanding of the impact of route of administration- whether the drug is administered separated, or joined to the microbubble. Nanoparticles are known for their long circulation times, however binding the agent to the microbubble may cause the drug to decrease from hours or days of circulation, down to minutes. While the full clinical implications of this change in pharmacokinetic profile are unknown, it is believed that delivering a higher amount of drug to the tumor, but limiting systemic exposure may achieve a greater therapeutic index.

7.5 Conclusions

The effects of ultrasound and microbubbles on doxorubicin pharmacokinetics were investigated. Two animal models and two sets of ultrasound parameters were studied. Elevated doxorubicin levels were seen both in the plasma and the tumor for Study 1 when ultrasound was applied. Encapsulated drug levels and total drug within the tumor were elevated in Study 2 with the addition of ultrasound. Future work involving efficacy studies and longer time points will provide more information about possible mechanisms causing the increased tumor uptake.

CHAPTER 8

Concluding Remarks

8.1 Summary

The work presented in this dissertation works towards the application of ultrasound and microbubbles to enhance nanoparticle drug delivery. Studies advance from *in vitro* testing of acoustic and microbubble parameters (Chapters 3 and 4) to *in vivo* evaluation of delivery of nanoparticles and therapeutic efficacy (Chapters 5, 6, 7). Both co-administration and loaded microbubbles are used throughout this work.

Novel contributions include an in depth look at the role of microbubble size in sonoporation (Chapter 3), where size isolated microbubbles are used. The ability to create microbubble populations of a specific size range can have many advantages. According to our data, fewer microbubbles may be need to achieve the desired bioeffects which increase permeability. In addition, controlled size can allow for controlled loading onto microbubbles. Knowing the size of the microbubble can allow for tailed ultrasound parameters to be used, since the resonance frequency of microbubbles is dependent on the size of the bubble. Acoustic responses, such as oscillation and translation from radiation force, vary based on size. Future work optimizing these settings is still needed, but

these results will be important moving forward with ultrasound microbubble enhanced delivery.

In Chapter 4 a novel nanocapsule loaded microbubble is created. These nanocapsules have been shown to overcome drug resistance in tumors [141]. We show the nanocapsules can be easily modified to bind to the shell of the microbubble. This loading potential of the microbubble is an appealing characteristic due to the limited payload that could be retained within the shell itself. In this chapter the ability to achieve targeted delivery *in vitro* to a cell monolayer is demonstrated.

In Chapter 5, *in vivo* co-administration study was performed. Using a therapeutic ultrasound system, low dose nanocapsules were administered 3 times per week for 2 weeks in combination with microbubbles and ultrasound. The mice receiving nanocapsules, ultrasound, and microbubbles had statistically significant tumor volumes on several days throughout the study. The use of an aggressively growing tumor was not ideal for testing the effect of ultrasound mediated delivery as the tumors didn't respond to treatment as well as expected. This study only relied on tumor volume to evaluate drug delivery, and did not measure actual concentration of paclitaxel within the tumor. Additional limitations of this study are that the control group used for comparing tumor response was from an earlier study, making comparisons difficult, and the dose selection may have been too low.

In Chapter 7, drug concentrations within plasma and tumor were measured to evaluate the effects of ultrasound. The study combined the use of a preclinical commercial therapeutic transducer with microbubbles and liposome treatment and provides a novel look at drug concentrations after ultrasound treatment. Analysis methods provided information about encapsulated and released doxorubicin concentrations up to 96 h after treatment. Increased concentrations were seen within the tumor tissue, along with

elevated plasma levels. Future efficacy studies are needed to determine if other mechanisms, such as microbubble shielding of the liposomes causes increased levels.

In Chapter 6, a clinical ultrasound system is used to deliver radiation force and microbubble destruction *in vivo*. Targeted fluorescent AADVs and targeted fluorescent microbubbles are injected into tumor bearing rats and mice. Optical imaging methods were used to assess delivery to tumor tissue. Fluorescent bubble delivery was seen in preliminary studies. Future work will increase the number of animals treated. Incorporating a drug loaded nanoparticle will eliminate issues with tissue autofluorescence issues and allow for a more precise measurement of the effectiveness of treatment with a clinical system.

8.1.1 MB Formulations

Throughout this work, various microbubble formulations were used to study the ability of microbubbles and ultrasound to enhance delivery. Table 8.1 provides details of each of types of bubbles used, including specific shell components, modifications for conjugation, size and method used for forming bubbles from the lipid solution. An advantage to making our microbubbles in our own laboratory is the ability to tailor the formulation based on the application.

8.1.2 Ultrasound Sources

Several ultrasound systems are also used throughout this work to achieve delivery (See Table 8.2). *In vitro* studies were carried out with a piston transducer energized by a waveform generator and RF amplifier. This system allowed maximum control of ultrasound settings including number of cycles, PRF, duty cycle and pressure. A system like this is ideal for investigating the effects of various parameters is a simplified manner. For example, increasing the pressure for sonoporation studies can be achieved simply by increasing the voltage signal. These studies demonstrated the ability of

unfocused and focused ultrasound to manipulate microbubbles. These studies however did not incorporate imaging uses of ultrasound.

In vivo studies were performed using three different types of ultrasound systems. The first system used was a commercially available system used for physical therapy applications. The Sonicator 740 is lightweight, portable system allows for limited control of frequency, intensity, and duty cycle. The system allowed for parameters to be easily matched to literature intensity and duty cycle, although full control over the signal not possible. Duty cycle options are 10%, 20% or 50%, with a set PRF of 100 Hz. Intensity values up to 2.2 W/cm^2 are possible. This transducer was unfocused allowing for treatment of the entire tumor at once, but did require slight movement of the transducer to avoid tissue heating due to hot spots on the transducer. Co-administration of nanocapsules and microbubbles did not require radiation force for delivery, which made the 1 MHz transducer ideal for treatment. This system again did not allow for imaging of the tissues.

In Chapter 6, *in vivo* studies were carried out with a clinical ultrasound scanner. Settings on the Siemens Sequoia 512 were manipulated to achieve radiation force and microbubble destruction. This system also allowed for image guidance to be used. CPS mode was used to image the contrast, which confirmed the loaded vehicle had reached the tumor site. In order to treat the entire tumor, a motion stage was required to translate the transducer across the tumor. Multiple types of nanoparticles and targeted nanoparticles were administered in these studies. Fluorescence detection proved to be a challenge in these studies.

The final system that was used in this work was the Philips therapy and imaging probe system (TIPS). This system has been discontinued by Philips. With the TIPS, a controller PC allows custom programming of the transducer output and scanning pattern of the transducer over the region of interest. This system is specifically designed

for use with mice and rats, and it is designed to allow users to treat target areas with specific ultrasound parameters. This technology is an ideal match for *in vivo* studies using the microbubble delivery vehicles developed in the current project. Although it was not used as part of our study, ultrasound imaging can also be performed with the system through integration of a higher frequency transducer into the therapy probe. This will allow precise location of a tumor regions within a subject and exposure of only the tumor region to ultrasound.

Table 8.1: Summary of MB and NP used for each study in this dissertation.

Chapter	Gas	Shell	Size	Method	NP
3	PFB	DSPC, DSPE-PEG2K	<1 μm	shaken	[none, calcein]
3	PFB	DSPC, DSPE-PEG2K	2, 4 μm	centrifugation	[none, calcein]
4	PFB	DSPC, DSPE-PEG2K DSPE-PEG2K Biotin	4-5 μm	centrifugation	avidin yellow polystyrene 400 nm nm
4	PFB	DSPC, DSPE-PEG2K DSPE-PEG2K Biotin	4-5 μm	centrifugation	GFP BTM NC
4	PFB	DSPC, DSPE-PEG2K DSPE-PEG2K Biotin	4-5 μm	centrifugation	C-22 PX BTM
5	PFB	DSPC, DSPE-PEG2K DSPE-PEG2K Biotin	¡ 1 μm	Shaken	C22 PX BTM NP
6	PFB	DSPC, DSPE-PEG2K, DSPE-PEG2K Biotin	2 μm	centrifugation	cRGD, blue avidin 200 nm
6	PFB	DSPC, DSPE-PEG2K, cRGD, DiR	2 μm	Shaken, then centrifuged	[none, FL shell]
7	PFB	DSPC, DSPE-PEG2K	<1 μm	Shaken	PLD, co-administered

Table 8.2: Summary of ultrasound systems and settings used for each study in this dissertation.

Chapter	Ultrasound	Settings
hline 3	unfocused 1 MHz piston	1 Mhz, 100-1.2 Mpa, 0.15-150 Hz PRF, 5 cycle
3	unfocused 1 MHz piston	1 Mhz, 300 kPa, 150 Hz PRF, 5 cycle
4	focused 2.25 MHz	3.5 MHz, 50kPa; 1.5 MHz, 1.2 MPa combined 3 s PRF of 150 mHz PRF, 30% DC
5	Sonicator 740 1 MHz	1 MHz, 2 W/cm^2, 10% DC
6	Siemens Sequoia 15L8	PW Doppler 7 MHz, 13 kPa, 25% DC, 25 kHz PRF 70 cycles; D Color MI 1.9
7	Philips TIPS	1 MHz, 1 MPa, 10 Hz PRF, 10-50% DC

8.2 Future Directions

The next step in evaluating the use of ultrasound to enhance chemotherapeutic delivery is to attach a drug loaded nanoparticle to the microbubble to create an acoustically active delivery vehicle that can be controlled externally by ultrasound. Attaching a drug containing nanoparticle, may overcome the detection challenges that were faced in the work described in Chapter 6. Continuing with methods used throughout this dissertation, future studies that attach doxorubicin liposomes to the microbubble shell could help increase delivery to tumors. Potential ways to attach the doxorubicin liposome to the bubbles include using avidinbiotin, maleimide-thiol or carboxylic acid-amine [153; 154]. Additionally, future work could employ a custom designed TIPS transducer that operates at both 1 MHz and 3 MHz to achieve both radiation force and destruction. Using the TIPS in combination with a imaging transducer will ensure the tumor is being targeted. Harvesting of the tumor and organs would be carried out and analyzed as done previously in Chapter 7. Special attention would be given to comparing concentrations seen in organs such as the liver and spleen when the liposome is free or bound. It is hypothesized that a greater difference in doxorubicin concentration will be seen within the tumor compared to free PLD and microbubble administration

and less doxorubicin will be measured in the plasma.

Future work evaluating drug deposition into tumors can be studied using microdialysis methods could answer questions about how effective ultrasound delivery methods are at overcoming barriers to delivery such as being able to exit the vasculature [155; 156]. Using a small probe inserted into the tumor, drug concentrations within the tumor can be measured over time. These methods can be used to detect both free and encapsulated doxorubicin within the tumor. This study would provide insight into the state of the liposome after ultrasound exposure and provide knowledge about whether the drug is entering into the extracelluar matrix of the tumor. An alternative method to measure delivery into the tumor would involve using an optical probe that can detect fluorescent signal from a nanoparticle. This could be done using Doxil, which is fluorescent, or another fluorescent nanoparticle such as the polystyrene beads used in previous studies. This method may overcome the limitation of previous studies with weak signal and interference from tissue autofluorescence.

A drug loaded AADV could also be used in future studies performed with the Sequoia 512 system. As with the TIPS studies, PK analysis of tissues would valuable information regarding the enhancement effect seen with ultrasound. Future studies could also take advantage of research software to measure perfusion before and after treatment. This novel volumetric imaging technique allows quantitative assessment of blood flow in an entire sample volume, unlike traditional 2-D ultrasound, which only provides qualitative information in a single slice of tissue [157]. Additionally, the therapeutic response can be observed in tumors much more accurately by monitoring blood perfusion versus caliper measurements only.

8.3 Clinical Translation

There are still many obstacles to overcome to translate microbubble-mediated ultrasound delivery of nanoparticles into a clinical setting, but progress is being made as more *in vitro* and *in vivo* studies are being published. Work remains to be done on understanding the mechanisms taking place *in vivo* to ensure that safe delivery can be achieved. Bioeffects will need to be closely monitored, because tissue damage has been seen in some studies [87]. It will also be important to understand the biodistribution and pharmacokinetics of the nanoparticles when delivered with microbubbles. As discussed earlier in liposome nanoparticles generally have long circulation times, but when bound to microbubbles, the complex is limited to the 5 to 10 min circulation time of the microbubble [57]. Although the microbubble-mediated delivery method will increase the nanoparticle concentration at the target site, accumulation in other organs is always a major factor to consider, because drug or gene accumulation in non-targeted organs/tissues could be detrimental.

Another area that is actively under investigation is the effect of ultrasound on the integrity of the nanoparticle, and how bound nanoparticles disassociate from microbubbles. There have been conflicting reports about how and if the nanoparticle is released from the shell. Lum *et al.* detected lipid labeled with DiI on the nanoparticles after breaking the microbubble [95]. However, other groups have found that the nanoparticle breaks free[54; 60; 113]. Ultrasound exposure has also been shown in some cases to cause release of the contents [57; 114], whereas in other studies, the cargo remains intact within the liposome carriers [112; 113].

Loading optimization also needs to be addressed. Liposome loading on microbubbles has been estimated at between 600 and 10000 liposomes per microbubble, depending on the size of both the microbubble and the liposome [54; 56; 57]. This may be complicated further by the fact that lipids are not uniformly distributed through the shell layer of

microbubble, resulting in heterogeneous loading of nanoparticles [95; 158]. Uniform loading is desirable to accurately quantify the amount of drug or gene on each bubble, and therefore delivered to the target site. Optimization of loading is challenging because it is frequently difficult to determine concentrations of nanoparticle solutions because of their small size. Although binding can be confirmed through methods such as flow cytometry, UV spectrometry, and microscopy, exact numbers of bound nanoparticles are difficult to obtain.

Further optimization of both ultrasound settings and delivery vehicle design are also needed. Because a variety of systems exist which deliver ultrasound energy, there is also a wide range of settings in use. Currently, comparisons between studies are hard to make because of the highly variable acoustic parameters used from study to study. In addition to ultrasound systems and settings, different microbubble formulations and nanoparticles are used that influence the results of each study. Further refining of microbubble populations through size selection techniques may be a way to improve the effectiveness of delivery methods. Microbubble populations with high uniformity in size may allow optimal loading of particles onto the shell and better prediction of the microbubble's response to ultrasound [159; 160]. Additionally, further study of the tradeoffs between bound and free nanoparticle delivery is needed for each application.

Translating research into the clinic is a very slow process. Drug development can easily take beyond 10 years. Ultrasound enhanced nanoparticle drug delivery has more than one component that will need to be approved/cleared by the FDA. However, this can be managed by working with already available drug formulations, contrast agents, and ultrasound systems. Although not with optimized parameters, the concept can be, as has already been, demonstrated in a clinical system. Recently one of the first clinical studies investigating the use of microbubbles and ultrasound to enhance efficacy of chemotherapeutic treatment has been published [161]. Five patients with

nonresectable pancreatic adenocarcinoma were treated using A GE LOGIQ 9 scanner, 4C transducer, SonoVue microbubbles and gemcitabine chemotherapy. A comparison to a control group of 80 patients treated with gemcitabine alone showed that ultrasound treatment increased the number of treatment cycles, prolonging the quality of life in patients with pancreatic adenocarcinoma. This first of its kind study provides hope that ultrasound exposure will contribute to improving cancer care in patients.

Safety is a major concern for bringing any new drug or device to market. While both ultrasound imaging and microbubble contrast agents are generally regarded as safe, there have been concerns in the past regarding safety of the microbubbles. After four deaths were reported in patients who had been administered contrast, the FDA issued a black box warning in 2007 which listed several contraindications and monitoring requirements [162]. After a review of the data, the warning was modified to only include contraindications for patients with known hypersensitivity to perflutren, (or albumin for Optison), patients with fixed cardiac shunts. These changes to the label affected the use on contrast in clinics, and may still hinder advances in contrast imaging/therapy in the United States [163].

Introducing microbubble agents for use in therapy, where bioeffects are desired, presents more safety issues that will need to be addressed. Extensive research will need to be done to demonstrate the effects are restricted to the desired location, and not negatively impacting surrounding tissues. These studies can be done by monitoring surrounding areas for changes in temperature, blood flow, or other tissue characteristics [164].

FDA limits on output exist for diagnostic imaging in order to prevent thermal effects and cavitation. These limits are on the mechanic index (MI)- must be below 1.9 and the spatial peak time averaged intensity (I_{spta}) must be below 720 mW/cm^2. These limits were established in 1976, and do not necessarily accurately represent the limits

of safe use of ultrasound. Additionally, these settings are for diagnostics, and therefore the development of a therapy system does not necessarily have to operate within these limits. Currently there are numerous therapeutic ultrasound systems that have been cleared by the FDA which fall outside of these limits. In HIFU, intensities of up to 10,000 W/cm^2 are use to treat tumors and uterine fibroids. Lower intensity systems are in use in physical therapy clinics for heating tissues and treating bursitis and tendinitis. The existence of these systems may improve the likelihood for approval of a system for drug delivery.

Beyond the hurdles of FDA clearance/ approval, there are limitations to the method of treating tumors with ultrasound and microbubbles. The tumor needs to be accessible to interrogation from the ultrasound beam, which puts limits on types of tumors and sites. For example, tissues deep within in the body or within the lungs would be difficult due to signal attention and air reflections, respectively. This also requires the location of the tumor to be known. Many cancers metastasize, and small molecule drugs will be able to attack these cells with more success than spatially localized tumor. Combining ultrasound-mediated treatment with other treatment options may be a solution to this drawback.

Creating one system that fits all the ideal characteristics may not be realistic, especially when drug loaded microbubbles are in use. Treatments with various drugs would require a new AADV. A single bubble, however, could be designed to be used when co-administration is the route of delivery.

In an ideal system, the location to be treated would be visualized using ultrasound imaging, the region to be treated would be selected, such as with an ROI tool, and the therapeutic ultrasound would be applied only to this region. This requires that information. Control over frequency, pulse length, duty cycle, pressure, is needed and

should also be displayed. In order to avoid damage to tissues above or below the treatment area, focused treatment should be used. This also would require the transducer to be moved across the area. Detailed information about the ultrasound pulse, such as axial, lateral, and elevational full-width half-max of the ultrasound pulse, is needed to determine the necessary adjustments to treat the desired area. How the microbubble and drug are linked, or not linked, will impact the type of ultrasound system that will be needed. For co-administration, imaging and destruction pulses are needed; using bound AADVS would require the addition of radiation force pulses. ARF pulses are typically longer than that is used in diagnostic imaging, however, and modifications to current clinical scanners can be use to alter settings such as pulse length that are needed for optimized radiation force.

Other types of systems to consider for ultrasound drug delivery are intravascular ultrasound systems that would release the microbubbles and drug internally form the same location the ultrasound is emitted. The feasibility and effectiveness of this type of treatment has been shown by multiple groups [165; 117].

8.4 Conclusions

Microbubbles are an appealing choice for enhancing nanoparticle targeted drug delivery. Nanoparticle chemotherapeutics can be combined with the microbubbles, and through the external control of ultrasound, localized delivery can be achieved. There are still many areas that require further investigation, however, many advances are being made in the use of ultrasound and microbubbles and the approach is developing into a promising method to improve cancer treatments.

APPENDIX A

Review of Nanoparticle Delivery Studies

Table A.1: Summary of *In Vitro* Studies. Abbreviations used in the table: cycle (C), cycles per pulse (CPP), duty cycle (DC), pulse repetition frequency (PRF), peak to peak (p-p), quantum dots (QD), frame rate (FR), pulse length (PL), pulse repetition period (PRP), polystyrene (PS), biotin-avidin (B-A), and maleimide-thiol (M-T).

Ref.	Transducer	Settings	MB	NP	Linked?	Model
[166]	Unfocused	1 MHz, 0.5 MPa, 10 Hz PRF, 1050% DC, 1090 s	Optison	PS 20-100 nm; CdSe QD 20 nm	-	MCF-7 cells and spheroids
[57]	Philips TIPS focused	1 MHz, 7MPa, 5 pulses, 100,000 CPP	Lipid biotinylated	liposomes, calcein, thrombin	B−A	Canine blood
[54]	Spherically focused	2.25 MHz, 3 C pulse; 5 MHz, 150 kPa, 5x10^6 C 3 short 1.9 MPa, 5 CPP 120 s at 0.25 Hz	Lipid biotinylated	liposome 100 amd 200 nm	B−A B−A	PC3 cells
[95]	Focused single element 2.25 MHz	1.3 s at 3 MHz, 150 kPa, 5 C; 5 CPP 1.5 MHz, 1.1 MPa	Lipid biotinylated	neutravidin coated latex beads 40 and 100 nm	B−A	cellulose tube
[79]	Single element 30 mm diameter	1 MHz, 20 C, 10kHz PRF, 0.1- 0.75 w/cm^2; 40 s	Polymer	Fe3O4 12 nm	in shell	SMMC 7721 cells
[167]	ATL/Philips HDI 5000 linear transducer	12-5 MHz, doppler: MI 0.4−0.45, PRF 1000 Hz;	PLA polymer	nanoshard after burst; polymer np	part of shell	mda-mb 231 MCe7 cells
[61]	Sonitron 2000	1 MHz, 10% DC, 2 W/cm^2	Lipid biotinylated	lipoplex	B−A	HUH7, HUH7e GFPLuc cells
[102]	ATL/Philips HDI 5000	5 MHz, doppler, 1000 Hz PRF, 10 Hz FR, 1.0 MI; 20 min scan	PLA polymer	nanoshard after burst	in shell	mda-mb 231, MCe7 cells
[56]	Sonitron 2000	1 MHz, 20% DC,2 W/cm^2; 10-15 s	Lipid Thiol functionalized	liposome 200 nm	M−T	BLM cells
[62]	Sonitron 2000	1 MHz, 2 W/cm^2, 50% DC, 30 s	Lipid biotinylated	mRNA lipoplex	B−A	dendritic cells
[114]	Sonitron 2000	1 MHz, 50% DC, 2 W/cm^2; 15 s 0.17 MPa, 0.17 MI	Lipid-biotinylated	liposome	B−A	BLM, HUH-7 cells
[60]	Sonitron 2000	1 MHz, 10% DC, 2 W/cm^2; 10 s	Lipid biotinylated	cationic liposomes, lipoplexes, siPlexes 125- 325 nm	B−A ,	PAEC, PVSMC cells
[117]	Unspecified Rich-Mar system	2 W/cm^2, 50% DC, 30 s	Lipid	rapamycin SPIO nanoparticle	in shell	PAEC, PVSMC cells
[113]	Sonitron 2000	1MHz, 10% DC, 2 W/cm^2; 10 s	lipid biotinylated	liposome- siPlex	B−A	HUH7, HUH7e GFPLuc cells
[59]	Topteam 161	PRF 100 Hz, 0.5 W/cm^2, 60 s, 50% DC	Sonovue	mPEG-PLGA-PLL containing siRNA	-	RPEJ cells
[112]	Sonitron 2000	1 MHz, 10% DC, 2 W/cm^2, 10 s	lipid-biotinylated	Liposome- siplex 120 nm	B−A,	BLM cells
[168]	Focused 1 MHz	1 MHz,100 s PRP, 40 CPP 30 s 200−600 kPa	Lipid-thiol functionalized		M−T	U-87 MG cells
[169]	20 mm probe	1 MHz, 20% DC, 1.65 W/cm^2, 0.35 MPa, 15 s	Lipid-biotinylated	liposome- dox	B−A	MCF-7/ADR cells
[170]	Sonitron	1 MHz, 50% DC, 600 kPa,	Lipid-thiol functionalized	liposomes	M−T	HMB2, BLM cells

Table A.2: Summary of *In Vivo* Studies. Abbreviations used in the table cycle :(C), cycles per pulse (CPP), duty cycle (DC), pulse repetition frequency (PRF), peak to peak (p-p), quantum dots (QD), frame rate (FR), pulse length (PL), pulse repetition period (PRP), polystyrene (PS), biotin-avidin (B-A), and maleimide-thiol (M-T).

Ref.	Transducer	Settings	MB	NP	Linked?	Model
[115]	Focused 1.0-MHz 38 mm diameter	10 ms PL, 1% DC, 1 Hz PRF,120 s, 1.2 MPa	SonoVue	Doxil (100nm)	-	Balb/c mouse; CT-26 tumor
[53]	Focused 1.0 MHz 38 mm diameter	10 ms PL, 1% DC, 1 Hz PRF, 120 s, 1.2 MPa	SonoVue	Lipid coated QD 30- 180 nm	- -	Balb/c mouse; CT-26 tumor
[98]	Focused 1.0-MHz 38 mm diameter	10 ms PL, 1% DC, 1 Hz PRF,120 s , 1.2 MPa	Sonovue	Lipid coated QD 130 nm	-	Balb/c mouse; CT-26 tumor
[111]	not specified	1 MHz, 1 v p-p pulse every 3 s for 150 s	Albumin	PS or PLGA (100 nm)	-	c57BL/6J mice hind limb
[58]	Unfocused 0.75 in diameter, 1 MHz	1 MHz, 5 pulses, 300 CPP, 1 v p-p, every 5 s for 12 min; 0.75 MPa	Albumin	PLGA	carboiimide chemistry -	Balb/c mice hind limb wistar rats
[87]	Sonnos 5500, S3 broadband transducer	1.3 MHz, 1.8 MPa , 110 lines in 50 ms 4 C over 3 us	PESDA	FL spheres 30 nm, 100 nm		wistar rats
[86]	HDI 3000cv	2.3 MHz, 4 C pulse over 0.1 ms; 128 lines forming 90 $^{\circ}$ sector	Optison	polymer spheres 205 nm, 503 nm	-	Sprague-dawley rats
[167]	ATL/Philips ; HDI 5000	5 MHz, Doppler: MI 1.0, 20 min scan	PLA polymer	nanoshard after burst;	part of shell	VX2 liver cancer rabbits
[102]	ATL/Philips HDI 5000	5 MHz, Doppler, 1000 Hz PRF, 10 Hz FR, 1.0 MI; 20 min scan tumor 0.17 MPa, 0.17 MI	PLA polymer	nanoshard after burst	in shell	VX2 liver cancer rabbits
[171]	Focused: Philips TIPS Sonicator 740	1 MHz, 1 MPa, 6 min 6 scans 2 min	Definity	liposomes, dox	-	MDA-MB-231-luc cells SCID mice BALB/c mice
[110]	focused single element	1 MHz, 100 C, 1 v p-p, 0.75 MPa	Optison	Polymer microspheres (100nm)	-	Sprague-Dawley rats
[116]	ATL/Philips HDI 5000 linear transducer	5 MHz, Doppler MI 0.4-0.45, 1000 Hz PRF, 20 min	PLA polymer	Nanoshard; 400 nm	part of shell	ACI rats, 3924 tumors
[147]	Focused, single element	1 MHz, 10 ms PL, 1% DC, 1 Hz PRF, 10 min 300 KHz; 2 W/cm^2; 20 min	lipid biotinylated	QD, lipsome, PX	B−A	Balb/c mie 4T1 tumor
[172]	spherically focused	0.5 MHz, 1.2 MPa, 6% DC, .5 Hz PRF, 4 min	SonoVue	liposomes		C57BL6 mice B16-F10-luc tumors
[173]	MyLab90	2.5 MHz, 0.9 MI	SonoVue	PEG PLA		Kun-Ming mice
[174]	Sonidel Sp100	1 MHz, 100% DC, 2-5 W/cm^2, 2 min,.39 MPa	Lipid-thiol functionalized	liposomes	M−T	NMRI mice
[145]	Unfocused 0.75 in diameter	1 MHz, 100 CPP, 5 s for 60 min 1.2 MPa	Albumin	PLGA	Covalent Bond	C57BLJ6/Rag-1 mice, C6 glioma

APPENDIX B

Effect of Anesthesia Carrier Gas on *In Vivo* Circulation Times of Ultrasound Microbubble Contrast Agents in Rats

B.1 Introduction

Microbubble contrast agents (MCAs) are currently implemented in many ultrasound imaging studies to provide enhanced resolution of a vascular network [175; 176; 177] as well as to act as vehicles for therapeutic applications [26; 178] . These contrast agents are lipid-encapsulated gaseous microspheres, ranging in diameter from 1 to 10 μm. Their ability to improve an image's quality is due to the difference in acoustic impedance between their gaseous core and the surrounding medium. The impedance difference, as well as their compressibility, causes MCAs to be very echogenic, where even a single microbubble can be detected [178; 70; 179].

The nonlinear behavior of MCAs in response to ultrasound pulses allows their scattered echoes to be separable from tissue, providing a high contrast to tissue ratio. MCAs have been applied in a wide range of imaging studies including assessing myocardial perfusion [180; 181], imaging blood-perfusion in tumors [12; 182] and molecular targeting of angiogenesis or inflammation [4; 183; 184; 185].

Other applications of microbubble vehicles include acting as therapeutic delivery mediators, where microbubbles carry a gene or drug on or within their shell [26; 160; 69; 96]. Microbubbles can also be applied in conjunction with therapeutic compounds to enhance drug or gene delivery across the vascular endothelium [70].

The ability of an MCA to either enhance imaging of blood perfusion or act as therapeutic mediator is maintained only as long as it is freely circulating and intact in the bloodstream, or intentionally deposited at a localized site. Therefore, if administration is through a bolus injection, the time window for ultrasound imaging or therapeutics is integrally correlated to the *in vivo* circulation times of the microbubbles. It has been hypothesized that the short *in vivo* and *in vitro* lifetimes of MCAs are a rate-limiting step for advancing ultrasound contrast technology as quickly as other contrast imaging modalities, such as X-ray and MRI [186]. Under normal physiological conditions, an injected microbubble's lifetime is a function of both compositional and environmental variables. Studies have shown that the makeup of a bubble's lipid shell and the content of the gas core affect its lifetime [128; 187], while environmental factors such as the acoustic waveforms incident on the bubble [188], dissolved gas concentration in the blood [189; 190], and immune response [191] also play critical roles. Recent attempts to improve the composition of microbubbles include using higher molecular weight and less soluble filling gasses [187; 192], and altering the chemical composition of the microbubble's lipid shell [193; 128]. Increasing the circulation lifetimes would improve the ability to perform consistent imaging studies over time with a bolus injection, as well as improve the window in which both diagnostic and therapeutic applications can be applied.

One possible method to improve the environmental conditions for injected MCAs during studies in anesthetized animals is by changing the dissolved gas concentration of an animal's blood. It is well known that the gas saturation in the medium surrounding

the microbubble affects the gas core's dissolution rate [193; 194; 195]. Early studies with first-generation contrast agents demonstrated that MCAs circulating in dogs that inhaled different anesthesia carrier gases had different circulation times [189; 190]. These previous studies examined two albumin-shelled agents, Albunex and Optison, and observed circulation persistence for different ratios of two common selections for anesthesia carrier gas: medical air and pure oxygen. In both studies, the imaging contrast provided by these two types of MCAs was diminished by the use of pure oxygen as a carrier gas compared with the contrast provided by the same MCA type in the same animal breathing medical air as the carrier gas.

In this paper we extend these early studies from albumin shelled contrast agents to newer lipid-shelled perfluorocarbon filled contrast agents. Additionally, we examine the effects of inhaled anesthesia gas on injected MCAs in a rodent model. Rodents are commonly used as preclinical models of cancer and other diseases, and as such, are frequently selected as subjects in ultrasound contrast imaging studies. The purpose of this study was to elucidate the extent and significance of the relationship between anesthesia carrier gas composition and MCA circulation lifetime in rats.

B.2 Experimental

B.2.1 Gas Diffusion Model

To investigate whether gas diffusion could account for differences in MCA lifetime, a mathematical model previously developed by Kwan and Borden [196] was employed which predicts the size of a microbubble suddenly immersed in a multi-gas environment, such as a PFB microbubble injected into blood. This model assumes that each gas acts independently to equilibrate at the gas-liquid interface and diffuse along its own chemical potential (partial pressure) gradient. All gases contribute to the total pressure and volume of the MCA gas core. Gas diffusion occurs through a stagnant aqueous

layer equal in thickness to the microbubble radius (i.e. it is a purely diffusing sphere). Because the animal was breathing, the impact of the microbubble injection (2 μl gas) on the dissolved gas contents of the blood pool was considered negligible. A set of coupled, nonlinear differential equations results from (i) a species balance over the microbubble, (ii) the diffusion equation, (iii) the Laplace pressure equation and (iv) the ideal gas law. Applying a finite difference method, the set of equations is discretized to the following form:

$$n_i^{\tau+1} = -4\pi h R D_i K_{H,i}\left[\frac{2\sigma}{R} - P_{\infty,i} f_i + P_H - \frac{3BT}{4\pi R^3}\sum_{j=1}^{N} n_j\right] + n_i, \quad j \neq i \tag{1}$$

$$0 = \frac{8\pi\sigma}{3BT}(R^{\tau+1})^2 + \frac{4\pi P_H}{3BT}(R^{\tau+1})^3 - \sum_{i=1}^{N} n_i^{\tau+1} \tag{2}$$

where N is the total number of gas species; τ is the numerical time step; R is the microbubble radius; σ is the microbubble surface tension; P_H is the hydrostatic pressure; B is the universal gas constant; T is temperature; n_i is the moles; D_i is the diffusion coefficient; $K_{H,i}$ is Henry's constant; $P_{\infty,i}$ is the partial pressure at saturation; and f_i is the ratio of the bulk dissolved gas content to that at saturation, each of component *i*. Solving equations (1) and (2) numerically allows prediction of the growth and dissolution of a microbubble subject to the simultaneous influx and efflux of different gas species as the system tends toward thermodynamic equilibrium, which occurs when the partial pressures in the gas core and surrounding medium are equal for all species. A variable time step was used to ensure that the moles inside the microbubble did not become negative. To determine the number of moles in the bubble, a forward wind difference method was applied, as seen in equation (1), which is solved step-wise. Equation (2) is non linear and was solved using a Newton-Raphson method (100 iterations). In the simulation, 100 iterations were used in the Newton-Raphson method. Finally, it should be noted that the model is limited in that it neglects the effects of convection

in the surrounding medium, variations in blood gas concentrations and pressure as the microbubble passes through the venous-arterial circuit, and effects of the encapsulating shell, such as gas permeation resistance and viscous and elastic terms accounting for lipid monolayer expansion, break-up, compression, buckling and collapse.

B.2.2 Animal Preparation

Animals were handled according to National Institute of Health guidelines and our study protocol was approved by the UNC Institutional Animal Care and Use Committee. Five female Sprague Dawley rats (Harlan; Indianapolis, IN, USA) were imaged throughout the course of this study. Before imaging an animal, it was first anesthetized in an induction chamber by introducing an aerosolized 5% isoflurane oxygen mixture. Once sedated, the animal was removed from the induction chamber, the isoflurane concentration was reduced from 5 to 2% and then maintained via mask delivery. Its abdomen was shaved with an electric clipper and a depilating cream was applied to the animal's skin to dissolve any remaining hair that would interfere with the ultrasound image. A 24 gauge catheter was then inserted into the animal's tail vein for the administration of MCAs. The animal was placed in dorsal recumbency on a heating pad, and ultrasound coupling gel was placed between the imaging transducer and the animal's skin to ensure the quality of signal transmission.

B.2.3 Contrast Agent Preparation and Administration

A lipid mixture 1,2-distearoyl-sn-glycero-3-phosphocholine (DSPC); 1,2-distearoyl-sn-glycero-3 phosphoethanolamine-N-[methoxy- (polyethylene glycol)-2000] (ammonium salt; DSPE- PEG2K; Avanti Polar Lipids) was prepared using a 9:1 molar ratio, similar to a previously described method [128]. Briefly, lipids were dissolved in chloroform, dried and dissolved into a buffer solution of PBS. The lipid solution was then transferred into vials, which were then evacuated and filled with decafluorobutane gas. Vials

were shaken with a Vialmix shaker (Bristol-Myers Squibb Medical Imaging, North Billerica, MA, USA) for 45 s prior to injection. MCAs, of mean diameter 0.84 ± 0.34 μm, were withdrawn directly from the vial with the vial vent connected to a bag filled with decafluorobutane, to ensure that no air entered the headspace of the vial. Aliquots of 25 μl of MCAs were administered through the tail vein, followed immediately by a 200 μl flush of sterilized saline.

B.2.4 Image Acquisition

The kidneys of the rats were selected as the imaging location for this study because of their proximity to the skin's surface and the high concentration of vasculature. The clinical system used to acquire all ultrasound images in this study was an Acuson Sequoia 512 (Siemens, Mountain View, CA, USA). B-mode images were collected at 14 MHz using a linear array transducer (model 15L8). Contrast agents were imaged in CPS mode operating at 7 MHz and a mechanical index of 0.18. CPS provides a high contrast-to-tissue ratio while being minimally destructive to MCAs. Video data collection started prior to a bolus injection of MCAs, and continued for up to 20 min to allow a majority of the microbubbles to be cleared by the animal. If there were still MCAs visibly circulating in the image after 20 min, data collection was prolonged to accommodate the longer MCA persistence. Data by Killam *et al.* [197] showed that, after Optison injection into canines, the octafluoropropane was eliminated after a mean residence time of 38-46 s. As our model clearly shows, PFB rapidly dissolves from the microbubble and is replaced by the blood gases. It is therefore reasonable to assume that PFB is eliminated from the blood between contrast agent injections, which are 20 min apart.

After the completion of all measurements for an animal, the imaging study was closed and the data exported from the ultrasound system in DICOM format. These

files were later analyzed offline in MATLAB. Multiple imaging sequences were obtained of each anesthetized rat. An imaging sequence included the collection of two runs of data, one breathing oxygen and one breathing air, each beginning with an injection of MCAs and lasting until contrast agents were no longer visibly circulating. The order of carrier gas administration was randomized for all the animals. After the completion of the first run, the anesthesia carrier gas was changed and the animal was given 10 min to acclimate to this new carrier gas before initiating the second imaging sequence [190]. The imaged sequence was repeated twice more to obtain a total of three imaging sequences for each carrier gas.

B.2.5 Monitoring Physiological Changes

Blood samples were collected to determine the extent of the relationship between dissolved blood gas partial pressures of oxygen, nitrogen, carbon dioxide and anesthesia carrier gas. Arterial blood samples were obtained from the tail and tested immediately after collection in a pH/blood gas analyzer (Chiron Diagnostics, Emeryville, CA, USA). Each sample was collected only after the animal had acclimated to the anesthesia carrier gas being tested.

B.2.6 Measuring Microbubble Circulation Time

All video data were exported from the ultrasound system and imported into MATLAB for analysis. Regions of interest (ROIs) were defined around the perimeter of the kidney of each animal, and the mask applied to every frame of data. All data were examined to ensure there were no gross movements in tissue to cause inaccuracies in the ROI. The mean pixel intensity within the ROI was computed and plotted as a function of time. An example of this data is displayed in Figure B.1. To compute a pre-contrast baseline value, the mean pixel intensity of the ROI was averaged prior to the bolus injection of MCAs. After the MCAs were injected, the mean pixel intensity

rose sharply to a single peak value as the bolus entered through the ROI, then decline as the bubbles became distributed throughout the animal's body and cleared from the system. As the population of injected MCAs began to decline, the grayscale pixel intensity in the ROI also decayed steadily from the initial peak down to the original baseline value. Using MATLAB, a fourth-order interpolation polynomial was fitted to the data following the peak value in the run. Two metrics were used to quantify the circulation times of the injected MCAs: half-life and time to 25% intensity ($t_{0.5Imax}$ and $t_{0.25Imax}$ respectively). These were defined as the difference between the injection time (as determined by the highest mean intensity value in the dataset) and the times at which the data had dropped to the points either halfway to baseline ($t_{0.5Imax}$) or 75% of the way to baseline ($t_{0.25Imax}$) [191].

Measurements were repeated three times for each type of carrier gas on each animal to determine the effect of anesthesia carrier gas. These MCA circulation times for the two types of gases were compared between each animal. A paired two-sample Student's t-test was used to validate the statistical significance of the difference in circulation times of the injected MCAs between the two types of carrier gas.

B.3 Results

B.3.1 The Effect of Carrier Gas Composition on MCA Lifetime *In Vivo*

Six imaging studies were completed for each animal, with each study consisting of a single bolus injection of contrast. Circulation times, obtained from intensity curves (Fig. B.1), were compared for medical air and oxygen. A statistically significant difference ($p<0.05$) was observed for MCA circulation time as a function of anesthesia carrier gas in four out of five animals (Fig. B.2). Circulation time in the cases for which the data was not significant illustrated the same trend as in the other animals. Administering medical air as the anesthesia carrier gas caused the contrast agent half-life to be an

average of 1.8 ± 0.1 times longer than when using pure oxygen. A greater difference was observed when examining time to 25% peak intensity; the $t_{0.25Imax}$ was 2.2 ± 0.2 times longer when the animal was breathing medical air compared with breathing pure oxygen.

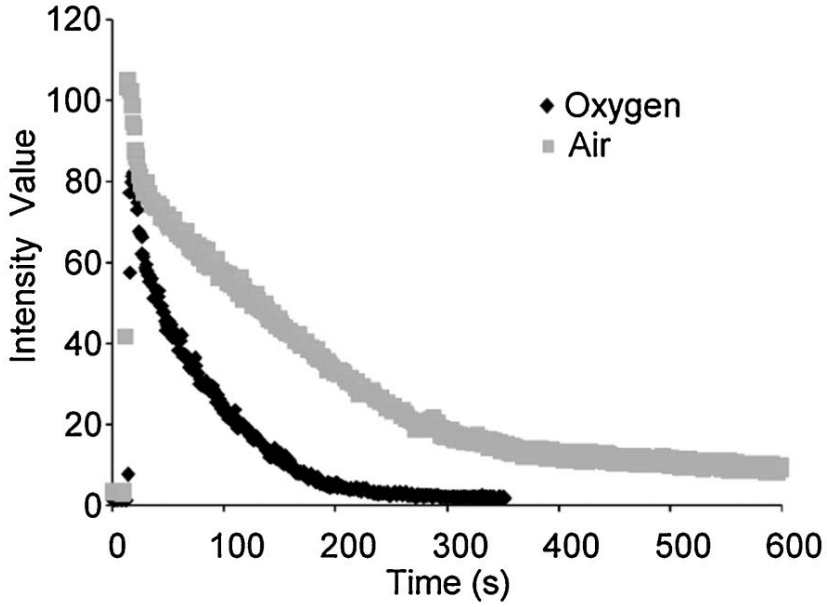

Figure B.1: A comparison of intensity curves obtained from animal 3 while breathing air compared with breathing oxygen is shown. The differences between the intensity curves is representative of results seen in all animals.

B.3.2 Relationships Between Carrier Gas and Physiology

Dissolved blood oxygen and carbon dioxide gas partial pressures were measured in four animals to observe any partial pressure differences between animals breathing pure oxygen and medical air (Fig. B.1). The largest effect of carrier gas on these variables was with pO_2, as the average value was over six times higher when breathing oxygen compared to medical air. The sum of partial pressures ($\sum p_i$) indicated a greater degree of ventilation/ perfusion mismatch for oxygen-breathing rats than for air-breathing rats, as may be expected [198; 199].

Table B.1: Mean partial pressures of dissolved O_2 and CO_2 gasses in arterial blood were measured from animals anesthetized with the two different carrier gases. The values for N_2 and H_2O were taken from literature [198; 199]. $\sum p_i$ is the sum of partial pressures. The pO_2 increased above the normal range while breathing pure oxygen, but the pCO_2 remained constant. Ventilation/perfusion mismatch increased for rats breathing pure oxygen, as expected [198; 199]. These values were used to simulate the dissolution times of a single MCA within the different mixed gas environments.

	pO_2 (mmHg)	pCO_2 (mmHg)	pN (mmHg)	pH_2O (mmHg)	$\sum p_i$ (mmHg)
Normal range	80-100	32-35	555-585	47	714-777
Breathing air (n=4)	70 ± 6	63 ± 9	560	47	740
Breathing oxygen (n=3)	546 ± 45	61 ± 15	0	47	654

One might hypothesize that the longer circulation times may be due to vasculature changes induced by the different inhaled anesthesia carrier gases. However, based on the measured blood gas values, shown in B.1, it does not appear that vascular changes are contributing to the increased MCA circulation lifetime. CO_2 partial pressure levels have been shown to be related to changes in vasculature dilation [200], but these values stayed relatively constant regardless of the administered carrier gas. Other factors that could potentially influence circulation time, such as breathing rate, heart rate and body temperature, were investigated. Preliminary studies (data not shown) showed no correlation between breathing rate, heart rate, body temperature and circulation times.

B.3.3 Simulations of MCA Circulation Time

To gain physical insight, we modeled microbubble dissolution times in blood by considering pure diffusion (no convection) of the different gas species into and out of the bubbles, as others have reported previously [201; 187]. Equations (1) and (2) were solved numerically using the Newton-Raphson method and MATLAB software (MathWorks, Natick, MA) for a 2, 5 and 10 μm diameter microbubble initially filled with pure perfluorobutane (PFB) and suddenly immersed in blood. Blood gas (O_2, N_2, H_2O

and CO_2) partial pressure values were taken from B.1 to simulate oxygen vs air as the carrier gas. The surface tension was set to 0 mN/m [194], and the hydrostatic pressure was set to 760 mmHg.

Figure B.3 shows the simulation results for the two carrier gases. Theory predicted that a 2 μm diameter microbubble survives approximately 3.2 times longer when medical air is used instead of oxygen (Fig. B.3). As the diameter was increased to 10 μm, the microbubble lifetimes were predicted to be 126 s for oxygen breathing and 409 s for air-breathing, which was in good general agreement with the experimental *in vivo* imaging data. Inspection of the microbubble contents over time provided an explanation for the extended lifetime B.4. Initially, the blood gases rapidly diffused into the microbubble just as PFB, which has a much lower solubility and diffusivity in water, slowly dissolved away. The inrush of blood gases resulted in rapid microbubble growth. Microbubble growth could not be measured acoustically here due to the complexity of the *in vivo* backscattered signal. However, microbubble growth has been predicted and measured as an increase in ultrasound attenuation in a more idealized system by Sarkar *et al.* [202; 203]. The presence of nitrogen extended the growth phase by not only adding to the volume, but also diluting the other gas species, resulting in greater accumulation of the other blood gases and reduction in the rate of PFB efflux. After a short time, the microbubble was mainly composed of blood gases, and PFB contributed only slightly to the total volume. Eventually, all gases began to efflux from the microbubble as PFB dissolution continued and the partial pressures of O_2, N_2, and CO_2 in the gas core exceeded the partial pressures in the surrounding blood. The dissolution rate was accelerated for the oxygen-carrier case owing to the greater degree of ventilation/perfusion imbalance. The sum of the partial pressures for oxygen-breathing (653 mmHg) was much lower than for air-breathing (740 mmHg). Since the ambient pressure was approximated to be 760 mmHg, the oxygen-breathing case represented a

greater deviation from equilibrium and therefore a greater driving force for microbubble dissolution. We should note that the simplified model is limited when making direct comparisons to *in vivo* contrast persistence data.

The calculation ignores the gas permeation resistance of the shell and assumes a constant surface tension (although near zero), which may not be true during the multiple regions of growth and dissolution that bubbles would experience [196]. Additionally, the calculations only take into account a single bubble under no-flow conditions. It is possible that a population of bubbles is more stable than a single bubble. The overlapping diffusion zones between neighboring microbubbles will influence their rate of dissolution, and there may be more subtle effects at play such as Ostwald ripening. These assumptions, along with activity of other clearance mechanisms like the reticuloendothelial system (RES), could account for observed circulation times being longer than the model predicts. Despite the limitations of the model, it clearly illustrates different responses due to different gases, which agrees with experimental data.

B.4 Discussion and Conclusion

A relationship between the anesthesia carrier gas and the *in vivo* lifetime of injected MCAs was observed within the five animals tested in this study. Each animal was administered three doses of MCAs under each type of carrier gas medical air and pure oxygen and the persistence of these contrast agents was monitored following injection. Half-life values and time to 25 percent intensity were calculated. Medical air was found to significantly increase the circulation time of ultrasound MCAs. The numerical results obtained using a model obeying classical Fickian diffusion with multiple gas species aligned with the experimentally measured values, suggesting that diffusion plays a key role in the reduced circulation time of injected MCAs in pure oxygen breathing animals. The effects of diffusion for the oxygen breathing case are manifest as an increased

driving force (i.e. ventilation/perfusion mismatch) and more rapid mass transfer (i.e. absence of an inert filling gas) for microbubble dissolution. This study illustrated that a simple change of an anesthesia carrier gas has the potential to improve the efficacy of ultrasound studies, both imaging and therapeutic.

B.5 Acknowledgements

We would like to acknowledge Steven Feingold, Kennita Johnson and Zhikun Liu for animal handling and technical assistance provided during the collection of experimental data in this study. James Tsuruta prepared contrast agents used in this study. This study was supported in part from The NIH Roadmap for Medical Research, R21EB005325 to P.A.D., the NYSTAR James D. Watson Investigator Award to M.A.B., and R01EB009066 to both P.A.D. and M.A.B. Pilot studies for this research appear in the proceedings of the 2009 IEEE Ultrasonics Symposium, copyright IEEE.

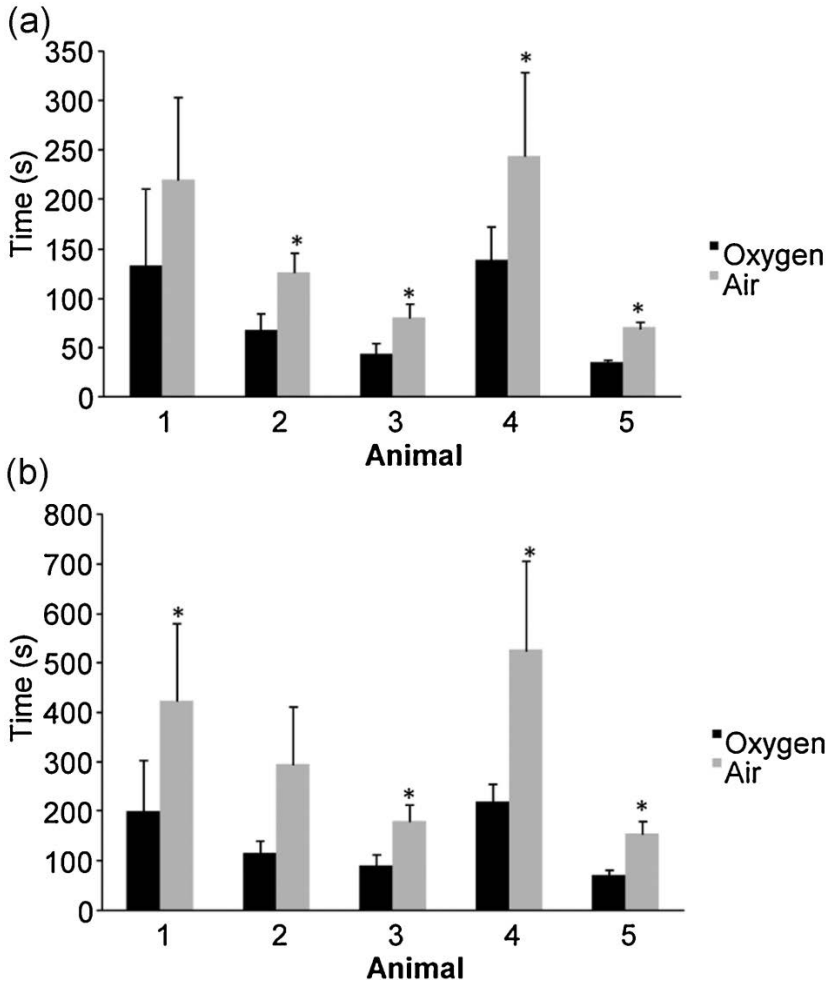

Figure B.2: Side by side comparison of the average injected MCA circulation times for each animal. (A) Average half-life and (B) average time to 25% for each animal inhaling the respective anesthesia carrier gases. The average circulation times when an animal was breathing isoflurane carried by medical air were significantly longer in most animals (*$p<0.05$).

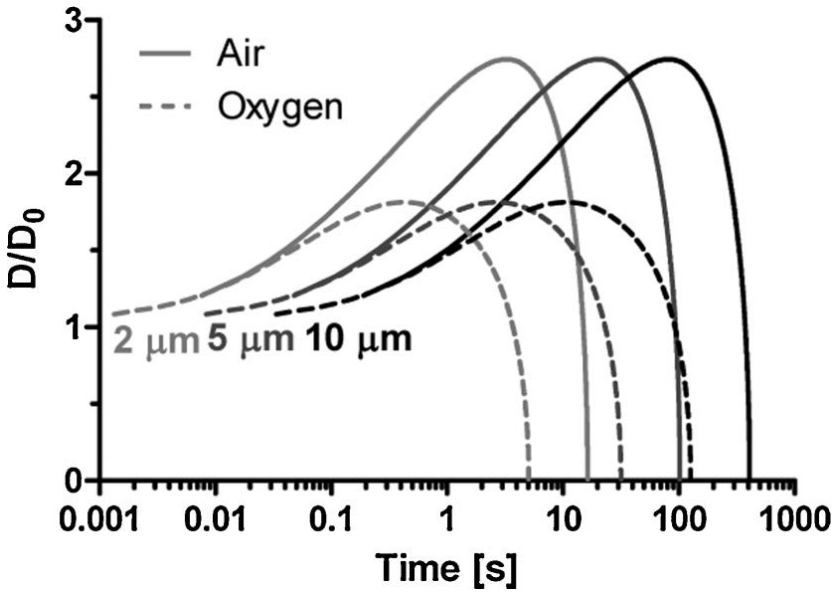

Figure B.3: Simulated response of a PFB microbubble suddenly immersed in arterial blood. The dissolved gas parameters used in these simulations, summarized in B.1, were based on measured values. Microbubble diameter was normalized by the initial value shown.

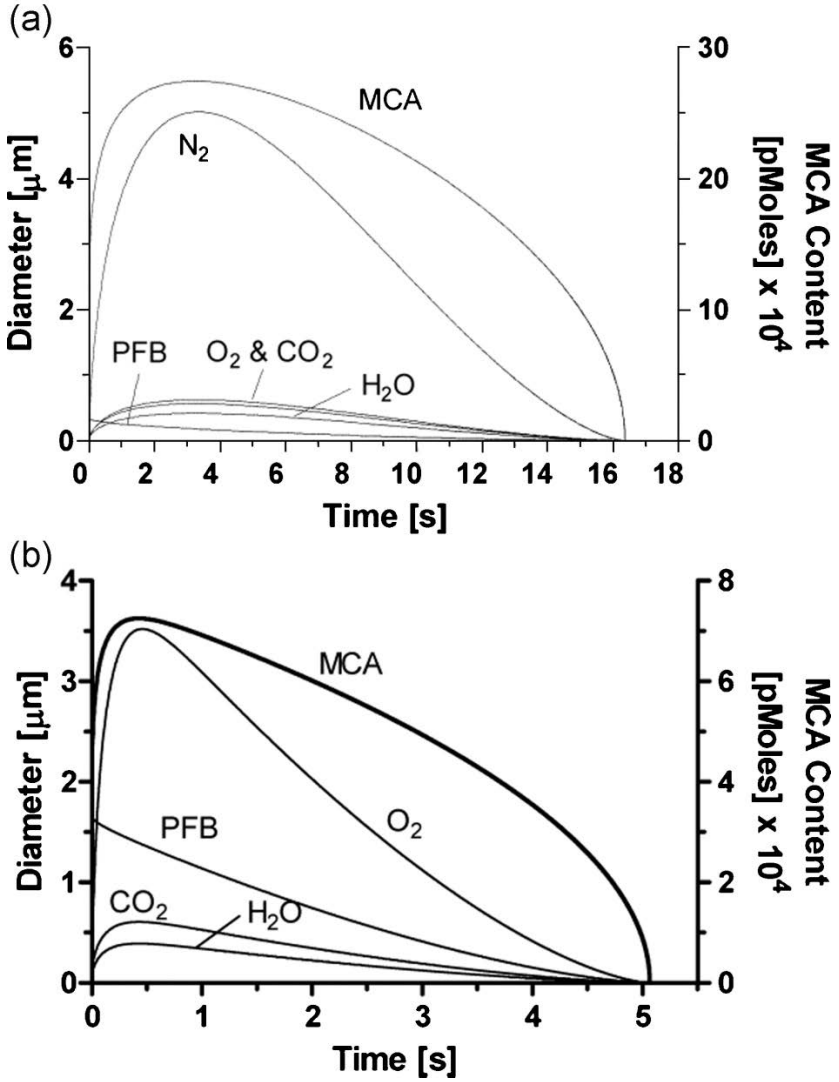

Figure B.4: Simulated response of a PFB microbubble suddenly immersed in arterial blood. The dissolved gas parameters used in these simulations, summarized in B.1, were based on measured values. Molar contents of each gas are plotted vs time for (A) medical air and (B) oxygen as the carrier gas.

BIBLIOGRAPHY

[1] K. Ferrara, M. Borden, and H. Zhang, "Lipid-shelled vehicles: Engineering for ultrasound molecular imaging and drug delivery," *Accounts of Chemical Research*, vol. 42, no. 7, pp. 881–892, 2009.

[2] C. Mayer, N. Geis, H. Katus, and R. Bekeredjian, "Ultrasound targeted microbubble destruction for drug and gene delivery," *Expert Opinion On Drug Delivery*, vol. 5, no. 10, pp. 1121–1138, 2008.

[3] S. Tinkov, R. Bekeredjian, G. Winter, and C. Coester, "Microbubbles as ultrasound triggered drug carriers," *Journal of Pharmaceutical Sciences*, vol. 98, no. 6, pp. 1935–1961, 2009.

[4] P. Dayton and J. Rychak, "Molecular ultrasound imaging using microbubble contrast agents," *Frontiers in Bioscience*, vol. 12, pp. 5124–5142, 2007.

[5] I. Lentacker, S. De Smedt, and N. Sanders, "Drug loaded microbubble design for ultrasound triggered delivery," *Soft Matter*, vol. 5, no. 11, pp. 2161–2170, 2009.

[6] S. Sirsi and M. Borden, "Microbubble compositions, properties and biomedical applications," *Bubble Science Engineering and Technology*, vol. 1, no. 1-2, pp. 3–17, 2009.

[7] K. Wei, A. Jayaweera, S. Firoozan, A. Linka, D. Skyba, and S. Kaul, "Quantification of myocardial blood flow with ultrasound-induced destruction of microbubbles administered as a constant venous infusion," *Circulation*, vol. 97, no. 5, pp. 473–483, 1998.

[8] M. Blomley, J. Cooke, E. Unger, M. Monaghan, and D. Cosgrove, "Microbubble contrast agents: A new era in ultrasound," *BMJ*, vol. 322, no. 7296, pp. 1222–1225, 2001.

[9] S. Feinstein, J. Cheirif, F. Ten Cate, P. Silverman, P. Heidenreich, C. Dick, R. Desir, W. Armstrong, M. Quinones, and P. Shah, "Safety and efficacy of a new transpulmonary ultrasound contrast agent: Initial multicenter clinical results," *Journal of the American College of Cardiology*, no. 2, pp. 316–324, 1990.

[10] B. Goldberg, J. Liu, and F. Forsberg, "Ultrasound contrast agents: A review," *Ultrasound in Medicine and Biology*, vol. 20, no. 4, pp. 319–333, 1994.

[11] F. Foster, P. Burns, D. Simpson, S. Wilson, D. Christopher, and D. Goertz, "Ultrasound for the visualization and quantification of tumor microcirculation," *Cancer and Metastasis Reviews*, vol. 19, no. 1-2, pp. 131–138, 2000.

[12] J. Chomas, R. Pollard, A. Sadlowski, S. Griffey, E. Wisner, and K. Ferrara, "Contrast-enhanced us of microcirculation of superficially implanted tumors in rats," *Radiology*, vol. 229, no. 2, pp. 439–446, 2003.

[13] P. Burns, S. Wilson, and D. Simpson, "Pulse inversion imaging of liver blood flow: Improved method for characterizing focal masses with microbubble contrast," *Investigative Radiology*, vol. 35, no. 1, pp. 58–71, 2000.

[14] K. Wei, E. Le, J. Bin, M. Coggins, J. Thorpe, and S. Kaul, "Quantification of renal blood flow with contrast-enhanced ultrasound," *Journal of the American College of Cardiology*, vol. 37, no. 4, pp. 1135–1140, 2001.

[15] H. Leong-Poi, J. Christiansen, A. Klibanov, S. Kaul, and J. Lindner, "Noninvasive assessment of angiogenesis by ultrasound and microbubbles targeted to v-integrins," *Circulation*, vol. 107, no. 3, pp. 455–460, 2003.

[16] D. Ellegala, H. Leong-Poi, J. Carpenter, A. Klibanov, S. Kaul, M. Shaffrey, J. Sklenar, and J. Lindner, "Imaging tumor angiogenesis with contrast ultrasound and microbubbles targeted to $\alpha_v\beta_3$," *Circulation*, vol. 108, no. 3, pp. 336–341, 2003.

[17] J. Lindner, J. Song, F. Xu, A. Klibanov, K. Singbartl, K. Ley, and S. Kaul, "Noninvasive ultrasound imaging of inflammation using microbubbles targeted to activated leukocytes," *Circulation*, vol. 102, no. 22, pp. 2745–2750, 2000.

[18] J. Lindner, P. Dayton, M. Coggins, K. Ley, J. Song, K. Ferrara, and S. Kaul, "Noninvasive imaging of inflammation by ultrasound detection of phagocytosed microbubbles," *Circulation*, vol. 102, no. 5, pp. 531–538, 2000.

[19] J. Lindner, "Contrast ultrasound molecular imaging of inflammation in cardiovascular disease," *Cardiovascular Research*, vol. 84, no. 2, pp. 182–189, 2009.

[20] R. Gramiak and P. Shah, "Echocardiography of the aortic root," *Investigative Radiology*, vol. 3, no. 5, pp. 356–366, 1968.

[21] P. Dayton, J. Allen, and K. Ferrara, "The magnitude of radiation force on ultrasound contrast agents," *Journal of the Acoustical Society of America*, vol. 112, no. 5, pp. 2183–2192, 2002.

[22] P. Dayton, K. Morgan, A. Klibanov, G. Brandenburger, K. Nightingale, and K. Ferrara, "A preliminary evaluation of the effects of primary and secondary radiation forces on acoustic contrast agents," *IEEE Transactions on Ultrasonics Ferroelectrics and Frequency Control*, vol. 44, no. 6, pp. 1264–1277, 1997.

[23] P. Dayton, A. Klibanov, G. Brandenburger, and K. Ferrara, "Acoustic radiation force *in vivo*: A mechanism to assist targeting of microbubbles," *Ultrasound in Medicine and Biology*, vol. 25, no. 8, pp. 1195–1201, 1999.

[24] J. Streeter, R. Gessner, I. Miles, and P. Dayton, "Improving sensitivity in ultrasound molecular imaging by tailoring contrast agent size distribution: *In vivo* studies," *Molecular Imaging*, vol. 9, no. 2, pp. 87–95, 2010.

[25] J. Streeter, R. Gessner, J. Tsuruta, S. Feingold, and P. Dayton, "Assessment of molecular imaging of angiogenesis with three-dimensional ultrasonography," *Molecular Imaging*, vol. 10, no. 6, pp. 460–468, 2011.

[26] K. Ferrara, R. Pollard, and M. Borden, "Ultrasound microbubble contrast agents: Fundamentals and application to gene and drug delivery," *Annual Review of Biomedical Engineering*, vol. 9, pp. 415–447, 2007.

[27] M. Palmeri and N. KR, "Acoustic radiation force-based elasticity imaging methods," *Interface Focus*, vol. 1, no. 4, pp. 553–564, 2011.

[28] J. Rychak, A. Klibanov, and J. Hossack, "Acoustic radiation force enhances targeted delivery of ultrasound contrast microbubbles: *In vitro* verification," *IEEE Transactions on Ultrasonics, Ferroelectrics and Frequency Control*, vol. 52, no. 3, pp. 421–433, 2005.

[29] J. Rychak, A. Klibanov, K. Ley, and J. Hossack, "Enhanced targeting of ultrasound contrast agents using acoustic radiation force," *Ultrasound in Medicine and Biology*, vol. 33, no. 7, pp. 1132–1139, 2007.

[30] R. Siegel, D. Naishadham, and A. Jemal, "Cancer statistics, 2013," *CA A Cancer Journal for Clinicians*, vol. 63, pp. 11–30, 2013.

[31] M. Chidambaram, R. Manavalan, and K. Kathiresan, "Nanotherapeutics to overcome conventional cancer chemotherapy limitations," *Journal of Pharmaceutical and Pharmaceutical Sciences*, vol. 14, no. 1, pp. 67–77, 2011.

[32] R. Love, H. Leventhal, D. Easterling, and D. Nerenz, "Side effects and emotional distress during cancer chemotherapy," *Cancer*, no. 3, p. 604612, 1989.

[33] E. Ballatori and A. Roila, "Impact of nausea and vomiting on quality of life in cancer patients during chemotherapy," *Health and Quality of Life Outcomes*, vol. 11, pp. 1–11, 2003.

[34] P. Ma and M. RJ, "Paclitaxel nano-delivery systems: A comprehensive review," *Journal of Nanomedicine and Nanotechnology*, vol. 4, no. 2, p. 1000164, 2013.

[35] M. Jordan and L. Wilson, "Microtubules as a target for anticancer drugs," *Nature Reviews Cancer*, vol. 4, no. 4, pp. 253–65, 2004.

[36] Y. Barenholz, "Doxil–the first fda-approved nano-drug: Lessons learned," *Journal of Controlled Release*, vol. 160, no. 2, pp. 117–134, 2012.

[37] V. Torchilin, "Targeted pharmaceutical nanocarriers for cancer therapy and imaging," *The AAPS Journal*, vol. 9, no. 2, pp. E128–E147, 2007.

[38] D. Fukumura, D. Duda, L. Munn, and R. Jain, "Tumor microvasculature and microenvironment: Novel insights through intravital imaging in pre-clinical models," *Microcirculation*, vol. 17, no. 3, pp. 206–225, 2010.

[39] D. Ribatti and A. Vacca, "Overview of angiogenesis during tumor growth," in *Angiogenesis* (W. Figg and J. Folkman, eds.), pp. 161–168, Springer US, 2008.

[40] J. Folkman, "Fundamental concepts of the angiogenic process," *Current Molecular Medicine*, vol. 3, no. 7, pp. 643–651, 2003.

[41] P. Carmeliet and R. Jain, "Angiogenesis in cancer and other diseases," *Nature*, vol. 407, no. 6801, pp. 249–257, 2000.

[42] R. Kerbel, "Tumor angiogenesis," *New England Journal of Medicine*, vol. 358, no. 19, pp. 2039–2049, 2008.

[43] G. Bergers and L. Benjamin, "Tumorigenesis and the angiogenic switch," *Nature Reviews Cancer*, vol. 3, no. 6, pp. 401–410, 2003.

[44] D. McDonald, "Angiogenesis and vascular remodeling in inflammation and cancer: Biology and architecture of the vasculature," in *Angiogenesis* (W. Figg and J. Folkman, eds.), pp. 17–33, Springer US, 2008.

[45] Y. Matsumura and H. Maeda, "A new concept for macromolecular therapeutics in cancer-chemotherapy - mechanism of tumoritropic accumulation of proteins and the antitumor agent smancs," *Cancer Research*, vol. 46, no. 12, pp. 6387–6392, 1986.

[46] H. Maeda, "Vascular permeability in cancer and infection as related to macromolecular drug delivery, with emphasis on the epr effect for tumor-selective drug targeting," *Proceedings of the Japan Academy Series B-Physical and Biological Sciences*, vol. 88, no. 3, pp. 53–71, 2012.

[47] B. Haley and E. Frenkel, "Nanoparticles for drug delivery in cancer treatment," *Urologic Oncology*, vol. 26, no. 1, pp. 57–64, 2008.

[48] F. Danhier, O. Feron, and V. Prat, "To exploit the tumor microenvironment: Passive and active tumor targeting of nanocarriers for anti-cancer drug delivery," *Journal of Controlled Release*, vol. 148, no. 2, pp. 135–146, 2010.

[49] W. Zamboni, V. Torchilin, A. Patri, J. Hrkach, S. Stern, R. Lee, A. Nel, N. Panaro, and P. Grodzinski, "Best practices in cancer nanotechnology: Perspective from nci nanotechnology alliance," *Clinical Cancer Research*, vol. 18, no. 12, pp. 3229–3241, 2012.

[50] F. Perche and V. Tochilin, "Recent trends in multifunctional liposomal nanocarriers for enhanced tumor targeting," *Journal of Drug Delivery*, 2013.

[51] S. Taruin, K. Nehoff, and K. Greish, "Anticancer nanomedicine and tumor vascular permeability; where is the missing link?," *Journal of Conrolled Release*, vol. 164, no. 3, pp. 265–275, 2012.

[52] T. Lammers, F. Kiessling, W. Hennink, and G. Storm, "Drug targeting to tumors: Principles, pitfalls and (pre-) clinical progress," *Journal of Controlled Release*, vol. 161, no. 2, pp. 175–187, 2012.

[53] C.-Y. Lin, T.-M. Liu, C.-Y. Chen, Y.-L. Huang, W.-K. Huang, C.-K. Sun, F.-H. Chang, and W.-L. Lin, "Quantitative and qualitative investigation into the impact of focused ultrasound with microbubbles on the triggered release of nanoparticles from vasculature in mouse tumors," *Journal of Controlled Release*, vol. 146, no. 3, pp. 291–298, 2010.

[54] A. Kheirolomoom, P. Dayton, A. Lum, E. Little, E. Paoli, H. Zheng, and K. Ferrara, "Acoustically-active microbubbles conjugated to liposomes: Characterization of a proposed drug delivery vehicle," *Journal of Controlled Release*, vol. 118, no. 3, pp. 275–284, 2007.

[55] E. Unger, T. McCreery, and R. Sweitzer, "Ultrasound enhances gene expression of liposomal transfection," *Investigative Radiology*, vol. 32, no. 12, pp. 723–727, 1997.

[56] B. Geers, I. Lentacker, N. Sanders, J. Demeester, S. Meairs, and S. De Smedt, "Self-assembled liposome-loaded microbubbles: The missing link for safe and efficient ultrasound triggered drug-delivery," *Journal of Controlled Release*, no. 2, pp. 249–256, 2011.

[57] A. Klibanov, T. Shevchenko, B. Raju, R. Seip, and C. Chin, "Ultrasound-triggered release of materials entrapped in microbubble-liposome constructs: A tool for targeted drug delivery," *Journal of Controlled Release*, vol. 148, no. 1, pp. 13–17, 2010.

[58] C. Burke, Y. Hsiang, E. Alexander, A. Kilbanov, and R. Price, "Covalently linking poly(lactic-co-glycolic acid) nanoparticles to microbubbles before intravenous injection improves their ultrasound-targeted delivery to skeletal muscle," *Small*, vol. 2011, no. 1, pp. 1227–1235, 2010.

[59] J. Du, Q. Shi, Y. Sun, P. Liu, M. Zhu, L. Du, and Y. Duan, "Enhanced delivery of monomethoxypoly(ethylene glycol)-poly(lactic-co-glycolic acid)-poly l-lysine nanoparticles loading platelet-derived growth factor bb small interfering RNA by ultrasound and/or microbubbles to rat retinal pigment epithelium cells," *The Journal of Gene Medicine*, vol. 13, no. 6, pp. 312–323, 2011.

[60] I. Lentacker, R. Vandenbroucke, B. Lucas, J. Demeester, S. De Smedt, and N. Sanders, "New strategies for nucleic acid delivery to conquer cellular and nuclear membranes," *Journal of Controlled Release*, vol. 132, no. 3, pp. 279–288, 2008.

[61] I. Lentacker, N. Wang, R. Vandenbroucke, J. Demeester, S. De Smedt, and N. Sander, "Ultrasound exposure of lipoplex loaded microbubbles facilitates direct cytoplasmic entry of the lipoplexes," *Molecular Pharmaceutics*, vol. 6, no. 2, pp. 457–467, 2009.

[62] M.-L. De Temmerman, H. Dewitte, R. Vandenbroucke, B. Lucas, C. Libert, J. Demeester, S. De Smedt, I. Lentacker, and J. Rejman, "mRNA-lipoplex loaded microbubble contrast agents for ultrasound-assisted transfection of dendritic cells," *Biomaterials*, no. 34, pp. 1–8, 2011.

[63] H. Hancock, L. Smith, J. Cuesta, A. Durrani, M. Angstadt, M. Palmeri, E. Kimmel, and V. Frenkel, "Investigations into pulsed high-intensity focused ultrasoundenhanced delivery: Preliminary evidence for a novel mechanism," *Ultrasound in Medicine and Biology*, vol. 35, no. 10, pp. 1722–1736, 2009.

[64] A. van Wamel, K. Kooiman, M. Harteveld, M. Emmer, F. ten Cate, M. Versluis, and N. de Jong, "Vibrating microbubbles poking individual cells: Drug transfer into cells via sonoporation," *Journal of Controlled Release*, vol. 112, no. 2, pp. 149–155, 2006.

[65] B. Meijering, L. Juffermans, A. van Wamel, R. Henning, I. Zuhorn, M. Emmer, A. Versteilen, W. Paulus, W. van Gilst, K. Kooiman, N. de Jong, R. Musters, L. Deelman, and O. Kamp, "Ultrasound and microbubble-targeted delivery of macromolecules is regulated by induction of endocytosis and pore formation," *Circulation Research*, vol. 104, no. 5, pp. 679–U226, 2009.

[66] K. Kooiman, M. Emmer, M. Foppen-Harteveld, A. van Wamel, and N. de Jong, "Increasing the endothelial layer permeability through ultrasound-activated microbubbles," *IEEE Transactions on Biomedical Engineering*, vol. 57, no. 1, pp. 29–32, 2010.

[67] J. Wu, J. Ross, and J. Chiu, "Reparable sonoporation generated by microstreaming," *Journal of the Acoustical Society of America*, vol. 111, no. 3, pp. 1460–1464, 2002.

[68] J. Collis, R. Manasseh, P. Liovic, P. Tho, A. Ooi, K. Petkovic-Duran, and Y. Zhu, "Cavitation microstreaming and stress fields created by microbubbles," *Ultrasonics*, vol. 50, no. 2, pp. 273–279, 2010.

[69] M. Postema and O. Gilja, "Ultrasound-directed drug delivery," *Current Pharmaceutical Biotechnology*, vol. 8, no. 6, pp. 355–361, 2007.

[70] V. Sboros, "Response of contrast agents to ultrasound," *Advanced Drug Delivery Reviews*, vol. 60, no. 10, pp. 1117–1136, 2008.

[71] M. Postema, A. Van Wamel, C. Lancee, and N. De Jong, "Ultrasound-induced encapsulated microbubble phenomena," *Ultrasound in Medicine and Biology*, vol. 30, no. 6, pp. 827–840, 2004.

[72] A. Yudina, M. Lepetit-Coiffe, and C. Moonen, "Evaluation of the temporal window for drug delivery following ultrasound-mediated membrane permeability enhancement," *Molecular Imaging and Biology*, vol. 13, no. 2, pp. 239–249, 2011.

[73] R. Karshafian, P. Bevan, R. Williams, S. Samac, and P. Burns, "Sonoporation by ultrasound-activated microbubble contrast agents: Effect of acoustic exposure parameters on cell membrane permeability and cell viability," *Ultrasound in Medicine and Biology*, vol. 35, no. 5, pp. 847–860, 2009.

[74] C. Deng, F. Sieling, H. Pan, and J. Cui, "Ultrasound-induced cell membrane porosity," *Ultrasound in Medicine and Biology*, vol. 30, no. 4, pp. 519–526, 2004.

[75] H. Guzman, D. Nguyen, S. Khan, and M. Prausnitz, "Ultrasound-mediated disruption of cell membranes. I. Quantification of molecular uptake and cell viability," *Journal of the Acoustical Society of America*, vol. 110, no. 1, pp. 588–596, 2001.

[76] M. Duvshani-Eshet, L. Baruch, E. Kesselman, E. Shimoni, and M. Machluf, "Therapeutic ultrasound-mediated DNA to cell and nucleus: Bioeffects revealed by confocal and atomic force microscopy," *Gene Therapy*, vol. 13, no. 2, pp. 163–172, 2005.

[77] D. Miller, C. Dou, and J. Song, "DNA transfer and cell killing in epidermoid cells by diagnostic ultrasound activation of contrast agent gas bodies *in vitro*," *Ultrasound in Medicine and Biology*, vol. 29, no. 4, pp. 601–607, 2003.

[78] Z. Fan, R. Kumon, J. Park, and C. Deng, "Intracellular delivery and calcium transients generated in sonoporation facilitated by microbubbles," *Journal of Controlled Release*, vol. 142, no. 1, pp. 31–39, 2010.

[79] F. Yang, M. Zhang, W. He, P. Chen, X. Cai, L. Yang, N. Gu, and J. Wu, "Controlled release of Fe3O4 nanoparticles in encapsulated microbubbles to tumor cells via sonoporation and associated cellular bioeffects," *Small*, vol. 7, no. 7, pp. 902–910, 2011.

[80] L. Juffermans, A. van Dijk, C. Jongenelen, B. Drukarch, A. Reijerkerk, H. de Vries, O. Kamp, and R. Musters, "Ultrasound and microbubble-induced intra- and intercellular bioeffects in primary endothelial cells," *Ultrasound in Medicine and Biology*, vol. 35, no. 11, pp. 1917–1927, 2009.

[81] N. Sheikov, N. McDannold, N. Vykhodtseva, F. Jolesz, and K. Hynynen, "Cellular mechanisms of the blood-brain barrier opening induced by ultrasound in presence of microbubbles," *Ultrasound in Medicine and Biology*, vol. 30, no. 7, pp. 979–989, 2004.

[82] J. Choi, M. Pernot, T. Brown, S. Small, and E. Konofagou, "Spatio-temporal analysis of molecular delivery through the blood-brain barrier using focused ultrasound," *Physics in Medicine and Biology*, vol. 52, no. 18, pp. 5509–5530, 2007.

[83] J. Choi, J. Feshitan, B. Baseri, S. Wang, Y. Tung, M. Borden, and E. Konofagou, "Microbubble-size dependence of focused ultrasound-induced blood-brain barrier opening in mice *in vivo*," *IEEE Transactions on Biomedical Engineering*, vol. 57, no. 1, pp. 145–154, 2010.

[84] N. McDannold, N. Vykhodtseva, and K. Hynynen, "Targeted disruption of the blood-brain barrier with focused ultrasound: Association with cavitation activity," *Physics in Medicine and Biology*, vol. 51, no. 4, pp. 793–807, 2006.

[85] R. Bekeredjian, R. Kroll, S. Fein, Eand Tinkov, C. Coester, G. Winter, H. A. Katus, and H. Kulaksiz, "Ultrasound targeted microbubble destruction increases capillary permeability in hepatomas," *Ultrasound in Medicine and Biology*, vol. 33, no. 10, pp. 1592–1598, 2007.

[86] R. Price, D. Skyba, S. Kaul, and T. Skalak, "Delivery of colloidal particles and red blood cells to tissue through microvessel ruptures created by targeted microbubble destruction with ultrasound," *Circulation*, vol. 98, no. 13, pp. 1264–1267, 1998.

[87] D. Vancraeynest, X. Havaux, A. Pouleur, A. Pasquet, B. Gerber, C. Beauloye, P. Rafter, L. Bertrand, and V. JL, "Myocardial delivery of colloid nanoparticles using ultrasound-targeted microbubble destruction," *European Heart Journal*, vol. 27, no. 2, pp. 237–245, 2006.

[88] S. Stieger, C. Caskey, R. Adamson, S. Qin, F.-R. Curry, E. Wisner, and K. Ferrara, "Enhancement of vascular permeability with low-frequency contrast-enhanced ultrasound in the chorioallantoic membrane model," *Radiology*, vol. 243, no. 1, pp. 112–121, 2007.

[89] D. Skyba, R. Price, A. Linka, T. Skalak, and S. Kaul, "Direct *in vivo* visualization of intravascular destruction of microbubbles by ultrasound and its local effects on tissue," *Circulation*, vol. 98, no. 4, pp. 290–293, 1998.

[90] C. Caskey, S. Stieger, S. Qin, P. Dayton, and K. Ferrara, "Direct observations of ultrasound microbubble contrast agent interaction with the microvessel wall," *Journal of the Acoustical Society of America*, vol. 122, no. 2, pp. 1191–1200, 2007.

[91] H. Chen, A. Brayman, M. Bailey, and T. Matula, "Blood vessel rupture by cavitation," *Urological Research*, no. 4, pp. 1–6, 2010.

[92] H. Chen, A. Brayman, W. Kreider, M. Bailey, and T. Matula, "Observations of translation and jetting of ultrasound-activated microbubbles in mesenteric microvessels," *Ultrasound in Medicine and Biology*, vol. 37, no. 12, pp. 2139–2148, 2011.

[93] H. Chen, W. Kreider, A. Brayman, M. Bailey, and T. Matula, "Blood vessel deformations on microsecond time scales by ultrasonic cavitation," *Physical Review Letters*, vol. 106, no. 3, p. 34301, 2011.

[94] P. Dayton, S. Zhao, S. Bloch, P. Schumann, K. Penrose, T. Matsunaga, R. Zutshi, A. Doinikov, and K. Ferrara, "Application of ultrasound to selectively localize nanodroplets for targeted imaging and therapy," *Molecular Imaging*, vol. 5, no. 3, p. 160, 2006.

[95] A. Lum, M. Borden, P. Dayton, D. Kruse, S. Simon, and K. Ferrara, "Ultrasound radiation force enables targeted deposition of model drug carriers loaded on microbubbles," *Journal of Controlled Release*, vol. 111, no. 1-2, pp. 128–134, 2006.

[96] M. Shortencarier, P. Dayton, S. Bloch, P. Schumann, T. Matsunaga, and K. Ferrara, "A method for radiation-force localized drug delivery using gas-filled lipospheres," *IEEE Transactions on Ultrasonics Ferroelectrics and Frequency Control*, vol. 51, no. 7, pp. 822–831, 2004.

[97] S. Bloch, P. Dayton, and K. Ferrara, "Targeted imaging using ultrasound contrast agents. progress and opportunities for clinical and research applications," *IEEE Engineering in Medicine and Biology Magazine*, vol. 23, no. 5, pp. 18–29, 2004.

[98] C.-Y. Lin, Y.-L. Huang, J.-R. Li, F.-H. Chang, and W.-L. Lin, "Effects of focused ultrasound and microbubbles on the vascular permeability of nanoparticles delivered into mouse tumors," *Ultrasound in Medicine and Biology*, vol. 36, no. 9, pp. 1460–1469, 2010.

[99] E. Bayer and M. Wilchek, "The use of the avidin-biotin complex as a tool in molecular biology," *Methods of Biochemical Analysis*, vol. 26, pp. 1–45, 1980.

[100] M. Lozano, C. Starkel, and M. Longo, "Vesicles tethered to microbubbles by hybridized DNA oligonucleotides: Flow cytometry analysis of this new drug delivery vehicle design," *Langmuir*, vol. 26, no. 11, pp. 8517–8524, 2010.

[101] M. Seo, I. Gorelikov, R. Williams, and N. Matsuura, "Microfluidic assembly of monodisperse, nanoparticle-incorporated perfluorocarbon microbubbles for medical imaging and therapy," *Langmuir*, vol. 26, no. 17, pp. 13855–13860, 2010.

[102] M. Cochran, J. Eisenbrey, R. Ouma, M. Soulen, and M. Wheatley, "Doxorubicin and paclitaxel loaded microbubbles for ultrasound triggered drug delivery," *International Journal of Pharmaceutics*, vol. 414, no. 1-2, pp. 161–170, 2011.

[103] J. Eisenbrey, O. Burstein, R. Kambhampati, F. Forsberg, J. Liu, and M. Wheatley, "Development and optimization of a doxorubicin loaded poly(lactic acid) contrast agent for ultrasound directed drug delivery," *Journal of Controlled Release*, vol. 143, no. 1, pp. 38–44, 2010.

[104] J. Eisenbrey, M. Soulen, and M. Wheatley, "Delivery of encapsulated doxorubicin by ultrasound-mediated size reduction of drug-loaded polymer contrast agents," *IEEE Transactions on Biomedical Engineering*, vol. 57, no. 1, pp. 24–28, 2010.

[105] Z. Liu, T. Lammers, J. Ehling, S. Fokong, J. Bornemann, F. Kiessling, and J. Gtjens, "Iron oxide nanoparticle-containing microbubble composites as contrast agents for MR and ultrasound dual-modality imaging," *Biomaterials*, vol. 32, no. 26, pp. 6155–6163, 2011.

[106] J. Park, D. Jagadeesan, R. Williams, W. Oakden, S. Chung, G. Stanisz, and E. Kumacheva, "Microbubbles loaded with nanoparticles: A route to multiple imaging modalities," *ACS Nano*, vol. 4, no. 11, pp. 6579–6586, 2010.

[107] H. Ke, Z. Xing, B. Zhao, J. Wang, J. Liu, C. Guo, X. Yue, S. Liu, Z. Tang, and Z. Dai, "Quantum-dot-modified microbubbles with bi-mode imaging capabilities," *Nanotechnology*, vol. 20, no. 42, pp. 425105–425105, 2009.

[108] R. Seip, C. Chin, C. Hall, B. Raju, A. Ghanem, and K. Tiemann, "Targeted ultrasound-mediated delivery of nanoparticles: On the development of a new hifu-based therapy and imaging device," *IEEE Transactions on Biomedical Engineering*, vol. 57, no. 1, pp. 61–70, 2010.

[109] X. Hu, H. Zheng, D. Kruse, P. Sutcliffe, D. Stephens, and K. Ferrara, "A sensitive tlrh targeted imaging technique for ultrasonic molecular imaging," *IEEE Transactions on Ultrasonics, Ferroelectrics and Frequency Control*, vol. 57, no. 2, pp. 305–316, 2010.

[110] J. Song, J. Chappell, M. Qi, E. VanGieson, S. Kaul, and R. Price, "Influence of injection site, microvascular pressure and ultrasound variables on microbubble-mediated delivery of microspheres to muscle," *Journal of the American College of Cardiology*, vol. 39, no. 4, pp. 726–731, 2002.

[111] J. Chappell, J. Song, C. Burke, A. Klibanov, and R. Price, "Targeted delivery of nanoparticles bearing fibroblast growth factor-2 by ultrasonic microbubble destruction for therapeutic arteriogenesis," *Small*, vol. 4, no. 10, pp. 1769–1777, 2008.

[112] I. Lentacker, S. De Smedt, J. Demeester, V. Van Marck, M. Bracke, and N. Sanders, "Lipoplex-loaded microbubbles for gene delivery: A trojan horse controlled by ultrasound," *Advanced Functional Materials*, vol. 17, no. 12, pp. 1910–1916, 2007.

[113] R. Vandenbroucke, J. Lentacker, Iand Demeester, S. De Smedt, and N. Sanders, "Ultrasound assisted siRNA delivery using PEG-siPlex loaded microbubbles," *Journal of Controlled Release*, vol. 126, no. 3, pp. 265–273, 2008.

[114] I. Lentacker, B. Geers, J. Demeester, S. De Smedt, and N. Sanders, "Design and evaluation of doxorubicin-containing microbubbles for ultrasound-triggered doxorubicin delivery: Cytotoxicity and mechanisms involved," *Molecular Therapy*, vol. 18, no. 1, pp. 101–108, 2009.

[115] C.-Y. Lin, J.-R. Li, H.-C. Tseng, M.-F. Wu, and W.-L. Lin, "Enhancement of focused ultrasound with microbubbles on the treatments of anticancer nanodrug in mouse tumors," *Nanomedicine Nanotechnology Biology and Medicine*, pp. 1–8, 2011.

[116] M. Cochran, J. Eisenbrey, M. Soulen, S. Schultz, R. Ouma, S. White, E. Furth, and M. Wheatley, "Disposition of ultrasound sensitive polymeric drug carrier in a rat hepatocellular carcinoma model," *Academic Radiology*, vol. 18, no. 11, pp. 1341–1348, 2011.

[117] T. Rthel, H. Mannell, J. Pircher, B. Gleich, U. Pohl, and F. Krtz, "Magnetic stents retain nanoparticle-bound antirestenotic drugs transported by lipid microbubbles," *Pharmaceutical Research*, no. 5, pp. 1295–1307, 2012.

[118] I. Lentacker, I. De Cock, R. Deckers, S. De Smedt, and C. Moonen, "Understanding ultrasound induced sonoporation: Definitions and underlying mechanisms," *Advanced Drug Delivery Reviews*, in press.

[119] Z. Fan, H. Liu, M. Mayer, and C. Deng, "Spatiotemporally controlled single cell sonoporation," *Proceedings of the National Academy of Sciences of the United States of America*, vol. 109, no. 41, pp. 16486–16491, 2012.

[120] S. Sonoda, K. Tachibana, E. Uchino, A. Okubo, M. Yamamoto, K. Sakoda, T. Hisatomi, K. Sonoda, Y. Negishi, Y. Izumi, S. Takao, and T. Sakamoto, "Gene transfer to corneal epithelium and keratocytes mediated by ultrasound with microbubbles," *Investigative Ophthalmology and Visual Science*, vol. 47, no. 2, pp. 558–564, 2006.

[121] C. Burke, A. Klibanov, J. Sheehan, and R. Price, "Inhibition of glioma growth by microbubble activation in a subcutaneous model using low duty cycle ultrasound without significant heating," *Journal of Neurosurgery*, vol. 114, no. 6, pp. 1654–1661, 2011.

[122] H. Pan, Y. Zhou, O. Izadnegahdar, J. Cui, and C. Deng, "Study of sonoporation dynamics affected by ultrasound duty cycle," *Ultrasound in Medicine and Biology*, vol. 31, no. 6, pp. 849–856, 2005.

[123] M. Forbes, R. Steinberg, and W. O'Brien, "Frequency-dependent evaluation of the role of definity in producing sonoporation of chinese hamster ovary cells," *Journal of Ultrasound in Medicine*, vol. 30, no. 1, pp. 61–69, 2011.

[124] A. Rahim, S. Taylor, N. Bush, G. Ter Haar, J. Bamber, and C. Porter, "Physical parameters affecting ultrasound/microbubble-mediated gene delivery efficiency *in vitro*," *Ultrasound in Medicine and Biology*, vol. 32, no. 8, pp. 1269–1279, 2006.

[125] A. Sorace, J. Warram, H. Umphrey, and K. Hoyt, "Microbubble-mediated ultrasonic techniques for improved chemotherapeutic delivery in cancer," *Journal of Drug Targeting*, vol. 20, no. 1, pp. 43–54, 2012.

[126] R. Karshafian, S. Samac, P. Bevan, and P. Burns, "Microbubble mediated sonoporation of cells in suspension: Clonogenic viability and influence of molecular size on uptake," *Ultrasonics*, vol. 50, no. 7, pp. 691–697, 2010.

[127] C. Panje, D. Wang, M. Pysz, R. Paulmurugan, Y. Ren, F. Tranquart, L. Tian, and J. Willmann, "Ultrasound-mediated gene delivery with cationic versus neutral microbubbles: Effect of DNA and microbubble dose on *in vivo* transfection efficiency," *Theranostics*, vol. 2, no. 11, pp. 1078–1091, 2012.

[128] M. Borden, D. Kruse, C. Caskey, S. Zhao, P. Dayton, and K. Ferrara, "Influence of lipid shell physicochemical properties on ultrasound-induced microbubble destruction," *IEEE Transactions on Ultrasonics Ferroelectrics and Frequency Control*, vol. 52, no. 11, pp. 1992–2002, 2005.

[129] J. Feshitan, C. Chen, J. Kwan, and M. Borden, "Microbubble size isolation by differential centrifugation," *Journal of Colloid and Interface Science*, vol. 329, no. 2, pp. 316–324, 2009.

[130] Y. Wang, W. Bai, E. Shen, and B. Hu, "Sonoporation by low-frequency and low-power ultrasound enhances chemotherapeutic efficacy in prostate cancer cells *in vitro*," *Oncology Letters*, vol. 6, no. 2, pp. 495–498, 2013.

[131] J. Zhang, J. Saggar, Z. Zhou, and H. Bing, "Different effects of sonoporation on cell morphology and viability," *Bosnian Journal of Basic Medical Sciences*, vol. 12, no. 2, pp. 64–68, 2012.

[132] Z. Fan, D. Chen, and C. Deng, "Improving ultrasound gene transfection efficiency by controlling ultrasound excitation of microbubbles," *Journal of Controlled Release*, vol. 170, no. 3, pp. 401–413, 2013.

[133] S. Hernot and A. Klibanov, "Microbubbles in ultrasound-triggered drug and gene delivery," *Advanced Drug Delivery Reviews*, vol. 60, no. 10, pp. 1153–1166, 2008.

[134] A. Rahim, S. Taylor, N. Bush, G. ter Haar, J. Bamber, and C. Porter, "Spatial and acoustic pressure dependence of microbubble-mediated gene delivery targeted using focused ultrasound," *Journal of Gene Medicine*, vol. 8, no. 11, pp. 1347–1357, 2006.

[135] J. Chen, A. Dhanaliwala, A. Dixon, A. Klibanov, and J. Hossack, "Synthesis and characterization of transiently stable albumin-coated microbubbles via a flow-focusing microfluidic device," *Ultrasound in Medicine and Biology*, vol. 40, no. 2, pp. 400–409, 2014.

[136] A. Raisinghani and A. DeMaria, "Physical principles of microbubble ultrasound contrast agents," *American Journal of Cardiology*, vol. 90, no. 10A, pp. 3J–7J, 2002.

[137] J. Alter, C. Sennoga, D. Lopes, R. Eckersley, and D. Wells, "Microbubble stability is a major determinant of the efficiency of ultrasound and microbubble mediated emphin vivo gene transfer," *Ultrasound in Medicine and Biology*, vol. 35, no. 6, pp. 976–84, 2009.

[138] K. Hensel, M. Mienkina, and G. Schmitz, "Analysis of ultrasound fields in cell culture wells for *in vitro* ultrasound therapy experiments," *Ultrasound in Medicine and Biology*, vol. 37, no. 12, pp. 2105–2115, 2011.

[139] S. Marvel, S. Okrasinski, S. Bernacki, E. Loboa, and P. Dayton, "The development and validation of a lipus system with preliminary observations of ultrasonic effects on human adult stem cells," *IEEE Transactions on Ultrasonics Ferroelectrics and Frequency Control*, vol. 57, no. 9, pp. 1977–1984, 2010.

[140] X. Dong, C. Mattingly, M. Tseng, M. Cho, V. Adams, and R. Mumper, "Development of new lipid-based paclitaxel nanoparticles using sequential simplex optimization," *European Journal of Pharmaceutics and Biopharmaceutics*, vol. 72, no. 1, pp. 9–17, 2009.

[141] X. Dong, C. Mattingly, M. Tseng, M. Cho, Y. Liu, V. Adams, and R. Mumper, "Doxorubicin and paclitaxel-loaded lipid-based nanoparticles overcome multidrug resistance by inhibiting p-glycoprotein and depleting ATP," *Cancer Research*, vol. 69, no. 9, pp. 3918–3926, 2009.

[142] D. Peer, J. Karp, S. Hong, O. FaroKhzad, R. Margalit, and R. Langer, "Nanocarriers as an emerging platform for cancer therapy," *Nature Nanotechnology*, vol. 2, no. 12, pp. 751–760, 2007.

[143] X. Dong and R. Mumper, "Nanomedicinal strategies to treat multidrug-resistant tumors: Current progress," *Nanomedicine*, vol. 5, no. 4, pp. 597–615, 2010.

[144] P. Ma, "C22-px treatment of 4t1 tumor bearing balb/c mice." unpublished.

[145] C. Burke, E. Alexander, K. Timbie, A. Kilbanov, and R. Price, "Ultrasound-activated agents comprised of 5FU-bearing nanoparticles bonded to microbubbles inhibit solid tumor growth and improve survival," *Molecular Therapy*, vol. 22, no. 2, pp. 321–328, 2014.

[146] R. Gessner, J. Streeter, R. Kothadia, S. Feingold, and P. Dayton, "An *in vivo* validation of the application of acoustic radiation force to enhance the diagnostic utility of molecular imaging using 3-D ultrasound," *Ultrasound in Medicine and Biology*, vol. 38, no. 4, pp. 651–660, 2012.

[147] F. Yan, L. Li, Z. Deng, Q. Jin, J. Chen, W. Yang, C. Yeh, J. Wu, R. Shandas, X. Liu, and H. Zheng, "Paclitaxel-liposome-microbubble complexes as ultrasound-triggered therapeutic drug delivery carriers," *Journal of Controlled Release*, vol. 166, no. 3, pp. 246–255, 2013.

[148] H. Kobayashi, R. Watanabe, and P. Choyke, "Improving conventional enhanced permeability and retention (epr) effects; what is the appropriate target?," *Theranostics*, vol. 4, no. 1, pp. 81–89, 2014.

[149] B. Theek, F. Gremse, S. Kunjachan, S. Fokong, R. Pola, M. Pechar, R. Deckers, G. Storm, J. Ehling, Kiessling, and T. Lammers, "Characterizing EPR-mediated passive drug targeting using contrast-enhanced functional ultrasound imaging," *Journal of Controlled Release*, vol. 182, pp. 83–89, 2014.

[150] G. Song, "PK analysis of pegylated liposomal doxorubicin in C3Tag mice." unpublished.

[151] P. McConville, W. Elliott, A. Kreger, R. Lister, J. Moody, E. Trachet, F. Urban, and W. Leopold, "Preclinical models of tumor growth and response," in *In Vivo Imaging of Cancer Therapy* (A. Shields and P. Price, eds.), Cancer Drug Discovery and Development, pp. 13–32, Humana Press, 2007.

[152] N. Sharpless and R. Depinho, "The mighty mouse: Genetically engineered mouse models in cancer drug development," *Nature Reviews Drug Discovery*, vol. 5, no. 9, pp. 741–754, 2006.

[153] C. Caskey, X. Hu, and K. Ferrara, "Leveraging the power of ultrasound for therapeutic design and optimization," *Journal of Controlled Release*, vol. 156, no. 3, pp. 297–306, 2011.

[154] F. Kiessling, J. Bzyl, S. Fokong, M. Siepmann, G. Schmitz, and M. Palmowski, "Targeted ultrasound imaging of cancer: An emerging technology on its way to clinics," *Current Pharmaceutical Design*, vol. 156, no. 3, pp. 2184–2199, 2012.

[155] W. Zamboni, "Liposomal, nanoparticle, and conjugated formulations of anticancer agents," *Clinical Cancer Research*, vol. 11, no. 23, pp. 8230–8234, 2005.

[156] W. Zamboni, S. Strychor, E. Joseph, D. Walsh, B. Zamboni, R. Parise, M. Tonda, N. Yu, C. Engbers, and J. Eiseman, "Plasma, tumor, and tissue disposition of stealth liposomal ckd-602 (s-ckd602) and nonliposomal ckd-602 in mice bearing a375 human melanoma xenografts," *Clinical Cancer Research*, vol. 13, no. 23, pp. 7217–7223, 2007.

[157] S. Feingold, R. Gessner, I. Guracar, and P. Dayton, "Quantitative volumetric perfusion mapping of the microvasculature using contrast ultrasound," *Investigative Radiology*, vol. 45, no. 10, pp. 669–674, 2010.

[158] M. Borden, G. Martinez, J. Ricker, N. Tsvetkova, M. Longo, R. Gillies, P. Dayton, and K. Ferrara, "Lateral phase separation in lipid-coated microbubbles," *Langmuir*, vol. 22, no. 9, pp. 4291–4297, 2006.

[159] M. Kaya, S. Feingold, K. Hettiarachchi, A. Lee, and P. Dayton, "Acoustic responses of monodisperse lipid-encapsulated microbubble contrast agents produced by flow focusing," *Bubble Science Engineering and Technology*, vol. 2, no. 2, p. 8, 2010.

[160] K. Hettiarachchi, A. Lee, S. Zhang, S. Feingold, and P. A. Dayton, "Controllable microfluidic synthesis of multiphase drug-carrying lipospheres for site-targeted therapy," *Biotechnology Progress*, vol. 25, no. 4, pp. 938–945, 2009.

[161] S. Kotopoulis, G. Dimcevski, O. Gilja, D. Helge Hoem, and M. Postema, "Treatment of human pancreatic cancer using combined ultrasound, microbubbles, and gemcitabine: A clinical case study," *Medical Physics*, vol. 40, no. 7, p. 072902, 2013.

[162] M. Main, A. Ryan, T. Davis, M. Albano, L. Kusnetzky, and H. M, "Acute mortality in hospitalized patients undergoing echocardiography with and without an ultrasound contrast agent (multicenter registry results in 4,300,966 consecutive patients)," *American Journal of Cardiology*, vol. 102, no. 12, pp. 1742–1746, 2008.

[163] M. Azmin, C. Harfield, Z. Ahmad, M. Edirisinghe, and E. Stride, "How do microbubbles and ultrasound interact? Basic physical, dynamic and engineering principles," *Current Pharmaceutical Design*, vol. 18, no. 15, 2012.

[164] R. Phillips, M. Stratmeyer, and G. Harris, "Safety and u.s. regulatory considerations in the nonclinical use of medical ultrasound devices," *Ultrasound in Medicine and Biology*, vol. 36, no. 8, 2010.

[165] J. Kilroy, A. Klibanov, B. Wamhoff, and J. Hossack, "Intravascular ultrasound catheter to enhance microbubble-based drug delivery via acoustic radiation force," *IEEE Transactions on Ultrasonics, Ferroelectrics, and Frequency Control*, vol. 59, no. 10, pp. 2156–2166, 2012.

[166] S. Grainger, J. Serna, S. Sunny, Y. Zhou, C. Deng, and M. El-Sayed, "Pulsed ultrasound enhances nanoparticle penetration into breast cancer spheroids," *Molecular Pharmaceutics*, vol. 7, no. 6, pp. 2006–2019, 2010.

[167] J. Eisenbrey2010, M. Soulen, and M. Wheatley, "Delivery of encapsulated doxorubicin by ultrasound-mediated size reduction of drug-loaded polymer contrast agents," *IEEE Transactions on Biomedical Engineering*, no. 1, 2010.

[168] J. Escoffre, B. Geer, A. Novell, I. Lentaker, A. M, and A. Bouakaz, "Doxorubicin liposome-loaded microbubbles for contrast imaging and ultrasound- triggered drug delivery," *IEEE Transactions on Ultrasonics, Ferroelectronics and Frequency Control*, vol. 60, no. 1, pp. 78–86, 2013.

[169] Z. Deng, F. Yan, Q. Jin, F. Li, J. Wu, X. Liu, and H. Zheng, "Reversal of multidrug resistance phenotype in human breast cancer cells using doxorubicin-liposomemicrobubble complexes assisted by ultrasound," *Journal of Controlled Release*, vol. 174, pp. 109–116, 2014.

[170] B. Geers, O. De Wever, J. Demeester, M. Bracke, S. De Smedt, and I. Lentacker, "Targeted liposome-loaded microbubbles for cell- specific ultrasound- triggered drug delivery," *Small*, no. 23, pp. 4027–4035, 2013.

[171] R. Seip, E. Leyvi, B. Raju, W. Shi, M. Bohmer, C. Chlon, and C. Sio, "Ultrasound and microbubble mediated doxil delivery in a murine breast cancer model: Therapeutic efficacy dependence on tumor growth rate," *IEEE International Ultrasonics Symposium*, pp. 1894–1897, 2011.

[172] S. Graham, R. Carlisle, J. Choi, M. Stevenson, A. Shah, R. Myers, K. Fisher, M.-B. Peregrino, L. Symour, and C. Coussios, "Inertial cavitation to non-invasively trigger and monitor intratumoral release of drug from intravenously delivered liposomes," *Journal of Controlled Release*, vol. 128, pp. 101–107, 2014.

[173] L. Yao, Q. Song, W. Bai, J. Zhang, D. Miao, M. Jiang, Y. Wang, Z. Shen, Q. Hu, X. Gu, M. Huang, G. Zheng, X. Gao, B. Hu, C. J, and H. Chen, "Facilitated brain delivery of poly (ethylene glycol)-poly (lactic acid) nanoparticles by microbubble-enhanced unfocused ultrasound," *Biomaterials*, no. 10, pp. 3384–3395, 2014.

[174] S. Cool, B. Geers, S. Roels, S. Stremersch, K. Vanderperren, J. Saunders, S. De Scmedt, D. Demeester, and N. Sanders, "Coupling of drug containing liposomes to microbubbles improves ultrasound triggered drug delivery in mice," *Journal of Controlled Release*, no. 3, pp. 885–893, 2013.

[175] D. Cogrove, "Ultrasound contrast agents: An overview," *European Journal of Radiology*, vol. 60, pp. 324–330, 2006.

[176] B. Goldberg, J. Raichlen, and F. Forsberg, "Ultrasound contrast agents: Basic principles and clinical applications," *Ultrasound in Medicine and Biology*, 2001.

[177] S. Ohlerth and R. OBrien, "Contrast ultrasound: General principles and veterinary clinical applications," *The Veterinary Journal*, vol. 174, pp. 501–512, 2007.

[178] M. Schneider, "Molecular imaging and ultrasound-assisted drug delivery," *Journal of Endourology*, vol. 22, pp. 795–802, 2008.

[179] J. Ophir and K. Parker, "Contrast agents in diagnostic ultrasound," *Ultrasound in Medicine and Biology*, vol. 15, pp. 319–333, 1989.

[180] C. Carr and J. Lindner, "Myocardial perfusion imaging with contrast echocardiography," *Echocardiography*, vol. 22, pp. 795–802, 2008.

[181] M. Schneider, "Design of an ultrasound contrast agent for myocardial perfusion," *Echocardiography*, vol. 17, pp. S11–16, 2000.

[182] K. Sugimoto, F. Moriyasu, N. Kamiyama, R. Metoki, and I. H, "Parametric imaging of contrast ultrasound for the evaluation of neovascularization in liver tumors," *Hepatology Research*, vol. 37, pp. 464–472, 2007.

[183] S. Stieger, P. Dayton, M. Borden, C. Caskey, S. Griffey, E. Wisner, and K. Ferrara, "Imaging of angiogenesis using cadence contrast pulse sequencing and targeted contrast agents," *Contrast Media and Molecular Imaging*, vol. 3, pp. 9–18, 2008.

[184] F. Villanueva, "Myocardial ischemic memory imaging with molecular echocardiography," *Circulation*, vol. 115, pp. 345–352, 2007.

[185] J. Willmann, A. Lutz, R. Paulmurugan, M. Patel, P. Chu, J. Rosenberg, and S. Gambhir, "Dual-targeted contrast agent for us assessment of tumor angiogenesis *in vivo*," *Radiology*, vol. 248, pp. 936–944, 2008.

[186] K. Soetanto and M. Cham, "Study on the lifetime and attenuation properties of microbubbles coated with carboxylic acid salts," *Ultrasonics*, vol. 38, pp. 969–977, 2000.

[187] A. Kabalnov, J. Bradley, S. Flaim, D. Klein, T. Pelura, B. Peters, S. Otto, J. Reynolds, E. Schutt, and J. Weers, "Dissolution of multicomponent microbubbles in the bloodstream: 2. Experiment," *Ultrasound in Medicine and Biology*, vol. 24, no. 5, pp. 751–760, 1998.

[188] J. Chomas, P. Dayton, J. Allen, K. Morgan, and K. Ferrara, "Mechanisms of contrast agent destruction," *IEEE Transactions on Ultrasonics Ferroelectrics and Frequency Control*, vol. 48, no. 1, pp. 232–248, 2001.

[189] J. Wible, J. Wojdyla, D. Scherrer, M. Adams, and G. Brandenburger, "Improving the sonographic contrast produced by albunex during the inhalation of gases other than air," *Academic Radiology*, vol. 3, pp. S317–S319, 1996.

[190] J. Wible Jr, J. Wojdyla, J. Bugaj, and G. Brandenburger, "Effects of inhaled gases on the ultrasound contrast produced by microspheres containing air or perfluoropropane in anesthetized dogs," *Investigative Radiology*, vol. 33, no. 12, pp. 871–9, 1998.

[191] M. Borden, M. Sarantos, S. Stieger, S. Simon, K. Ferrara, and P. Dayton, "Ultrasound radiation force modulates ligand availability on targeted contrast agents," *Molecular Imaging*, vol. 5, no. 3, pp. 139–147, 2006.

[192] J. Riess, "Understanding the fundamentals of perfluorocarbons and perfluorocarbon emulsions relevant to *in vivo* oxygen delivery," *Artificial Cells Blood Substitutes and Biotechnology*, vol. 33, no. 1, pp. 47–63, 2005.

[193] M. Borden and L. ML, "Dissolution behavior of lipid monolayercoated, air-filled microbubbles: Effect of lipid hydrophobic chain length," *Langmuir*, vol. 18, no. 24, pp. 9225–9233, 2002.

[194] P. Duncan and D. Needham, "Test of the epstein-plesset model for gas microparticle dissolution in aqueous media: Effect of surface tension and gas undersaturation in solution," *Langmuir*, vol. 20, no. 7, pp. 2567–2578, 2004.

[195] E. Talu, K. Hettiarachchi, R. Powell, A. Lee, P. Dayton, and M. Longo, "Maintaining monodispersity in a microbubble population formed by flow-focusing," *Langmuir*, vol. 24, no. 5, pp. 1745–1749, 2008.

[196] J. Kwan and M. Borden, "Microbubble dissolution in a multigas environment," *Langmuir*, vol. 26, no. 9, pp. 6542–6548, 2010.

[197] A. Killam, P. Mehlhaff, P. Zavorskas, Y. Greener, B. McFerran, J. Miller, C. Burrascano, E. Jablonski, L. Anderson, and H. Dittrich, "Tissue distribution of I-125-labeled albumin in rats, and whole blood and exhaled elimination kinetics of octafluoropropane in anesthetized canines, following intravenous administration of optison (r) (FS069)," *International Journal of Toxicology*, vol. 18, no. 1, pp. 49–63, 1999.

[198] J. Nunn, *Applied Respiratory Physiology*. Butterworths: London, 1987.

[199] J. West, *Respiratory Physiology*. Williams and Wilkins: Philadelphia, PA, 1990.

[200] S. Gambhir, S. Inao, M. Tadokoro, M. Nishino, K. Ito, T. Ishigaki, H. Kuchiwaki, and J. Yoshida, "Comparison of vasodilatory effect of carbon dioxide inhalation and intravenous acetazolamide on brain vasculature using positron emission tomography," *Neurological Research*, vol. 19, no. 2, pp. 139–144, 1997.

[201] M. Burkard and H. Vanliew, "Oxygen-transport to tissue by persistent bubbles - theory and simulations," *Journal of Applied Physiology*, vol. 77, no. 6, pp. 2874–2878, 1994.

[202] D. Chatterjee, P. Jain, and K. Sarkar, "Ultrasound-mediated destruction of contrast microbubbles used for medical imaging and drug delivery," *Physics of Fluids*, vol. 17, no. 10, 2005.

[203] K. Sarkar, A. Katiyar, and P. Jain, "Growth and dissolution of an encapsulated contrast microbubble: Effects of encapsulation permeability," *Ultrasound in Medicine and Biology*, vol. 35, no. 8, pp. 1385–96, 2009.